JOURNAL OF PETROLOGY | VOLUME 47 | NUMBER 6 | PAGES 1177–1220 | 2006 | doi:10.1093/petrology/egl007

Post-collisional, Potassic and Ultrapotassic Magmatism of the Northern Tibetan Plateau: Constraints on Characteristics of the Mantle Source, Geodynamic Setting and Uplift Mechanisms

ZHENGFU GUO[1,2]*, MARJORIE WILSON[2], JIAQI LIU[1] AND QIAN MAO[1]

[1]INSTITUTE OF GEOLOGY AND GEOPHYSICS, CHINESE ACADEMY OF SCIENCES, P.O. BOX 9825, BEIJING 100029, PEOPLE'S REPUBLIC OF CHINA

[2]INSTITUTE OF GEOPHYSICS AND TECTONICS, SCHOOL OF EARTH AND ENVIRONMENT, UNIVERSITY OF LEEDS, LEEDS LS2 9JT, UK

RECEIVED JANUARY 10, 2005; ACCEPTED FEBRUARY 6, 2006
ADVANCE ACCESS PUBLICATION MARCH 7, 2006

Cenozoic, post-collisional, potassic and ultrapotassic igneous rocks in the North Qiangtang, Songpan–Ganzi and North Kunlun terranes of the northern Tibetan Plateau are distributed along a semi-continuous, east–west-trending, volcanic belt, which is over 1200 km in length. Spatially, there is a close association with major strike-slip faults, thrust faults and pull-apart basins. The ages of these magmatic rocks range from 45 Ma to the present (the youngest known eruption occurred in 1951); they are shoshonitic, compositionally similar to K-rich subduction-related magmas, and range in SiO_2 from 44 to 66 wt %. There is a relative enrichment of large ion lithophile elements (LILE) and light rare earth elements (LREE) in the most primitive magmatic rocks (MgO >6 wt %) in the North Qiangtang terrane compared with those in the Songpan–Ganzi and North Kunlun terranes; correspondingly, the primitive magmas have higher $^{87}Sr/^{86}Sr$ and $^{206}Pb/^{204}Pb$, and lower $^{143}Nd/^{144}Nd$ ratios in the North Qiangtang terrane than in the Songpan–Ganzi and North Kunlun terranes. The dominant factors that control the geochemical characteristics of the magmas are an enriched asthenospheric mantle source composition, the degree of partial melting of this source, and the combined processes of crustal assimilation and fractional crystallization (AFC). Enrichment of the asthenosphere is considered to have occurred by incorporation of subducted sediments into the mantle wedge above a subducted slab of Indian lithosphere during India–Asia convergence. Continental lithospheric mantle, metasomatically enriched during earlier episodes of subduction, may have also contributed a source component to the magmas. Trace element modelling indicates that the mantle source of the most primitive magmas in the North Qiangtang terrane contained higher amounts of subducted sediment (0·5–10%) compared with those in the Songpan–Ganzi and North Kunlun terranes (<2%). The degrees of partial melting required to generate the primitive potassic and ultrapotassic magmas from the enriched mantle sources range from <0·1% to ~15% in the three major basement terranes. Energy-constrained AFC model calculations show that the more evolved magmatic rocks (MgO <6 wt %) are the results of AFC processes in the middle crust in the North Qiangtang terrane and the upper crust in the Songpan–Ganzi and North Kunlun terranes. We propose that the ultimate driving force for the generation of the post-collisional potassium-rich magmatism in north Tibet is the continuous northward underthrusting of the Indian continental lithosphere following India–Asia collision. This underthrusting resulted in upwelling of hot asthenosphere beneath north Tibet, squeezed up between the advancing Indian lithosphere and the backstop of the rigid Asian continental lithosphere. Asthenospheric upwelling may have also contributed to uplift of the northern Tibetan Plateau.

KEY WORDS: *Tibetan Plateau; potassic and ultrapotassic magmatism; enriched asthenospheric mantle source; EC-AFC modelling; geodynamics*

*Corresponding author. Present address: Institute of Geology and Geophysics, Chinese Academy of Sciences, P.O. Box 9825, Beijing 100029, People's Republic of China. Telephone: 0086 10 62007334. Fax: 0086 10 62010846. E-mail: zhengfu@earth.leeds.ac.uk; zfguo@mail.iggcas.ac.cn

INTRODUCTION

Cenozoic, post-collisional, potassium-rich igneous rocks form a nearly east–west-trending, semi-continuous, magmatic province in the northern Tibetan Plateau, mainly distributed within the North Kunlun, Songpan–Ganzi and North Qiangtang terranes (Fig. 1). The magmatism is considered to be an indicator of evolving mantle dynamics associated with subduction of Indian continental lithosphere and uplift of the northern Tibetan Plateau following India–Asia collision (Arnaud *et al.*, 1992; Turner *et al.*, 1993, 1996*a*; Deng, 1998; Pan *et al.*, 1998; Liu, 1999; Ding *et al.*, 2003). Although there have been many studies of these magmatic rocks since 1946 (e.g. Norin, 1946; Pearce & Mei, 1988; Turner *et al.*, 1996*a*; Lai *et al.*, 2003; Deng *et al.*, 2004; Williams *et al.*, 2004), their petrogenesis and geodynamic setting remain controversial. Magma generation has been ascribed to convective removal of the lower part of the lithospheric mantle (e.g. Turner *et al.*, 1993, 1996*a*; Williams *et al.*, 2004) and to intracontinental subduction of the Tarim and Qaidam terranes (Fig. 1) beneath the northern Tibetan Plateau (e.g. Pearce & Mei, 1988; Deng, 1989, 1991, 1998; Arnaud *et al.*, 1992; Willet & Beaumont, 1994; Jin *et al.*, 1996; Meyer *et al.*, 1998; Tapponnier *et al.*, 2001; Ding *et al.*, 2003). Williams *et al.* (2004) have suggested that the magmatism in north and south Tibet may have a different petrogenesis; magma generation in north Tibet may be triggered by convective removal of the lower part of the lithospheric mantle, whereas that in south Tibet may be controlled by subducted slab breakoff, probably implying differences in uplift mechanism between the northern and southern parts of the Tibetan Plateau. Post-collisional igneous rocks spanning 45 Myr (Fig. 2) make the Tibetan Plateau magmatism truly unique. The lack of detailed studies of the temporal and spatial changes in the petrological and geochemical characteristics of the magmatic rocks, particularly given the relative rarity of primitive compositions (MgO >6 wt %), has precluded further constraints on the nature of their mantle source region, petrogenesis, tectonic setting, and the uplift mechanism of the northern Tibetan Plateau.

This study focuses on potassium-rich magmatism in 25 volcanic fields in north Tibet, extending across a region some 1200 km from west to east and 350 km from north to south (Fig. 1). Emphasis is placed on the magmatism within the North Qiangtang, Songpan–Ganzi and North Kunlun terranes, for which there are relatively few published geochemical data, mainly because of the inaccessibility of the area. The samples studied include a wide range of rock types and cover the complete age range of post-collisional magmatism from ~45 Ma to AD 1951 in the different basement terranes (Table 1 and Fig. 2). Six of the samples studied (JH23, JH6, XT8, KX91, KX84 and KX67; Table 2), with MgO >6 wt % (Table 3 and Electronic Appendix), contain mantle xenoliths, indicating short residence times of these magmas in the crust. Compared with previous studies (e.g. Arnaud *et al.*, 1992; Turner *et al.*, 1993, 1996*a*; Williams *et al.*, 2004), which were predominantly based on igneous rocks with MgO <6 wt %, we have much better coverage of the more primitive magma compositions over a much wider geographical area. We present new major and trace element analyses for 50 samples and Sr–Nd–Pb isotopic data for a subset of 30 samples. On the basis of these and previously published geochronological, geochemical and geophysical data, we develop a model to explain the petrogenesis and geodynamic setting of the post-collisional potassium-rich magmatism.

GEOLOGICAL SETTING

Tertiary–recent potassium-rich magmatism in the northern Tibetan Plateau

The potassic and ultrapotassic magmatic rocks that form the basis of this study are located in the North Kunlun, Songpan–Ganzi and North Qiangtang terranes (Fig. 1). The ages of these rocks (Fig. 2) range from *c.* 45 Ma to the present (i.e. AD 1951) on the basis of five thermoluminescence (TL) ages, two ^{14}C ages, one single-zircon U–Pb age, 78 K–Ar and 36 $^{40}Ar/^{39}Ar$ ages, as well as historical records of an active volcanic eruption in Ashikule in AD 1951 [Harris *et al.*, 1988*b*; Pearce & Mei, 1988; Deng, 1989, 1991, 1993, 1998; Li *et al.*, 1989; Liu, 1989, 1999; Liu & Xie, 1989; Liu & Maimaiti, 1990; Arnaud *et al.*, 1992; Sun, 1992; Turner *et al.*, 1993, 1996*a*; Xinjiang Bureau of Geology and Mineral Resources (XBGMR), 1993; Zhang & Zheng, 1994; Deng *et al.*, 1996; Chi *et al.*, 1999; Ding *et al.*, 1999, 2003; Tan *et al.*, 2000; Wu *et al.*, 2001; Luo *et al.*, 2003; Williams *et al.*, 2004; Wang *et al.*, 2005]. The magmatism post-dates the onset of India–Asia continental collision in southern Tibet at ~65–70 Ma (Yin & Harrison, 2000), showing that it was generated in a post-collisional tectonic setting. Temporally, magmatism has been semi-continuous since 45 Ma; spatially, it becomes progressively younger from south to north (Fig. 2a). Magmatic activity is characterized by scattered, small-volume lava flows, pyroclastic deposits, cinder cones and volcanic necks. The volcanic fields studied have outcrops that vary from >1000 km^2 (e.g. the Duogecuoren and Qiangbaqian fields) to <2 km^2 (e.g. the Dahongliutan field); most are relatively small (Table 1). Some of the volcanic rocks studied here (e.g. the Xiongyingtai, Jingyuhu and Kangxiwa fields; Tables 2 and 3) contain mantle xenoliths (Luo *et al.*, 2000; Wu *et al.*, 2001), implying that the host magmas are relatively primitive.

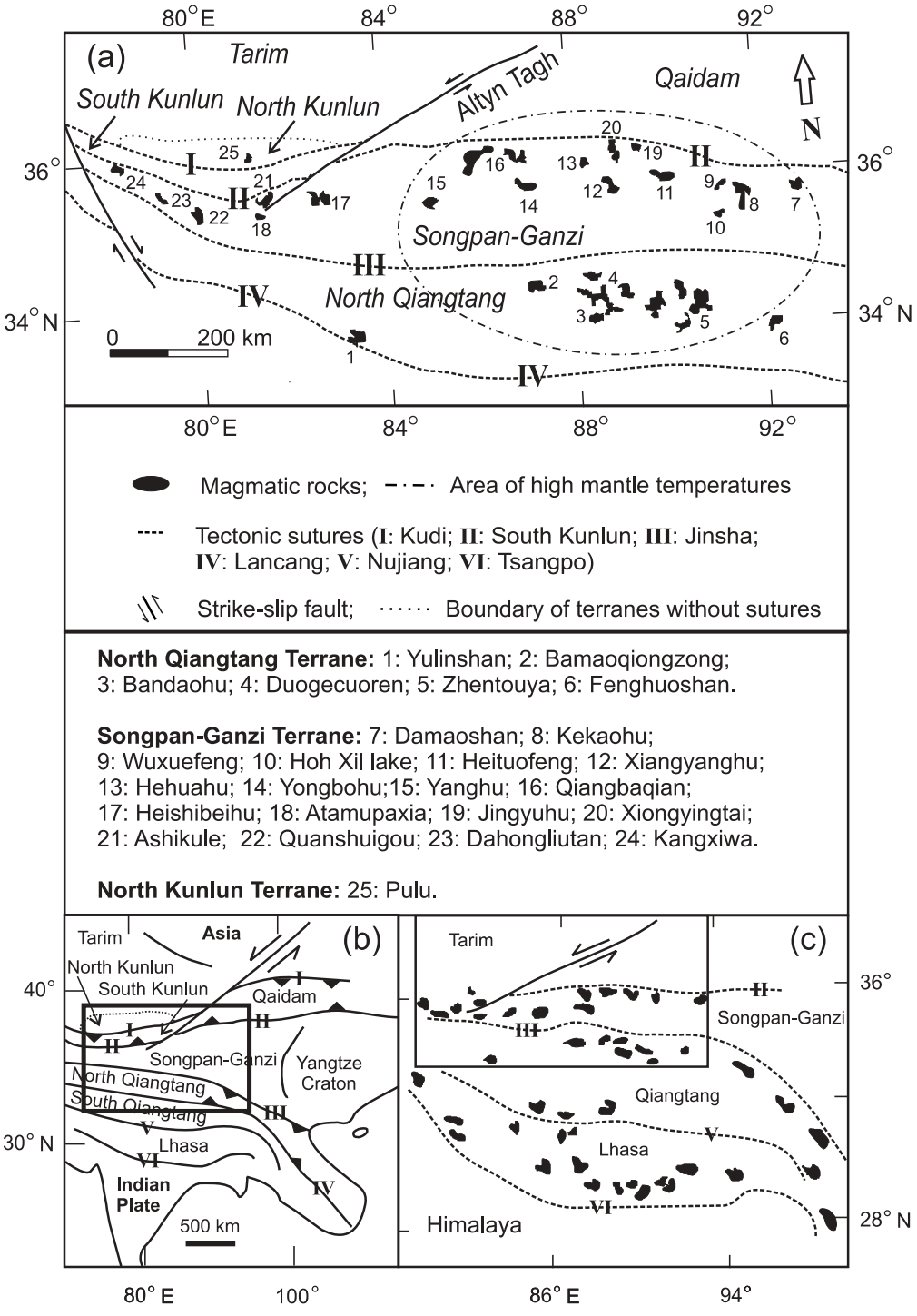

Fig. 1. (a) Simplified map showing the distribution of Cenozoic post-collisional potassic and ultrapotassic magmatism in the northern part of the Tibetan Plateau (modified from Deng, 1998; Yang, 1998; Liu, 1999; Wang *et al.*, 2000; Yin & Harrison, 2000; Xiao *et al.*, 2002; Ding *et al.*, 2003; Mo *et al.*, 2003). The dot–dashed line represents an area of inferred high upper mantle temperatures based on inefficient regional S-wave (S_n) propagation (Ni & Barazangi, 1983; McNamara *et al.*, 1995) and low regional P-wave (P_n) velocity (McNamara *et al.*, 1995; Owens & Zandt, 1997; Kosarev *et al.*, 1999; Xu *et al.*, 1999). (b) Regional map showing the position of the study area in relation to the main tectonic sutures in the Tibetan Plateau (modified from Liu, 1999; Deng *et al.*, 2004). The bold rectangle shows the position of the study area. The continuous lines with Roman numbers (i.e. I, II, III, etc.) represent the main tectonic sutures. The filled triangles on the continuous lines point in the direction of subduction of oceanic lithosphere. The Roman numbers correspond to those in (a). (c) Map showing the distribution of post-collisional magmatic rocks in northern and southern Tibet (modified from Chung *et al.*, 1998; Williams *et al.*, 2004). The rectangle shows the location of the study area. The Roman numbers correspond to those in (a) and (b).

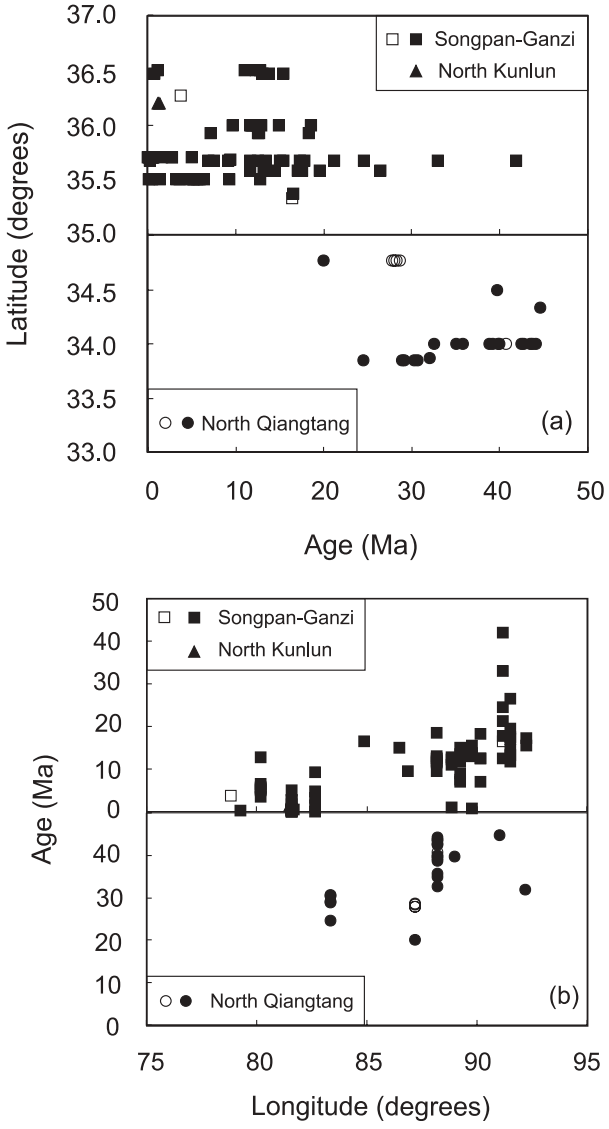

Fig. 2. Variation of the ages of the potassium-rich magmatism in the terranes of north Tibet according to latitude and longitude based on 123 dated samples [i.e. K–Ar (78 ages), $^{40}Ar/^{39}Ar$ (36 ages), thermoluminescence (five ages), ^{14}C (two ages), historical record (one age), single-zircon U–Pb dating by SHRIMP II (one age)]. Sources of the data are given in Table 1. The open symbols denote samples that have MgO >6 wt %; the filled symbols denote samples that have MgO <6 wt %. (a) Latitude (degrees) vs age (Ma). (b) Age (Ma) vs longitude (degrees).

Phanerozoic history of the basement terranes in north Tibet

Because the Tertiary–recent potassium-rich magmatism of north Tibet spans a number of different basement terranes that may contribute to the petrogenesis of the magmas, we first need to review the geological history of these terranes; particular emphasis is placed on identifying tectono-magmatic events that might have caused enrichment of the mantle part of the lithosphere and on the characteristics of the crust.

The northern Tibetan Plateau is a collage of several allochthonous continental terranes whose boundaries are marked by tectonic suture zones (Fig. 1). From north to south, these are the Kudi suture (I), the South Kunlun suture (II), the Jinsha suture (III) and the Lancang suture (IV). Correspondingly, from north to south, the four main continental terranes are the North Kunlun terrane, South Kunlun terrane, Songpan–Ganzi terrane and North Qiangtang terrane (Fig. 1 and Table 4).

Within the northern Tibetan Plateau, Precambrian basement mainly crops out in the North Kunlun and South Kunlun terranes (Dewey *et al.*, 1988; Pan & Bian, 2000; Xiao *et al.*, 2002); this basement is composed of gneisses, schists, migmatites, stromatolite-bearing limestones, marbles, pelites, greywackes and cherts. A granite body, which has a zircon U–Pb age of 2261 Ma (Xu *et al.*, 2000), intrudes the basement of the North Kunlun terrane, providing a minimum Proterozoic age for the basement.

The Qiangtang terrane contains the most extensive exposures of metamorphic rocks in the interior of Tibet, forming an east–west-trending belt 500 km long by 100 km wide (Pan *et al.*, 1998; Kapp *et al.*, 2003). These form a tectonic mélange, interpreted by Kapp *et al.* (2000) as a metamorphic core complex, comprising a strongly deformed matrix of metasedimentary and mafic igneous schists enclosing less strongly deformed blocks of metabasite, Carboniferous–Triassic metasedimentary rocks and Early Palaeozoic gneisses. Both the blocks and matrix exhibit greenschist, epidote-blueschist and, locally, epidote-amphibolite metamorphic mineral assemblages consistent with exhumation from >35 km depth. Kapp *et al.* (2003) have proposed that this mélange was produced by underthrusting of oceanic crust and its sedimentary cover ~200 km beneath the Qiangtang terrane during southward, Early Mesozoic, low-angle subduction along the Jinsha suture. Low-angle subduction is consistent with the absence of a well-developed Triassic magmatic arc in central Tibet. This model has important geodynamic implications in that it predicts that a significant portion of the central Tibetan mantle lithosphere must have been removed during the Early Mesozoic, and thus would not be available to act as a source component for the Cenozoic magmas. Additionally, the model implies that the lower crust of central Tibet is dominantly composed of the same tectonic mélange. Hacker *et al.* (2000) have reported the presence of metasedimentary and mafic metaigneous, granulite-facies, crustal xenoliths in 3 Ma shoshonitic lavas from central Tibet, which would be consistent with the Kapp *et al.* (2003) model. These xenoliths record a thermal gradient reaching 800–1000°C at a depth of 30–50 km and a late-stage heating event consistent with injection of magma into the lower

Table 1: Volumes and ages of the post-collisional K-rich magmatism in north Tibet

Field no.	Locality	Area (km^2)	Thickness (m)	Volume (km^3)	Age (Ma)	Average age (Ma)	Data sources
1	Yulinshan	150	150	22·5	24·50 (a), 28·88, 29·2 (b), 30·33, 30·66 (a)	28·7	[1,2]
2	Bamaoqiongzong	300	50	15	{20·0, 27·8, 28·0, 28·3, 28·6} (a)	26·5	[3]
3	Bandaohu	200	80	16	32·6, 35·0, 35·8, 38·8, 39·2, 39·8, 39·9, 40·7, 42·5, 42·7, 43·5, 43·7, 44·1 (a)	39·9	[4]
4	Duogecuoren	1000	50	50	39·7 (b)	39·7	[5]
5	Zhentouya	800	60	48	44·7 (a)	44·7	[6]
6	Fenghuoshan	10	70	0·7	32 (a)	32	[7]
7	Damaoshan	150	80	12	15·39, <17·3> (a)	16·3	[8]
8	Kekaohu	300	70	21	<11·7>, 13·2, 14·47, 17·04, 17·6, 19·6, 26·5 (a)	17·2	[6,8]
9	Wuxuefeng	200	80	16	12·53, 17·75, 21·24, 24·55, 32·9, 41·9 (a)	25·1	[6,9]
10	Hoh Xil lake	8	20	0·16	16·47 (b)	16·47	[10]
11	Heituofeng	120	40	4·8	7·09, 12·5, <12·60>, 18·3 (a)	12·6	[6,8]
12	Xiangyanghu	100	40	4	6·95, <7·49> (a), 8·3–9·9, 11·7, 13·4, 15·0 (b)	10·6	[8,11]
13	Hehuahu	150	70	10·5	9·6, 11·6, 11·8, 11·9, 12·4, 12·5, 12·9, 18·5 (b)	12·7	[11]
14	Yongbohu	50	50	2·5	9·4 (a)	9·4	[12]
15	Yanghu	20	80	1·6	16·5 (b)	16·5	[13]
16	Qiangbaqian	1500	30	45	{14·9} (a)	14·9	[3]
17	Heishibeihu	355	80	28·4	0·067 (c), 1·43, 3·27, 4·64, 9·23 (a)	3·7	[3,13,14]
18	Atamupaxia	60	60	3·6	0·56 (c)	0·56	[15]
19	Jingyuhu	135	150	20·3	0·69, 13·77, 15·47 (a), 13·0 (b)	10·7	[11,15,16]
20	Xiongyingtai	115	150	17·3	1·08 (c), 11·05, 12·22, 12·83 (a)	9·3	[15,16]
21	Ashikule	200	100	20	1951 AD (e), 0·0067–0·0087 (d), 0·074 (c), 0·12, 0·20, 0·28, 0·31, 0·44, 0·50, 0·52, 0·58, 0·60, 0·67, 1·65, 2·8 (a), 0·30, 0·50, 2·7, 5·0 (b)	0·96	[15,17,18,19]
22	Quanshuigou	220	100	22	3·6, 5·1, 5·3, 5·6, 5·84, 6·4 (a), 12·8 (b)	6·4	[14,19,20]
23	Dahongliutan	1	30	0·03	0·28 (c)	0·28	[13]
24	Kangxiwa	2	14	0·03	3·8 (f)	3·8	[21]
25	Pulu	5	22	0·11	1·19, 1·23, 1·24, 1·43 (a)	1·27	[17,22,23]

The number of each volcanic field corresponds to that in Fig. 1a. The distribution areas (km^2) and thickness (m) of the volcanic fields are based on previous data (Li *et al.*, 1989; Liu & Maimaiti, 1990; Deng, 1998; Liu, 1999) and this study. Sources of the age data for the magmatic rocks are as follows: [1] Ding *et al.* (1999); [2] Ding *et al.* (2003); [3] Deng (1989); [4] Tan *et al.* (2000); [5] Chi *et al.* (1999); [6] Zhang & Zheng (1994); [7] Pearce & Mei (1988); [8] Deng *et al.* (1996); [9] Sun (1992); [10] Wang *et al.* (2005); [11] Turner *et al.* (1996*a*); [12] Li *et al.* (1989); [13] Deng (1998); [14] XBGMR (1993); [15] Deng (1991); [16] Wu *et al.* (2001); [17] Liu & Maimaiti (1990); [18] Turner *et al.* (1993); [19] Williams *et al.* (2004); [20] Arnaud *et al.* (1992); [21] Luo *et al.* (2003); [22] Liu & Xie (1989); [23] Liu (1989). Analytical methods used to determine the ages of the igneous rocks, which are shown by letters in parentheses, are as follows: (a) K–Ar (78 ages); (b) $^{40}Ar/^{39}Ar$ (36 ages); (c) thermoluminescence (five ages); (d) ^{14}C (two ages); (e) historical record (one age); (f) single-zircon U–Pb dating by SHRIMP II (one age). The following ages were analysed in international geochronological laboratories by collaboration although they were first published in Chinese journals: { }, ages determined by A. R. Basu of the University of Rochester, USA; < >, ages determined at the Central Institute of Mitsubishi, Japan. Average age (Ma) is average value of all ages of the volcanic fields based on the analytical methods shown above.

crust at 1300°C. Controversy remains as to whether or not the Qiangtang terrane has any Precambrian basement rocks. There are Precambrian basement exposures in Changdu to the east and the Karakorum to the west, which are thought to be extensions of the Qiangtang terrane (Desio, 1979; Tahirkheli, 1982; Pan *et al.*, 1998).

The Phanerozoic cover sequences of the northern Tibetan Plateau mainly comprise clastic deposits, carbonates and interbedded volcanic rocks [BGMRXAR (Bureau of Geology and Mineral Resources of Xizang (Tibet) Autonomous Region), 1993; Pan *et al.*, 1998; Zhao *et al.*, 2001]. There is no evidence for the existence of Archaean crust in this region (Dewey *et al.*, 1988; Pan *et al.*, 1998; Pan & Bian, 2000).

Previous geological studies (e.g. Pan, 1996; Pan *et al.*, 1998; Pan & Bian, 2000; Xiao *et al.*, 2002) indicate that

Table 2: Phenocryst and groundmass mineral assemblages of the magmatic rocks of north Tibet

Field no.	Sample no.	Terrane	Locality	Mg-no.	Rock type	Phenocrysts	Groundmass
1	G26	North Qiangtang	Yulinshan	0·57	S3	Cpx (2) + Nos (1) + Ha (1) + Ne (2)	Cpx + Nos + Ha + Ne + Sani + Ap + Fe–Ti
1	G68	North Qiangtang	Yulinshan	0·22	S3	Nos (1) + Ha (1) + Lc (2) + Sani (1)	Nos + Ha + Sani + Ap + Fe–Ti + G
2	G98-3	North Qiangtang	Bamaoqiongzong	0·62	U1	Ol (1) + Cpx (2) + Lc (1)	Cpx + Ha + Ne + Sani + Ap
2	G98-1	North Qiangtang	Bamaoqiongzong	0·72	U2	Ol (3) + Cpx (1) + Nos (1) + Lc (1)	Cpx + Ha + Tit + Sani + Fe–Ti
2	G98-11	North Qiangtang	Bamaoqiongzong	0·69	U3	Ol (2) + Cpx (1) + Ne (1) + Fe–Ti (1)	Ha + Nos + Tit + Sani + G
2	G98-6	North Qiangtang	Bamaoqiongzong	0·65	U1	Cpx (2) + Nos (1) + Lc (1)	Cpx + Ha + Ne + Sani + Ap + Fe–Ti
2	G98-14	North Qiangtang	Bamaoqiongzong	0·65	U2	Cpx (1) + Ha (1) + Lc (1) + Sani (1)	Cpx + Nos + Sani + Ap + G
2	G98-9	North Qiangtang	Bamaoqiongzong	0·65	U1	Ol (1) + Cpx (1) + Phl (1)	Cpx + Nos + Ha + Fe–Ti
2	G98-0	North Qiangtang	Bamaoqiongzong	0·59	S2	Cpx (2) + Lc (1)	Ha + Tit + Sani + G
3	JC973	North Qiangtang	Bandaohu	0·60	S1	Cpx (1) + Sani (1)	Cpx + Sani + Pl + Fe–Ti
3	JC9719	North Qiangtang	Bandaohu	0·71	U1	Ol (2) + Cpx (1)	Cpx + Pl + Fe–Ti
3	JC975	North Qiangtang	Bandaohu	0·68	U1	Cpx (2) + Opx (1)	Cpx + Sani + Pl
4	JC9716	North Qiangtang	Duogecuoren	0·57	U2	Cpx (1) + Sani (1) + Pl (1)	Sani + Pl + Bi
4	JC9710	North Qiangtang	Duogecuoren	0·69	S2	Cpx (2) + Phl (1)	Cpx + Pl + Bi
4	JC978	North Qiangtang	Duogecuoren	0·62	S1	Ol (1) + Cpx (1)	Cpx + Pl + Sani
4	DG11	North Qiangtang	Duogecuoren	0·58	S2	Cpx (1) + Pl (1)	Bi + Pl + Sani
4	DG08	North Qiangtang	Duogecuoren	0·62	S2	Ol (1) + Cpx (1)	Bi + Sani + Ap
5	ZF91	North Qiangtang	Zhentouya	0·49	S3	Cpx (1) + Pl (1) + Sani (2)	Bi + Cpx + Sani + Ap + Fe–Ti
5	ZF96	North Qiangtang	Zhentouya	0·56	S3	Cpx (2) + Pl (1) + Sani (1)	Cpx + Sani + Bi + G
6	QN01	North Qiangtang	Fenghuoshan	0·51	T	Cpx (1) + Bi (3) + Sani (2)	Bi + Cpx + Sani + Fe–Ti
7	DM-9	Songpan–Ganzi	Damaoshan	0·31	S3	Sani (2) + Bi (2) + Qz (3)	Sani + Bi + Qz + Ap + Fe–Ti
8	YS-19	Songpan–Ganzi	Kekaohu	0·44	S3	Sani (3) + Qz (2)	Sani + Ap + Bi + Qz + G
9	YS-07	Songpan–Ganzi	Wuxuefeng	0·36	T	Pl (1) + Sani (2) + Bi (3) + Qz (2)	Sani + Bi + Qz + Fe–Ti
10	HX01	Songpan–Ganzi	Hoh Xil lake	0·65	U1	Ol (2) + Cpx (1) + Lc (1) + Ne (1)	Cpx + Lc + Sani + Ap + Fe–Ti
11	HT-18	Songpan–Ganzi	Heituofeng	0·47	S3	Cpx (1) + Pl (2) + Sani (2) + Bi (1)	Cpx + Sani + Bi
12	XY03	Songpan–Ganzi	Xiangyanghu	0·68	S2	Cpx (1) + Pl (3) + Phl (2)	Cpx + Pl
12	XY05	Songpan–Ganzi	Xiangyanghu	0·40	S3	Pl (1) + Sani (2) + Qz (2)	Pl + Bi + Sani + Qz
13	HH72	Songpan–Ganzi	Hehuahu	0·70	U1	Pl (3) + Phl (1)	Pl + Phl + Fe–Ti
14	YB55	Songpan–Ganzi	Yongbohu	0·44	T	Pl (3) + Sani (1) + Qz (1)	Pl + Bi + Sani + Qz
15	YS02	Songpan–Ganzi	Yanghu	0·66	U2	Cpx (2) + Opx (1) + Pl (2)	Sani + Fe–Ti + G
16	QQ08	Songpan–Ganzi	Qiangbaqian	0·54	S3	Cpx (2) + Pl (2)	Cpx + Sani + Bi
17	HS-69	Songpan–Ganzi	Heishibeihu	0·68	U1	Cpx (1) + Opx (1)	Cpx + Pl
17	HS07	Songpan–Ganzi	Heishibeihu	0·58	S2	Cpx (1) + Pl (3) + Sani (1)	Pl + Sani + Bi
18	AP-8	Songpan–Ganzi	Atamupaxia	0·46	S3	Bi (2) + Pl (1) + Sani (2)	Pl + Sani + Bi + Ap
19*	JH23	Songpan–Ganzi	Jingyuhu	0·66	U1	Cpx (1) + Pl (2)	Cpx + Pl
19*	JH6	Songpan–Ganzi	Jingyuhu	0·67	U1	Cpx (3) + Lc (1)	Cpx + Pl + Fe–Ti
19	JH9	Songpan–Ganzi	Jingyuhu	0·58	S3	Cpx (2) + Pl (2) + Sani (1)	Pl + Sani + Bi + Ap
20*	XT8	Songpan–Ganzi	Xiongyingtai	0·60	S2	Cpx (1) + Pl (3) + Sani (1)	Pl + Sani + Cpx + Ap
20	XT16	Songpan–Ganzi	Xiongyingtai	0·60	S2	Cpx (1) + Pl (3)	Cpx + Pl + Ap + Fe–Ti
21	AH63	Songpan–Ganzi	Ashikule	0·65	U2	Cpx (2) + Pl (2) + Sani (1)	Pl + Sani + Cpx + Fe–Ti
21	AH-7	Songpan–Ganzi	Ashikule	0·49	S3	Pl (2) + Sani (1) + Bi (1)	Pl + Sani + Bi + Fe–Ti + Qz
22	QS22	Songpan–Ganzi	Quanshuigou	0·67	S2	Cpx (2) + Ol (1) + Phl (2)	Cpx + Pl + Ap + Fe–Ti
22	QS30	Songpan–Ganzi	Quanshuigou	0·59	S2	Cpx (2) + Pl (1) + Phl (1)	Cpx + Pl + Sani
23	YS72	Songpan–Ganzi	Dahongliutan	0·62	S3	Cpx (2) + Pl (2) + Sani (1)	Pl + Sani + Ap + G
24*	KX91	Songpan–Ganzi	Kangxiwa	0·64	S2	Cpx (2) + Pl (2)	Cpx + Pl
24*	KX84	Songpan–Ganzi	Kangxiwa	0·69	U1	Ol (2) + Cpx (1) + Pl (2)	Cpx + Pl + Fe–Ti
24*	KX67	Songpan–Ganzi	Kangxiwa	0·68	U2	Cpx (2) + Pl (2) + Ol (1)	Cpx + Pl + Ap
25	PL-7	North Kunlun	Pulu	0·67	U1	Cpx (2) + Pl (2) + Opx (1)	Cpx + Pl
25	PL-99	North Kunlun	Pulu	0·66	S2	Cpx (1) + Pl (3) + Ol (1)	Cpx + Pl + Bi
25	PL-58	North Kunlun	Pulu	0·53	S2	Pl (2) + Sani (2) + Bi (1)	Sani + Pl + Bi

Field number refers to number of volcanic field in Fig. 1a. Rock type is determined by Fig. 3a. Names shown by letters are as follows. S1, trachybasalt; S2, basaltic trachyandesite; S3, trachyandesite; T, trachyte; U1, tephrite; U2, phonotephrite; U3, tephriphonolite. Ap, apatite; Bi, biotite; Cpx, clinopyroxene; Fe–Ti, Fe–Ti oxides; G, glass; Ha, haüyne; Lc, leucite; Ne, nepheline; Nos, nosean; Ol, olivine; Opx, orthopyroxene; Phl, phlogopite; Pl, plagioclase; Qz, quartz; Sani, sanidine; Tit, titanite. Proportions in per cent of phenocrysts are shown in parentheses (volume %).
*Samples contain mantle xenoliths.

Table 3: Major and trace element analyses of the representative potassic and ultrapotassic magmatic rocks in north Tibet

Field no.:	1	1	2	2	2	2	2	2	3
Sample no.:	G26	G68	G98-3	G98-1	G98-6	G98-14	G98-9	G98-0	JC973
Terrane:	North Qiangtang	North Qiangtang	North Qiangtang	North Qiangtang	North Qiangtang	North Qiangtang	North Qiangtang	North Qiangtang	North Qiangtang
Locality:	Yulinshan	Yulinshan	Bamao-qiongzong	Bamao-qiongzong	Bamao-qiongzong	Bamao-qiongzong	Bamao-qiongzong	Bamao-qiongzong	Bandaohu
Age (Ma):	28·7	28·7	26·5	26·5	26·5	26·5	26·5	26·5	39·9
SiO_2	57·69	57·44	47·36	50·24	46·47	47·58	48·34	53·11	49·43
TiO_2	1·31	1·16	1·07	1·20	0·75	1·36	1·45	1·38	1·39
Al_2O_3	14·24	18·37	13·80	12·02	12·90	13·12	12·87	15·26	14·86
Fe_2O_3*	6·77	7·92	12·34	8·11	12·19	9·66	10·92	9·86	10·32
MnO	0·15	0·13	0·11	0·14	0·12	0·09	0·11	0·14	0·14
MgO	3·61	0·91	8·06	8·42	9·02	7·15	8·04	5·71	6·34
CaO	5·50	6·06	10·76	10·40	12·06	12·12	11·01	7·60	9·93
Na_2O	3·55	3·01	2·95	2·89	2·33	3·72	2·27	2·14	2·05
K_2O	6·68	4·85	3·31	6·32	3·88	4·81	4·42	4·24	4·88
P_2O_5	0·48	0·14	0·23	0·25	0·26	0·39	0·57	0·56	0·65
LOI	2·55	2·33	0·62	1·24	1·48	2·41	2·11	1·33	1·83
Mg-no.	0·57	0·22	0·62	0·72	0·65	0·65	0·65	0·59	0·60
La	376	348	423	405	401	366	236	197·0	219
Ce	685	589	715	658	625	554	462	368	314
Pr	71·5	57·2	72·5	65·3	67·2	60·7	51·7	38·6	37·2
Nd	194	166	201	208	215	172	162	117·0	119
Sm	28·7	27·3	38·1	34·7	36·1	28·1	28·1	22·9	21·4
Eu	6·74	5·38	9·31	8·61	8·46	7·17	6·49	5·05	5·36
Gd	18·04	15·70	19·30	18·50	17·16	15·08	12·86	12·32	12·20
Tb	2·42	2·01	2·36	2·28	2·07	1·84	1·41	1·43	1·64
Dy	11·54	9·58	10·30	9·65	9·27	8·89	7·08	7·18	8·29
Ho	1·97	1·65	1·64	1·56	1·35	1·51	1·48	1·23	1·48
Er	4·69	4·37	4·27	4·02	3·97	4·16	4·11	2·97	3·96
Tm	0·66	0·61	0·61	0·58	0·64	0·59	0·61	0·43	0·63
Yb	4·18	4·12	3·63	3·84	4·31	3·95	3·89	2·68	4·07
Lu	0·56	0·64	0·52	0·57	0·67	0·56	0·61	0·39	0·59
Sc	9·42	6·49	25·6	23·3	23·5	20·6	21·6	15·30	18·2
V	98·5	79·1	198·4	205·3	186·2	177·3	180·2	108·7	126·9
Cr	70·9	23·8	495·0	389·2	440·5	376·2	401·8	221·8	211·9
Co	14·9	11·4	38·4	35·3	26·5	20·4	22·5	29·72	21·7
Ni	19·5	5·57	156·7	134·6	96·9	124·7	113·0	80·47	113·6
Cu	13·91	6·84	52·47	47·20	44·48	37·19	40·87	26·74	30·19
Zn	265·0	118·3	116·1	121·9	98·2	91·1	124·6	70·3	91·3
Ga	33·5	26·4	21·7	22·8	19·6	20·2	20·3	17·3	21·2
Rb	213	357	138	119	209	213	246	166	279
Sr	8561	6369	2326	2433	2664	2047	2611	3988	1706
Y	74·2	56·8	32·4	38·2	37·5	33·5	35·9	33·8	31·7
Zr	697	787	401	428	549	442	475	241	338
Nb	72·1	75·9	51·7	68·2	70·9	78·6	80·5	56·6	46·5
Ba	6062	6929	7434	7504	7544	7627	7569	4011	7108
Hf	15·8	14·0	8·2	10·6	12·9	11·5	12·8	11·78	7·26
Ta	3·72	3·41	1·11	1·04	1·68	2·36	2·98	2·37	2·71
Pb	116·5	188·9	76·3	68·6	72·6	67·1	68·2	38·9	58·5
Th	75·3	56·9	139·2	134·1	116·7	158·5	146·2	59·6	126·9
U	7·50	12·84	8·38	10·56	8·27	6·91	7·65	8·94	5·67
δCe	0·96	0·93	0·92	0·90	0·85	0·83	0·98	0·97	0·78
δEu	0·84	0·73	0·94	0·94	0·91	0·96	0·91	0·83	0·93

Table 3: continued

Field no.:	3	3	4	5	5	12	12	13	15	16
Sample no.:	JC9719	JC975	JC978	ZF91	ZF96	XY03	XY05	HH72	YS02	QQ08
Terrane:	North Qiangtang	North Qiangtang	North Qiangtang	North Qiangtang	North Qiangtang	Songpan–Ganzi	Songpan–Ganzi	Songpan–Ganzi	Songpan–Ganzi	Songpan–Ganzi
Locality:	Bandaohu	Bandaohu	Duogecuoren	Zhentouya	Zhentouya	Xiang–yanghu	Xiang–yanghu	Hehuahu	Yanghu	Qiangbaqian
Age (Ma):	39·9	39·9	39·7	44·7	44·7	10·6	10·6	12·7	16·5	14·9
SiO_2	48·66	47·16	49·49	61·77	59·10	52·28	62·08	47·29	50·20	57·62
TiO_2	1·46	1·52	1·60	0·73	1·22	1·61	1·44	1·55	1·05	1·18
Al_2O_3	13·54	12·79	12·93	16·46	15·19	13·99	15·82	13·56	13·28	16·53
Fe_2O_3*	9·12	10·58	11·52	5·48	6·63	7·40	6·87	8·91	8·95	6·43
MnO	0·17	0·15	0·09	0·13	0·09	0·11	0·06	0·14	0·14	0·13
MgO	9·17	9·21	7·62	2·16	3·41	6·34	1·82	8·46	6·95	3·11
CaO	9·88	10·43	9·14	4·75	6·41	9·39	4·00	10·48	10·28	6·68
Na_2O	2·41	2·17	2·05	3·40	3·32	3·29	3·01	3·62	3·76	3·53
K_2O	4·70	4·75	4·89	3·85	3·97	4·23	4·26	4·51	4·66	4·00
P_2O_5	0·89	1·23	0·66	1·28	0·68	1·37	0·64	1·48	0·71	0·80
LOI	2·87	2·03	0·46	1·39	0·54	2·57	0·16	1·91	2·75	1·82
Mg-no.	0·71	0·68	0·62	0·49	0·56	0·68	0·40	0·70	0·66	0·54
La	229	129	38·9	60·8	161	156	145	125	216	151
Ce	308	202	77·2	116	319	251	266	217	342	286
Pr	33·8	22·9	9·61	12·6	35·3	27·2	27·3	26·5	34·8	33·4
Nd	109	75·3	36·74	41·7	102	95·0	81·7	92·8	100	111
Sm	18·7	15·1	8·51	7·94	17·7	15·3	15·1	14·7	19·0	13·8
Eu	4·42	3·84	2·28	1·54	3·48	4·06	2·75	3·84	4·64	2·67
Gd	7·38	8·06	4·67	4·14	7·95	9·19	9·37	8·46	8·72	9·48
Tb	1·08	1·03	0·69	0·59	1·14	1·18	1·14	1·08	1·01	1·17
Dy	6·13	5·76	4·26	3·47	6·09	5·77	5·62	5·24	5·04	5·67
Ho	1·37	1·24	0·86	0·64	1·15	0·91	0·88	0·97	0·86	0·96
Er	3·61	3·44	2·51	1·75	2·91	2·31	2·12	2·38	1·97	2·09
Tm	0·52	0·46	0·38	0·25	0·38	0·33	0·28	0·34	0·26	0·29
Yb	3·11	2·96	2·54	1·61	2·13	2·17	1·66	1·98	1·54	1·94
Lu	0·47	0·44	0·38	0·24	0·31	0·32	0·26	0·31	0·21	0·28
Sc	22·6	22·1	20·5	11·1	15·5	22·8	7·14	27·8	21·9	7·64
V	148·6	166·9	135·8	40·8	77·6	186·9	55·5	196·5	164·9	66·8
Cr	410·9	524·7	405·7	38·6	58·1	325·6	15·0	464·9	362·5	45·5
Co	35·9	37·5	29·8	8·47	12·9	42·4	11·8	40·1	32·5	12·45
Ni	122·3	133·8	136·7	25·2	40·6	138·6	10·9	171·9	64·5	38·7
Cu	31·28	38·61	38·05	11·27	21·08	31·05	6·98	33·84	32·63	13·42
Zn	100·7	113·0	76·4	44·7	51·9	120·2	106·9	152·6	114·3	134·6
Ga	18·7	16·4	19·6	16·9	18·7	20·4	20·5	24·5	23·7	20·4
Rb	304	359	388	100	119	174	238	121	86·5	158
Sr	1668	1289	946	694	2789	1709	887	1394	1138	1176
Y	34·7	30·1	30·9	13·6	34·2	29·8	22·7	27·8	21·5	28·2
Zr	317	494	389	261	202	404	352	339	217	438
Nb	47·9	24·3	16·54	34·2	21·9	36·8	36·5	34·5	44·6	45·6
Ba	6869	6428	4985	1565	1342	2777	1684	1888	1846	1695
Hf	9·41	11·3	9·21	12·61	8·49	16·1	13·4	18·9	8·85	14·3
Ta	2·29	2·31	2·33	0·77	1·31	2·51	3·07	2·11	1·34	2·24
Pb	64·9	53·6	50·7	35·7	42·0	74·6	23·5	36·9	32·2	31·1
Th	108·9	25·9	21·6	42·9	46·8	42·9	34·7	32·6	28·5	30·1
U	6·34	5·86	5·98	3·45	5·27	5·34	5·48	3·02	5·46	5·83
δCe	0·76	0·84	0·95	0·97	0·99	0·87	0·97	0·88	0·87	0·95
δEu	0·97	0·96	1·00	0·74	0·78	0·97	0·66	0·96	0·96	0·68

Field no.:	17	17	19†	20†	20	21	22	23	24†	25	25
Sample no.:	HS-69	HS07	JH6	XT8	XT16	AH-7	QS22	YS72	KX84	PL-7	PL-58
Terrane:	Songpan–Ganzi	Songpan–Ganzi	Songpan–Ganzi	Songpan–Ganzi	Songpan–Ganzi	Songpan–Ganzi	Songpan–Ganzi	Songpan–Ganzi	Songpan–Ganzi	North Kunlun	North Kunlun
Locality:	Heishibeihu	Heishibeihu	Jingyuhu	Xiongyingtai	Xiongyingtai	Ashikule	Quanshuigou	Dahongliutan	Kangxiwa	Pulu	Pulu
Age (Ma):	3·7	3·7	10·7	9·3	9·3	0·96	6·4	0·28	3·8	1·27	1·27
SiO_2	45·82	54·46	46·26	53·35	52·92	57·52	50·70	56·64	44·12	45·19	55·97
TiO_2	1·43	1·60	1·48	1·08	1·13	1·05	1·57	1·18	1·39	1·68	1·68
Al_2O_3	13·34	13·57	13·33	13·40	14·23	13·73	13·27	14·29	13·93	11·62	14·51
Fe_2O_3*	10·22	9·33	10·34	10·69	9·53	9·19	9·19	6·58	9·94	10·97	9·00
MnO	0·14	0·07	0·12	0·16	0·15	0·08	0·14	0·12	0·15	0·16	0·11
MgO	8·70	5·19	8·30	6·40	5·82	3·61	7·37	4·27	8·76	9·19	4·13
CaO	10·70	7·76	10·41	7·38	8·13	6·24	9·92	5·15	12·32	12·01	7·26
Na_2O	3·19	3·77	3·79	3·15	3·16	3·48	2·15	3·56	3·36	3·66	2·60
K_2O	5·59	3·58	4·76	3·67	4·29	4·65	4·42	7·35	4·90	3·88	3·86
P_2O_5	0·87	0·67	1·20	0·71	0·63	0·45	1·27	0·84	1·12	1·63	0·88
LOI	1·19	2·46	1·15	0·34	1·21	0·70	1·14	0·59	2·34	0·79	0·68
Mg-no.	0·68	0·58	0·67	0·60	0·60	0·49	0·67	0·62	0·69	0·67	0·53
La	48·3	134	154	193	128	187	162	166	136	124	203
Ce	74·6	217	261	351	216	376	269	297	238	235	369
Pr	8·11	23·5	22·9	36·4	21·7	38·9	25·2	32·2	28·1	25·7	37·5
Nd	28·9	74·7	73·4	113	70·9	118	82·5	103	104	92·5	125
Sm	5·16	13·6	16·4	22·3	13·5	20·4	19·6	16·9	20·2	14·6	22·7
Eu	1·54	2·14	4·11	5·12	2·64	3·73	4·84	3·31	4·47	4·27	4·28
Gd	4·02	6·01	8·57	9·38	9·21	12·86	9·34	10·06	6·89	10·85	15·67
Tb	0·59	0·85	0·95	1·15	1·24	1·67	0·96	1·29	0·78	1·61	1·85
Dy	3·31	4·31	4·76	5·26	5·84	7·95	4·21	6·50	4·21	7·86	8·84
Ho	0·66	0·81	0·77	0·77	1·07	1·33	0·76	1·08	0·75	1·31	1·27
Er	1·73	2·03	1·96	1·74	2·72	2·93	1·99	2·21	1·87	3·03	2·87
Tm	0·27	0·28	0·29	0·22	0·40	0·41	0·30	0·24	0·28	0·46	0·43
Yb	1·76	1·84	1·96	1·47	2·87	2·65	2·14	1·27	1·78	2·97	2·86
Lu	0·26	0·27	0·30	0·23	0·44	0·40	0·33	0·18	0·27	0·51	0·47
Sc	24·7	14·2	22·9	22·1	18·3	10·4	24·4	11·5	25·1	22·9	11·3
V	188·9	142·6	190·5	179·6	116·3	75·3	128·9	125·4	240·8	181·5	98·3
Cr	419·3	51·3	410·8	338·9	241·1	69·6	389·2	68·7	471·5	411·9	68·7
Co	38·7	24·4	37·7	34·8	20·2	15·7	34·7	18·5	38·3	41·3	30·9
Ni	167·2	95·3	149·5	109·7	96·5	46·8	142·5	72·8	161·9	162·3	56·2
Cu	38·46	31·20	48·36	29·48	22·47	12·39	30·45	15·62	37·08	26·66	14·97
Zn	139·5	110·9	131·3	125·5	85·5	74·2	149·5	118·5	141·6	113·9	81·6
Ga	22·6	21·5	20·5	19·0	18·3	21·6	17·2	20·7	18·9	20·8	18·2
Rb	79·4	111	138	96·8	138	149	126	136	131	101	102
Sr	684	866	1698	1239	1106	994	1788	1507	1681	1068	1012
Y	27·2	17·6	23·6	22·8	18·6	28·4	25·7	20·4	23·5	28·3	28·6
Zr	415	315	346	239	254	521	369	472	415	401	394
Nb	18·7	40·9	43·8	25·7	29·4	45·8	92·1	28·9	41·7	37·4	38·8
Ba	988	1188	2426	1978	1246	1755	2008	2004	2003	1372	1673
Hf	7·4	13·5	12·5	16·5	10·1	13·5	10·4	12·1	10·1	15·7	11·0
Ta	1·88	1·68	3·19	0·69	2·54	2·19	2·66	1·26	2·83	1·88	2·27
Pb	35·5	37·2	28·3	26·9	39·3	36·2	51·6	36·5	20·5	28·6	35·3
Th	13·6	28·2	24·5	19·6	28·5	34·2	59·24	40·0	14·4	26·3	37·9
U	7·64	6·58	4·66	2·38	5·01	4·49	7·26	6·27	3·37	5·12	7·38
δCe	0·84	0·87	0·96	0·96	0·92	1·03	0·93	0·93	0·90	0·97	0·96
δEu	1·00	0·62	0·95	0·92	0·68	0·66	0·96	0·72	0·93	0·99	0·66

Major element oxide contents are normalized to 100 wt % on a volatile-free basis. Field number refers to number of the volcanic field in Fig. 1a. Age (Ma) is average value of the ages of the volcanic fields calculated from all of age data shown in Table 1. Mg-number = $Mg/(Mg + Fe^{2+})$, calculated assuming $Fe_2O_3/(FeO + Fe_2O_3) = 0{\cdot}20$. δCe is the ratio of chondrite-normalized Ce concentration to the expected concentration of Ce assuming no anomaly of Ce, and similarly for δEu. The normalization factors for the calculations are from Sun & McDonough (1989). The complete dataset may be downloaded from the *Journal of Petrology* website at http://www.petrology.oxfordjournals.org/.

*Total iron is given as Fe_2O_3.

†Samples contain mantle xenoliths.

Table 4: Ages of the main tectonic suture zones in north Tibet

No.*	Name of suture	Emplaced location of suture	Age of suture (Ma)	Subducted direction	Data sources
I	Kudi	North Kunlun/South Kunlun	Late Ordovician–Early Silurian	southward	[1,2]
II	South Kunlun	South Kunlun/Songpan–Ganzi	260 Ma	northward	[3,4,5]
III	Jinsha	Songpan–Ganzi/North Qiangtang	Early Carboniferous–Early Permian	southward	[6,7]
IV	Lancang	North Qiangtang/South Qiangtang	Devonian–Carboniferous	northward	[8,9]

*Suture number refers to number of the suture in Fig. 1a.
Data sources: [1] Xu & Pan (1993); [2] Pan *et al*. (1998); [3] Yang *et al*. (1996); [4] Guo *et al*. (1998); [5] Pan & Bian (2000); [6] Wang *et al*. (2000); [7] Yin & Harrison (2000); [8] Yang (1998); [9] Mo *et al*. (2003).

the southern margin of the North Kunlun terrane was a passive continental margin from Late Proterozoic times, with an ocean (Proto-Tethys) to the south separating it from the South Kunlun terrane. Subduction of Proto-Tethys oceanic lithosphere beneath the South Kunlun terrane occurred during Late Proterozoic to Early Palaeozoic times (Matte *et al*., 1996; Pan, 1996; Pan & Bian, 2000). The closure of the Proto-Tethys ocean during the Late Ordovician to Early Silurian, around 450 Ma (Xu & Pan, 1993; Pan *et al*., 1998), resulted in the collision of the North Kunlun and South Kunlun terranes and the formation of the Kudi suture (I). The Kudi suture (Fig. 1) is represented by an ophiolitic assemblage that includes serpentinized harzburgites, dunites, gabbros and pillow basalts, interbedded with deep-water cherts (Matte *et al*., 1996; Pan, 1996; Pan *et al*., 1998; Sobel & Arnaud, 1999; Mattern & Schneider, 2000; Pan & Bian, 2000; Xiao *et al*., 2002).

The South Kunlun and Songpan–Ganzi terranes probably formed a continuous continental block to the south of the Proto-Tethys ocean prior to the onset of subduction (e.g. Pan *et al*., 1998; Pan, 2000). A back-arc basin (South Kunlun ocean) gradually developed between the South Kunlun terrane and the Songpan–Ganzi terrane as a consequence of southerly subduction of Proto-Tethys oceanic lithosphere (Pan, 2000). The South Kunlun suture (II), located between the South Kunlun terrane to the north and the Songpan–Ganzi terrane to the south (Fig. 1), represents the closure of this back-arc basin. It comprises dismembered ophiolitic assemblages including ultramafic blocks, diabase, gabbro, serpentinized harzburgite, pillow lavas and chert (Molnar *et al*., 1987; Jiang *et al*., 2000; Pan & Bian, 2000). The age of the basalts is ~260 Ma on the basis of a whole-rock Rb–Sr isochron (Yang *et al*., 1996). Previous studies (Matte *et al*., 1996; Guo *et al*., 1998; Pan *et al*., 1998; Pan & Bian, 2000; Xu *et al*., 2000) have suggested that the South Kunlun ocean, now represented by the South Kunlun suture (II), may have subducted to the north during Late Palaeozoic times, based on the presence of contemporaneous subduction-related granitoids and volcanic rocks.

Wang *et al*. (2000) have proposed that the Palaeo-Tethys ocean basin opened in the Early Devonian. The closure of the main branch of Palaeo-Tethys, the Lancang ocean, is marked by the Lancang suture (IV) [Li, 1987; Zhou *et al*., 1989; YBGMR (Yunnan Bureau of Geology and Mineral Resources), 1990; Mo *et al*., 1991, 1993, 2003; Li *et al*., 1995; Yang, 1998; Wang *et al*., 2000], separating the North and South Qiangtang terranes (Fig. 1). The precise location and geodynamic setting of the Lancang suture, however, remain controversial (Hsü *et al*., 1995; Li *et al*., 1995; Kapp *et al*., 2000, 2003; Deng *et al*., 2002). The suture turns into a NW–SE-trending structure to the SE of the study area [Fig. 1b; also see (Yang 1998, fig. 1) and (Wang *et al*. 2000, fig. 1) for further discussion]. The Lancang suture is marked by dismembered Devonian–Carboniferous ophiolitic assemblages, which comprise serpentinite, harzburgite, gabbro, diabase, mafic pillow lavas, marine sediments and cherts (Li, 1987; Li *et al*., 1995; Yang, 1998; Wang *et al*., 2000). Paired with the ophiolitic suite, a Permo-Triassic arc volcanic rock sequence exists to the north and NE of the suture (Mo *et al*., 1991, 1993; Yang, 1998). These arc volcanic rocks consist of tholeiitic, calc-alkalic and shoshonitic series. There is a geochemical polarity, characterized by an increase in potassium and other incompatible trace elements (e.g. Rb and Ba), towards the NE within the volcanic belt (Mo *et al*., 1993; Yang, 1998). These indicate a mature volcanic arc, suggesting that the Langcang oceanic crust subducted northwards beneath the North Qiangtang terrane (Yang, 1998; Wang *et al*., 2000). It should be noted, however, that some workers have disagreed with the presence of the Lancang suture within the Qiangtang terrane (e.g. Deng, 1998; Pan *et al*., 1998).

Wang *et al*. (2000) have shown that the North Qiangtang terrane was connected with the southern Songpan–Ganzi terrane, forming an integrated continental block, during the initial stage of Lancang ocean subduction. A back-arc extensional basin gradually formed between the North Qiangtang terrane and the Songpan–Ganzi terrane as a consequence of northward

subduction. This phase of back-arc extension is considered to be a precursor of the Jinsha ocean now represented by the Jinsha suture zone (III) (Mo *et al.*, 1991, 1993; Wang *et al.*, 2000), which lies between the North Qiangtang terrane and the Songpan–Ganzi terrane (Fig. 1). The Jinsha suture is marked by mélanges with ophiolitic assemblages including ultramafic blocks, gabbros, picrites, pillow lavas and pelagic sediments (Pan, 1984; Dewey *et al.*, 1988; Pan *et al.*, 1998; Yang, 1998; Pan & Bian, 2000). Early Carboniferous and Early Permian radiolaria have been reported from chert and siliceous limestone interbeds within pillow basalts from the ophiolitic mélange (Wu, 1993; Feng *et al.*, 1997; Pan & Bian, 2000), indicating that the Jinsha oceanic lithosphere was generated at this time. The subduction direction of the Jinsha oceanic crust, however, remains controversial; this has been proposed to be southward (Dewey *et al.*, 1988; Pearce & Mei, 1988; Yin & Nie, 1996; Yang, 1998; Pan & Bian, 2000; Wang *et al.*, 2000; Yin & Harrison, 2000), northward (Coward *et al.*, 1988; Wu *et al.*, 1989; Li *et al.*, 1995), or both (Leeder *et al.*, 1988). There is a contemporaneous arc volcanic belt to the south of the Jinsha suture (Pearce & Mei, 1988; Pan *et al.*, 1998); however, the field relationships are complex because the suture has been strongly modified by post-collisional thrust systems.

The upper crust of the Songpan–Ganzi terrane comprises a 10–15 km thick sequence of Late Triassic flysch sediments deposited in a series of sedimentary basins on the passive continental margin of the North China block (Kapp *et al.*, 2003). A change from marine to non-marine sedimentation during the Early Jurassic is considered to record the accretion of the Qiangtang terrane to the Eurasian margin (Dewey *et al.*, 1988).

Based on the above, it is likely that the lithosphere beneath the North Qiangtang, Songpan–Ganzi and South Kunlun terranes has been geochemically enriched by both southward subduction of the Proto-Tethys oceanic lithosphere and northward subduction of the Palaeo-Tethys oceanic lithosphere. Because both the South Kunlun ocean (marked by the South Kunlun suture) and the Jinsha ocean (recorded by the Jinsha suture) (Fig. 1) initiated as back-arc extensional basins (Pan, 2000; Wang *et al.*, 2000), the lithosphere beneath the Songpan–Ganzi terrane could have been metasomatized during the early periods of the subduction of both the Proto-Tethys and the Palaeo-Tethys oceans, prior to the formation of the back-arc basins, although the Songpan–Ganzi terrane was far from the contemporaneous subduction zones.

The final closure of the South Kunlun, Jinsha and Lancang oceans in the Late Triassic led to the amalgamation of the South Kunlun, Songpan–Ganzi, North Qiangtang and South Qiangtang terranes (Pan *et al.*, 1998; Pan & Bian, 2000; Wang *et al.*, 2000). These continent–continent collisions gave rise to structural deformation, regional metamorphism of varying degrees, disruption of the ophiolitic mélanges and intracontinental subduction along previous zones of oceanic crust subduction (Pan *et al.*, 1998). Triassic synorogenic (syn-collisional) granitoids and intermediate to acidic arc volcanic rocks are mainly distributed within the South Kunlun terrane, the Qaidam terrane, the Songpan–Ganzi terrane and the North Qiangtang terrane (Harris *et al.*, 1988*a*; Pan *et al.*, 1998; Pan & Bian, 2000; Zhang *et al.*, 2000). Following this period of terrane amalgamation, the whole northern part of the Tibetan Plateau experienced strong intracontinental deformation from the Late Triassic.

PETROGRAPHY

The igneous rocks studied are aphyric to weakly porphyritic with <10% (by volume) phenocrysts; mafic samples contain <5% (by volume) phenocrysts. The phenocryst assemblage in the more mafic rocks consists mainly of olivine, orthopyroxene, clinopyroxene, phlogopite, plagioclase and alkali feldspar set in a microcrystalline matrix of plagioclase, alkali feldspar, pyroxene, biotite, apatite and Fe–Ti oxides. The phenocryst minerals in the more evolved rocks include sanidine, quartz, subordinate plagioclase and biotite; the groundmass comprises alkali feldspar, quartz, biotite, Fe–Ti oxides and glass. Some strongly undersaturated rocks (e.g. samples from the North Qiangtang terrane) contain phenocrysts of leucite, clinopyroxene, olivine, nepheline, nosean, haüyne, phlogopite and Fe–Ti oxides; their groundmass consists of sanidine, clinopyroxene, nosean, haüyne, apatite, titanite, Fe–Ti oxides and glass (Table 2).

ANALYTICAL TECHNIQUES

All of the analysed samples are petrographically fresh and show no evidence of significant hydrothermal alteration or weathering. Samples 2–3 kg in weight were cut into several thin slices. Fresh slices were cleaned three times using deionized water, dried, and then crushed in a tungsten carbide swing mill. To minimize contamination, only pieces of samples that did not come directly into contact with the mill were powdered in an agate mortar for subsequent major element, trace element and Sr–Nd–Pb isotope analysis.

For major element analyses, sample powders (1·2 g) were fused with $Li_2B_4O_7$ (6 g) in a CLAISSEFLUXER VI (Canada) fusion furnace at 1050°C for 20 min. Whole-rock major element oxide contents were analysed on fused glass discs with a Phillips PW1400 sequential X-ray fluorescence spectrometer (XRF) at the Institute of Geology and Geophysics, Chinese Academy of Sciences, Beijing (IGGCAS). The analytical precision was better than 2% relative. Loss on ignition (LOI) was

determined after ignition at 1000°C for 10 h of 2 g rock powder. The detailed analytical procedure follows that reported by Zhang *et al.* (2002). Representative data are presented in Table 3. The complete dataset is included as an Electronic Appendix, which may be downloaded from the *Journal of Petrology* website at http://www.petrology.oxfordjournals.org/.

For rare earth element (REE) and trace element analyses, whole-rock powders (40 mg) were weighed and dissolved in distilled 1 ml HF and 0·5 ml HNO_3 ($HNO_3 : H_2O = 1 : 1$) in 7 ml Savillex Teflon screw-cap capsules and then were ultrasonically stirred for 15 min. Subsequently, the solutions were evaporated at 150°C to dryness and the residue was digested with 1·5 ml HF and 0·5 ml HNO_3 ($HNO_3 : H_2O = 1 : 1$) in Teflon screw-cap capsules. Then, the solutions were heated at 130°C initially and at up to 170°C for 24 h by gradually increasing the temperature during this time. The solutions were then heated at 170°C for 10 days, dried and redissolved in 2 ml HNO_3 ($HNO_3 : H_2O = 1 : 1$) in the capsules. The solutions were heated at 150°C for 5 h and then evaporated, dried and redissolved in 2 ml HNO_3 ($HNO_3 : H_2O = 1 : 1$) and 2 ml 1% HNO_3 at 150°C for 5 h in screw-cap capsules, to ensure that the samples were completely dissolved. The solutions were put into plastic beakers and then 1 ml 500 ppb In was added as an internal standard. Finally, the solutions were diluted in 1% HNO_3 to 50 ml before analysis.

The REE and trace element contents of the sample solutions were analysed by inductively coupled plasma mass spectrometry (ICP-MS) at IGGCAS using a Finnigan MAT system. A blank solution was prepared; the total procedural blanks were <50 ng for all the trace elements reported in Table 3. (Representative data analysed are presented in Table 3. The complete dataset is included as an Electronic Appendix, which may be downloaded from the *Journal of Petrology* website at http://www.petrology.oxfordjournals.org/.) During the analytical runs, frequent standard calibrations were performed to correct for instrumental signal drift following the procedure of Gao *et al.* (1999). Four replicates and two international standards (BHVO-1 and AGV-1) were prepared using the same procedure to monitor the analytical reproducibility. The discrepancy, based on repeated analyses of samples and international standards, is <5% for all the elements given in Table 3. Analyses of the international standards are in excellent agreement with the recommended values (Govindaraju, 1994), and deviate <6% from the published values (see the Electronic Appendix). The detailed analytical procedures follow those of Jin & Zhu (2000) and Guo *et al.* (2005).

For Rb–Sr and Sm–Nd isotope analyses, whole-rock chips of <20 mesh size were used. Before being ground to 200 mesh (75 μm) in an agate mortar, the chips were leached in purified 6N HCl for 24 h at room temperature to minimize the influence of surface alteration or weathering, especially for Sr isotopic ratios. Sample powders (60 mg) were spiked with mixed isotope tracers (^{87}Rb–^{84}Sr for Rb–Sr isotope analyses and ^{149}Sm–^{150}Nd for Sm–Nd isotope analyses), then dissolved with a mixed acid ($HF : HClO_4 = 3 : 1$) in Teflon capsules for 7 days at room temperature. Rb and Sr and REE fractions were separated in solution using AG50W×8 (H^+) cationic ion-exchange resin columns. Sm and Nd were separated from the other REE fractions in solution using AG50W×8 (H^+) cationic ion-exchange columns and P507 extraction and eluviation resin. The collected Sr and Nd fractions were evaporated and dissolved in 2% HNO_3 to give solutions for analysis by mass spectrometry. Isotopic measurement was performed on a VG354 mass spectrometer (UK) at IGGCAS; the data are presented in Table 5. The mass fractionation corrections for Sr and Nd isotopic ratios were based on $^{86}Sr/^{88}Sr = 0{\cdot}1194$ and $^{146}Nd/^{144}Nd = 0{\cdot}7219$, respectively. The international La Jolla standard yielded $^{143}Nd/^{144}Nd = 0{\cdot}511862 \pm 7$ ($n = 12$, 2σ) (the recommended value is 0·511859) and international standard BCR-1 yielded $^{143}Nd/^{144}Nd = 0{\cdot}512626 \pm 9$ ($n = 12$) (the recommended value is 0·512638). The international standard NBS987 gave $^{87}Sr/^{86}Sr = 0{\cdot}710254 \pm 16$ ($n = 8$) (the recommended value is 0·710240) and international standard NBS607 gave $^{87}Sr/^{86}Sr = 1{\cdot}20032 \pm 30$ ($n = 12$) (the recommended value is 1·20039). The whole procedure blank is less than 2×10^{-10} g for Rb–Sr isotopic analysis and 5×10^{-11} g for Sm–Nd isotopic analysis. Analytical errors for Sr and Nd isotopic ratios are given as 2σ in Table 5. The $^{87}Rb/^{86}Sr$ and $^{147}Sm/^{144}Nd$ ratios were calculated using the Rb, Sr, Sm and Nd concentrations obtained by ICP-MS. The initial $^{87}Sr/^{86}Sr$ and $^{143}Nd/^{144}Nd$ ratios were calculated using average ages of the samples based on $^{40}Ar/^{39}Ar$, K–Ar dating and other analytical methods (Table 1).

For Pb isotope measurements, in order to minimize contamination from the atmosphere during the crushing process, 100 mesh powders of samples were used. 150 mg whole-rock powder was weighed and dissolved in Teflon capsules using concentrated HF at 120°C for 7 days. Pb was separated from the silicate matrix and purified using AG1×8 anionic ion-exchange columns with dilute HBr as eluant. The whole procedure blank is less than 1 ng. Pb isotopic ratios were measured with a VG354 mass spectrometer (UK) at IGGCAS. During the period of analysis repeat analyses of the international standard NBS981 yielded $^{204}Pb/^{206}Pb = 0{\cdot}059003 \pm 0{\cdot}000084$ ($n = 6$) (the certified value is 0·058998), $^{207}Pb/^{206}Pb = 0{\cdot}91449 \pm 0{\cdot}00017$ ($n = 6$) (the certified value is 0·914598), and $^{208}Pb/^{206}Pb = 2{\cdot}16691 \pm 0{\cdot}00097$ ($n = 6$) (the certified value is 2·168099). Pb isotope fractionations were corrected using correction factors from the certified values of the international

Table 5: Sr and Nd isotope compositions of the north Tibet potassic and ultrapotassic magmatic rocks

Field no.	Terrane	Sample no.	$^{87}Rb/^{86}Sr$	$^{87}Sr/^{86}Sr \pm 2\sigma$	$(^{87}Sr/^{86}Sr)_i$	εSr(i)	$^{147}Sm/^{144}Nd$	$^{143}Nd/^{144}Nd \pm 2\sigma$	$(^{143}Nd/^{144}Nd)_i$	εNd(i)
1	North Qiangtang	G26	0·0700	0·709021 ± 12	0·708992	64·26	0·0928	0·512324 ± 8	0·512307	−5·75
1	North Qiangtang	G68	0·1580	0·708684 ± 16	0·708620	58·97	0·1032	0·512146 ± 7	0·512127	−9·26
2	North Qiangtang	G98-3	0·1673	0·708243 ± 19	0·708180	52·69	0·1189	0·512318 ± 7	0·512297	−5·98
2	North Qiangtang	G98-1	0·1384	0·707982 ± 11	0·707930	49·14	0·1047	0·512307 ± 10	0·512289	−6·15
2	North Qiangtang	G98-6	0·2212	0·708249 ± 13	0·708166	52·49	0·1054	0·512213 ± 6	0·512195	−7·98
2	North Qiangtang	G98-14	0·2940	0·708862 ± 18	0·708751	60·80	0·1024	0·512106 ± 9	0·512088	−10·06
2	North Qiangtang	G98-9	0·2657	0·708019 ± 15	0·707919	48·98	0·1085	0·512039 ± 12	0·512020	−11·39
2	North Qiangtang	G98-0	0·1174	0·708324 ± 14	0·708280	54·11	0·1228	0·512385 ± 7	0·512364	−4·69
3	North Qiangtang	JC973	0·4616	0·708746 ± 19	0·708479	57·18	0·1129	0·512229 ± 8	0·512199	−7·54
3	North Qiangtang	JC9719	0·5141	0·707819 ± 14	0·707522	43·59	0·1078	0·512407 ± 6	0·512378	−4·04
3	North Qiangtang	JC975	0·7863	0·707638 ± 12	0·707183	38·79	0·1259	0·512488 ± 10	0·512454	−2·57
4	North Qiangtang	JC978	1·1567	0·708418 ± 15	0·707766	47·04	0·1454	0·512162 ± 11	0·512124	−9·03
5	North Qiangtang	ZF91	0·4049	0·710108 ± 17	0·709851	76·73	0·1195	0·512012 ± 12	0·511977	−11·77
5	North Qiangtang	ZF96	0·1205	0·709506 ± 11	0·709430	70·74	0·1089	0·512342 ± 7	0·512310	−5·27
12	Songpan–Ganzi	XY03	0·2871	0·707307 ± 16	0·707265	39·42	0·1011	0·512506 ± 11	0·512499	−2·45
12	Songpan–Ganzi	XY05	0·7565	0·710573 ± 12	0·710461	84·80	0·1162	0·511945 ± 9	0·511937	−13·41
13	Songpan–Ganzi	HH72	0·2447	0·707076 ± 10	0·707032	36·16	0·0996	0·512361 ± 8	0·512353	−5·25
15	Songpan–Ganzi	YS02	0·2141	0·707512 ± 11	0·707462	42·32	0·1192	0·512246 ± 14	0·512233	−7·48
16	Songpan–Ganzi	QQ08	0·3787	0·709713 ± 13	0·709633	73·11	0·0781	0·512206 ± 13	0·512198	−8·20
17	Songpan–Ganzi	HS-69	0·3272	0·706538 ± 13	0·706521	28·75	0·1122	0·512529 ± 7	0·512526	−2·09
17	Songpan–Ganzi	HS07	0·3599	0·708201 ± 16	0·708182	52·33	0·1143	0·512438 ± 7	0·512435	−3·86
19	Songpan–Ganzi	JH6	0·2292	0·707016 ± 13	0·706970	35·30	0·1400	0·512441 ± 9	0·512428	−3·74
20	Songpan–Ganzi	XT8	0·2204	0·707618 ± 14	0·707580	43·93	0·1239	0·512381 ± 6	0·512371	−4·90
20	Songpan–Ganzi	XT16	0·3519	0·708095 ± 16	0·708035	50·38	0·1195	0·512393 ± 8	0·512384	−4·66
21	Songpan–Ganzi	AH-7	0·4227	0·709103 ± 11	0·709098	65·28	0·1085	0·512226 ± 8	0·512225	−8·03
22	Songpan–Ganzi	QS22	0·1988	0·707210 ± 15	0·707192	38·32	0·1491	0·512429 ± 12	0·512423	−4·04
23	Songpan–Ganzi	YS72	0·2545	0·708394 ± 18	0·708393	55·26	0·1030	0·512266 ± 11	0·512266	−7·25
24	Songpan–Ganzi	KX84	0·2198	0·706689 ± 12	0·706677	30·97	0·1219	0·512442 ± 9	0·512439	−3·79
25	North Kunlun	PL-7	0·2666	0·708819 ± 10	0·708814	61·26	0·0991	0·512326 ± 10	0·512325	−6·07
25	North Kunlun	PL-58	0·2842	0·709029 ± 23	0·709024	64·24	0·1140	0·512113 ± 6	0·512112	−10·23

Field number refers to number of volcanic field in Fig. 1a. Chondritic uniform reservoir (CHUR) at the present day [$(^{87}Rb/^{86}Sr)_{CHUR} = 0·0847$ (McCulloch & Black, 1984); $(^{87}Sr/^{86}Sr)_{CHUR} = 0·7045$ (DePaolo, 1988); $(^{147}Sm/^{144}Nd)_{CHUR} = 0·1967$ (Jacobsen & Wasserburg, 1980); $(^{143}Nd/^{144}Nd)_{CHUR} = 0·512638$ (Goldstein *et al.*, 1984)] was used for the calculations. $\lambda_{Rb} = 1·42 \times 10^{-11}$ year^{-1} (Steiger & Jager, 1977); $\lambda_{Sm} = 6·54 \times 10^{-12}$ year^{-1} (Lugmair & Marti, 1978). Both εSr(i) and εNd(i) were obtained by using the average ages in the volcanic fields (Table 1).

standard NBS 981. The average 2σ uncertainty for measured ratios of $^{206}Pb/^{204}Pb$, $^{207}Pb/^{204}Pb$ and $^{208}Pb/^{204}Pb$ is 0·6%, 0·4% and 0·5% per a.m.u. (atomic mass unit), respectively. The Pb isotope data are presented in Table 6. Detailed sample preparation and analytical procedures for the Sr–Nd–Pb isotope measurements follow those of Zhang *et al.* (2002) and Fan *et al.* (2003).

RESULTS

Major and trace element geochemistry

The whole-rock geochemical data (Table 3 and Electronic Appendix) indicate that all of the analysed samples are potassic [K_2O/Na_2O (wt %) >1·0], except for two samples (QS30 and HS07) with K_2O/Na_2O <1 (0·92 and 0·95). Eight samples (QS22, YS72, DG08, G98-1, JC975, G98-11, JC973, JC978) have K_2O/Na_2O ratios >2; their MgO and K_2O contents are >3 wt %. These eight samples are considered to be ultrapotassic based on the criteria of Foley *et al.* (1987).

The compositions of the analysed samples are plotted in a total-alkali vs silica classification diagram (Le Bas *et al.*, 1986; Le Maitre *et al.*, 1989) in Fig. 3a and subdivided into three groups based on their locations within the North Qiangtang, Songpan–Ganzi and North Kunlun terranes. Samples from these terranes

Table 6: Pb isotope compositions of the north Tibet potassic and ultrapotassic magmatic rocks

Field no.	Terrane	Sample no.	$^{206}Pb/^{204}Pb$	$^{207}Pb/^{204}Pb$	$^{208}Pb/^{204}Pb$	$^{238}U/^{204}Pb$	$^{235}U/^{204}Pb$	$^{232}Th/^{204}Pb$	$(^{206}Pb/^{204}Pb)_i$	$(^{207}Pb/^{204}Pb)_i$	$(^{208}Pb/^{204}Pb)_i$
1	North Qiangtang	G26	18·908	15·698	39·248	4·066	0·030	42·171	18·890	15·697	39·188
1	North Qiangtang	G68	19·121	15·805	39·562	4·256	0·031	19·502	19·102	15·804	39·534
2	North Qiangtang	G98-3	19·012	15·703	39·216	6·876	0·051	118·069	18·984	15·702	39·061
2	North Qiangtang	G98-1	19·051	15·718	39·119	9·618	0·071	126·212	19·011	15·716	38·953
2	North Qiangtang	G98-6	18·941	15·719	39·204	7·160	0·053	104·395	18·911	15·718	39·067
2	North Qiangtang	G98-14	19·038	15·712	39·377	6·309	0·046	149·535	19·012	15·711	39·181
2	North Qiangtang	G98-9	18·867	15·702	39·017	6·910	0·051	136·471	18·838	15·701	38·838
2	North Qiangtang	G98-0	18·731	15·719	39·326	14·328	0·105	98·680	18·672	15·716	39·196
3	North Qiangtang	JC973	19·031	15·752	39·336	6·027	0·044	139·370	18·993	15·750	39·055
3	North Qiangtang	JC9719	18·846	15·688	39·224	6·045	0·044	107·317	18·808	15·686	39·008
3	North Qiangtang	JC975	18·810	15·634	38·827	6·836	0·050	31·270	18·767	15·632	38·764
4	North Qiangtang	JC978	19·054	15·732	39·286	7·398	0·054	27·667	19·008	15·730	39·232
5	North Qiangtang	ZF91	18·681	15·629	38·968	6·033	0·044	77·456	18·639	15·627	38·797
5	North Qiangtang	ZF96	18·784	15·713	38·984	7·882	0·058	72·321	18·729	15·710	38·824
12	Songpan–Ganzi	XY03	18·707	15·621	38·838	4·433	0·033	36·802	18·700	15·621	38·819
12	Songpan–Ganzi	XY05	18·885	15·725	39·208	14·424	0·106	94·443	18·862	15·724	39·159
13	Songpan–Ganzi	HH72	18·798	15·716	39·008	5·012	0·037	55·858	18·788	15·716	38·973
15	Songpan–Ganzi	YS02	18·714	15·680	38·686	10·554	0·078	56·911	18·687	15·679	38·640
16	Songpan–Ganzi	QQ08	18·826	15·684	39·136	11·745	0·086	62·704	18·799	15·683	39·090
17	Songpan–Ganzi	HS-69	18·814	15·706	39·115	13·178	0·097	24·224	18·806	15·706	39·111
17	Songpan–Ganzi	HS07	18·709	15·673	38·994	11·011	0·081	48·716	18·703	15·673	38·985
19	Songpan–Ganzi	JH6	18·755	15·668	39·012	10·233	0·075	55·664	18·733	15·667	38·973
20	Songpan–Ganzi	XT8	18·689	15·684	38·657	5·466	0·040	46·473	18·679	15·684	38·629
20	Songpan–Ganzi	XT16	18·587	15·605	39·047	7·991	0·059	46·893	18·572	15·604	39·019
21	Songpan–Ganzi	AH-7	18·753	15·739	39·006	7·728	0·057	60·780	18·752	15·739	39·003
22	Songpan–Ganzi	QS22	18·728	15·702	38·859	8·792	0·065	74·141	18·719	15·702	38·836
23	Songpan–Ganzi	YS72	18·713	15·651	38·724	10·759	0·079	70·930	18·713	15·651	38·723
24	Songpan–Ganzi	KX84	18·605	15·635	38·668	10·279	0·076	45·328	18·599	15·635	38·659
25	North Kunlun	PL-7	18·702	15·601	38·489	11·201	0·082	59·549	18·700	15·601	38·485
25	North Kunlun	PL-58	18·726	15·746	39·258	13·135	0·096	69·708	18·723	15·746	39·254

Field number refers to number of volcanic field in Fig. 1a. $\lambda_{U238} = 0{\cdot}155125 \times 10^{-9}$ year^{-1}, $\lambda_{U235} = 0{\cdot}98485 \times 10^{-9}$ year^{-1} and $\lambda_{Th232} = 0{\cdot}049475 \times 10^{-9}$year^{-1} (Steiger & Jager, 1977). $(^{207}Pb/^{204}Pb)_{NHRL} = 0{\cdot}1084 \times (^{206}Pb/^{204}Pb)_i + 13{\cdot}491$ (Hart, 1984); $(^{208}Pb/^{204}Pb)_{NHRL} = 1{\cdot}209 \times (^{206}Pb/^{204}Pb)_i + 15{\cdot}627$ (Hart, 1984). Initial Pb isotope ratios were obtained by using the average ages of the volcanic fields (Table 1).

overlap and define scattered trends that lie almost totally within the trachybasalt–basaltic trachyandesite–trachyandesite–trachyte and tephrite–phonotephrite–tephriphonolite–phonolite fields. A plot of K_2O vs SiO_2 (Fig. 3b) shows that the rocks belong to the shoshonitic magma series, except for one highly differentiated sample, which plots within the high-K calc-alkaline field.

Mg-numbers [= molar $Mg/(Mg + Fe^{2+})$ ratio, calculated assuming $Fe_2O_3/(FeO + Fe_2O_3) = 0{\cdot}20$] range from 0·22 to 0·72 (Table 3 and Electronic Appendix). Abundances of the compatible elements (e.g. MgO, Fe_2O_3, CaO, TiO_2, Ni, Sc, Cr) in the magmatic rocks of the different terranes display similar variation trends (Fig. 4). SiO_2 and Al_2O_3 increase, whereas CaO, Fe_2O_3, Ni and Cr (not shown) decrease, with decreasing MgO (Fig. 4a–d and l). This may be explained by fractional crystallization of clinopyroxene and olivine, which is consistent with petrographical observations that olivine and clinopyroxene phenocrysts predominate in the more mafic rocks (Table 2). However, no correlations exist between incompatible trace elements (e.g. Ba, Rb, Sr, Nb, Zr and Pb) and MgO (Fig. 4f–k). Contents of the incompatible trace elements Ba, Rb, Sr and Pb are

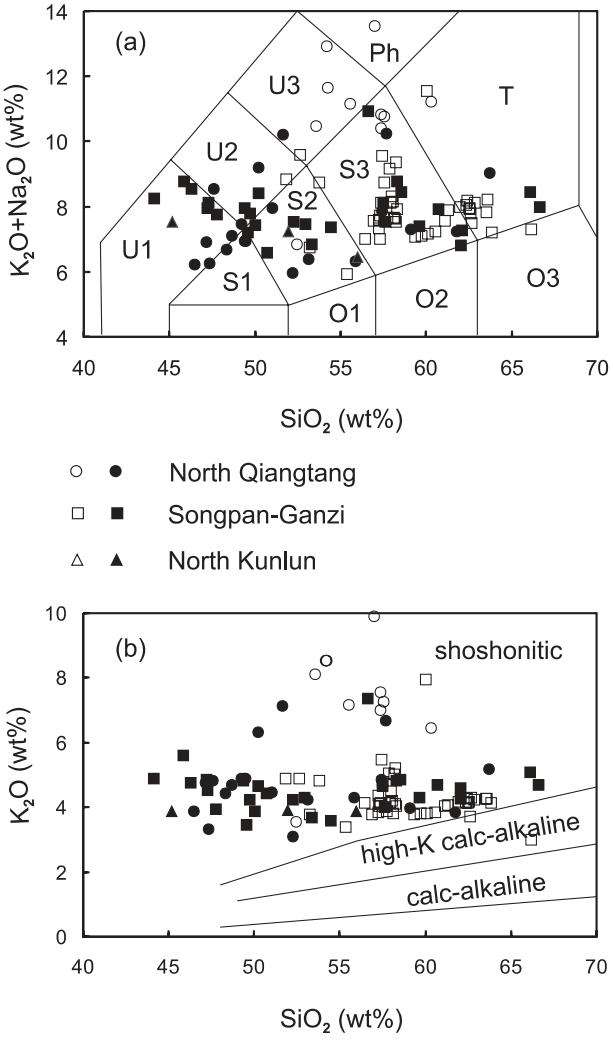

Fig. 3. (a) $K_2O + Na_2O$ (wt %) vs SiO_2 (wt %) for the potassic and ultrapotassic igneous rocks. All data plotted have been recalculated to 100 wt % on a volatile-free basis (see also Table 3 and the Electronic Appendix). Classification boundaries are from Le Bas *et al.* (1986) and Le Maitre *et al.* (1989). Filled and open symbols represent, respectively, data from this study and the published data of Arnaud *et al.* (1992), Turner *et al.* (1993, 1996*a*), Ding *et al.* (2003) and Williams *et al.* (2004). Rock types shown by letters are as follows: S1, trachybasalt; S2, basaltic trachyandesite; S3, trachyandesite; T, trachyte; U1, tephrite; U2, phonotephrite; U3, tephriphonolite; Ph, phonolite; O1, basaltic andesite; O2, andesite; O3, dacite. (b) K_2O (wt %) vs SiO_2 (wt %) diagram for the same samples as plotted in (a). Data have been normalized to 100 wt % volatile-free as indicated in Table 3 and the Electronic Appendix. The dividing lines show the classification boundaries from Rickwood (1989). Data sources and symbols are as in (a).

clearly higher in most samples from the North Qiangtang terrane than in those from the Songpan–Ganzi and North Kunlun terranes (Fig. 4f–h and k). Samples from the North Qiangtang terrane with high Ba, Rb, Sr and Pb concentrations do not show corresponding high LOI values, although the LOI values in the potassium-rich magmatic rocks must also reflect the presence of hydrous mineral phases (e.g. phlogopite). Moreover, the samples with high Ba, Rb, Sr and Pb concentrations are petrographically fresh (e.g. fresh plagioclase), further precluding the possibility of sample alteration.

Almost all of the samples with MgO >6 wt % have Mg-numbers >0·60; the highest Mg-number is 0·72 (sample G98-1; Table 3 and Electronic Appendix). This suggests that these samples represent relatively primitive magmas. On this basis, we define samples with MgO >6 wt % as primitive and those having MgO <6 wt % as evolved. To minimize the effects of magmatic differentiation and crustal contamination, only primitive samples were used to investigate the conditions of generation of the primary, mantle-derived magmas. Chondrite-normalized REE patterns (Fig. 5) and primitive mantle-normalized incompatible element diagrams for the primitive samples (Fig. 6) show strong incompatible element enrichment. Primitive mantle-normalized concentrations range from several times primitive mantle for heavy REE (HREE), Ti and Y to several hundred and even >1000 times for large ion lithophile elements (LILE) such as Rb, Ba, Th, U, K and Pb (Fig. 6). The mantle-normalized incompatible trace element patterns are distinguished by significantly negative Nb–Ta–Ti and positive Pb anomalies, despite the generally high contents of the elements Nb, Ta and Ti (Table 3 and Electronic Appendix). The average concentrations of Rb, Ba, Th, U, La, Ce, Pb, Sr, Nd, Sm and Eu are higher in the samples from the North Qiangtang terrane than in those from the Songpan–Ganzi and North Kunlun terranes; however, average contents of the high field strength elements (HFSE; Ta, Zr and Ti) are similar in the magmas of the three terranes (Table 3 and Electronic Appendix). Positive correlations are evident between La/Yb and La (Fig. 7a), and Ce/Pb and Ce (Fig. 7b); the slope defined by the samples from the North Qiangtang terrane is different from that for samples from the Songpan–Ganzi and North Kunlun terranes.

Sr–Nd–Pb isotope geochemistry

Sr–Nd–Pb isotope data for the primitive and evolved samples are plotted in Figs 8 and 9, respectively. All samples have relatively high values of $(^{87}Sr/^{86}Sr)_i$ (0·706521–0·710461), low $(^{143}Nd/^{144}Nd)_i$ (0·511937–0·512526) and high $(^{207}Pb/^{204}Pb)_i$ (15·601–15·804) and $(^{208}Pb/^{204}Pb)_i$ (38·485–39·534) at a given $(^{206}Pb/^{204}Pb)_i$ (18·572–19·102) (Tables 5 and 6). The Sr–Nd isotope compositions exhibit a negative correlation (Figs 8a and 9a). The Sr–Nd–Pb isotopic compositions of Global Subducting Sediment (GLOSS; Plank & Langmuir, 1998) and previously published data for potassium-rich igneous rocks from the three terranes (Arnaud *et al.*, 1992; Turner *et al.*, 1993, 1996*a*; Ding *et al.*, 2003;

Williams *et al.*, 2004) are shown for comparison (Fig. 9). In plots of $(^{208}Pb/^{204}Pb)_i$ vs $(^{206}Pb/^{204}Pb)_i$, and $(^{207}Pb/^{204}Pb)_i$ vs $(^{206}Pb/^{204}Pb)_i$ (Figs 8d, e and 9d, e), the samples studied define a diffuse array above and subparallel to the Northern Hemisphere Reference Line (NHRL; Hart, 1984). In all isotope projections, the potassium-rich magmatic rocks broadly overlap the field of GLOSS.

The primitive samples have relatively higher $^{87}Sr/^{86}Sr$ and $^{206}Pb/^{204}Pb$, and lower $^{143}Nd/^{144}Nd$ ratios in the North Qiangtang terrane compared with those in the Songpan–Ganzi and North Kunlun terranes (Fig. 8). In the Pb isotope diagrams (Fig. 8d and e), these samples define diffuse linear arrays within the GLOSS field. The evolved samples have similar Sr–Nd–Pb isotope ratios in the North Qiangtang, Songpan–Ganzi and North Kunlun terranes, although some of the evolved magmas have higher $^{206}Pb/^{204}Pb$ ratios in the North Qiangtang terrane compared with those in the Songpan–Ganzi and North Kunlun terranes (Fig. 9). In all Sr–Nd–Pb isotope diagrams, the data for the evolved samples from this study broadly overlap those of previous studies.

DISCUSSION

The major and trace element characteristics and Sr–Nd–Pb isotope compositions of the primitive and evolved magmatic rocks in north Tibet can provide constraints on the nature of the mantle source, processes of partial melting, crustal-level evolution of the magmas and geodynamic setting. Moreover, there may be a relationship between the petrogenesis of the post-collisional K-rich magmas and the uplift of northern Tibet.

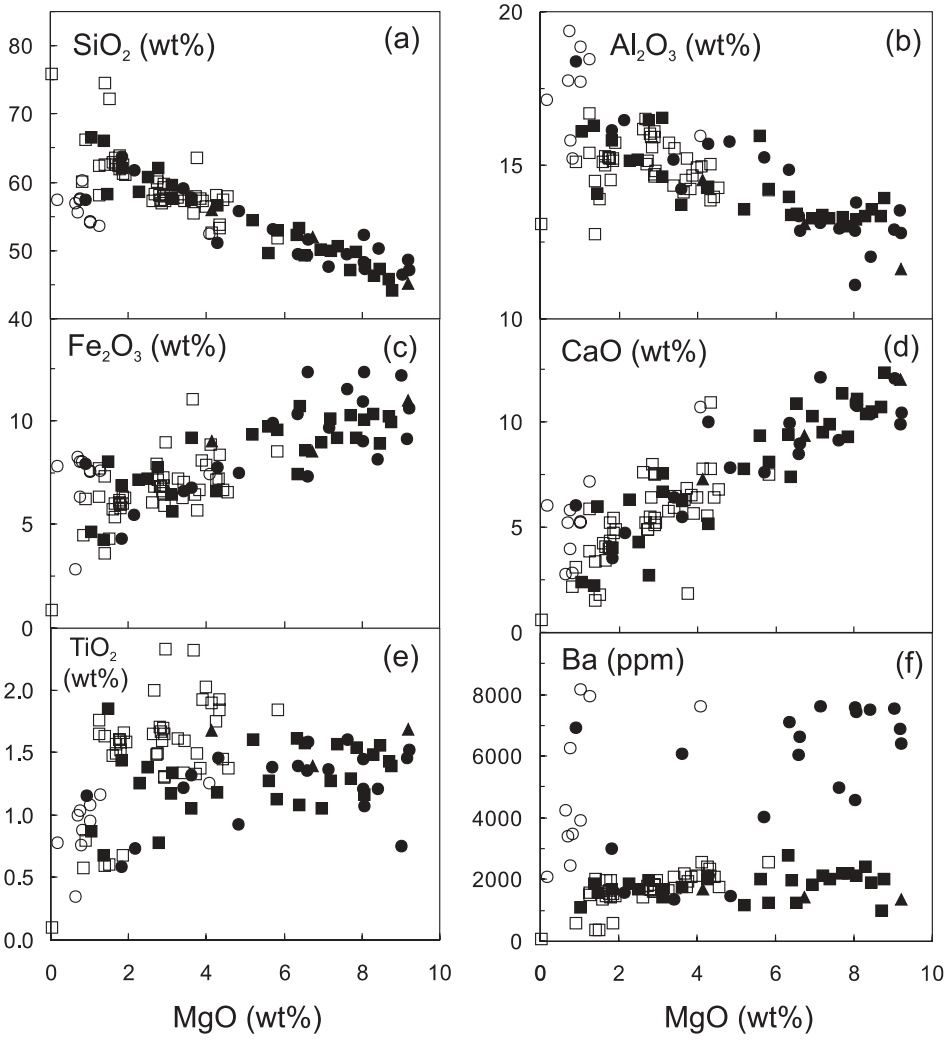

Fig. 4. Selected major element oxide (wt %) and trace element (ppm) concentrations vs MgO content (wt %) illustrating the broad compositional range of the potassium-rich magmatism in north Tibet. All the major element data have been recalculated to 100 wt % on a volatile-free basis (Table 3 and Electronic Appendix). Data sources and symbols are as in Fig. 3a.

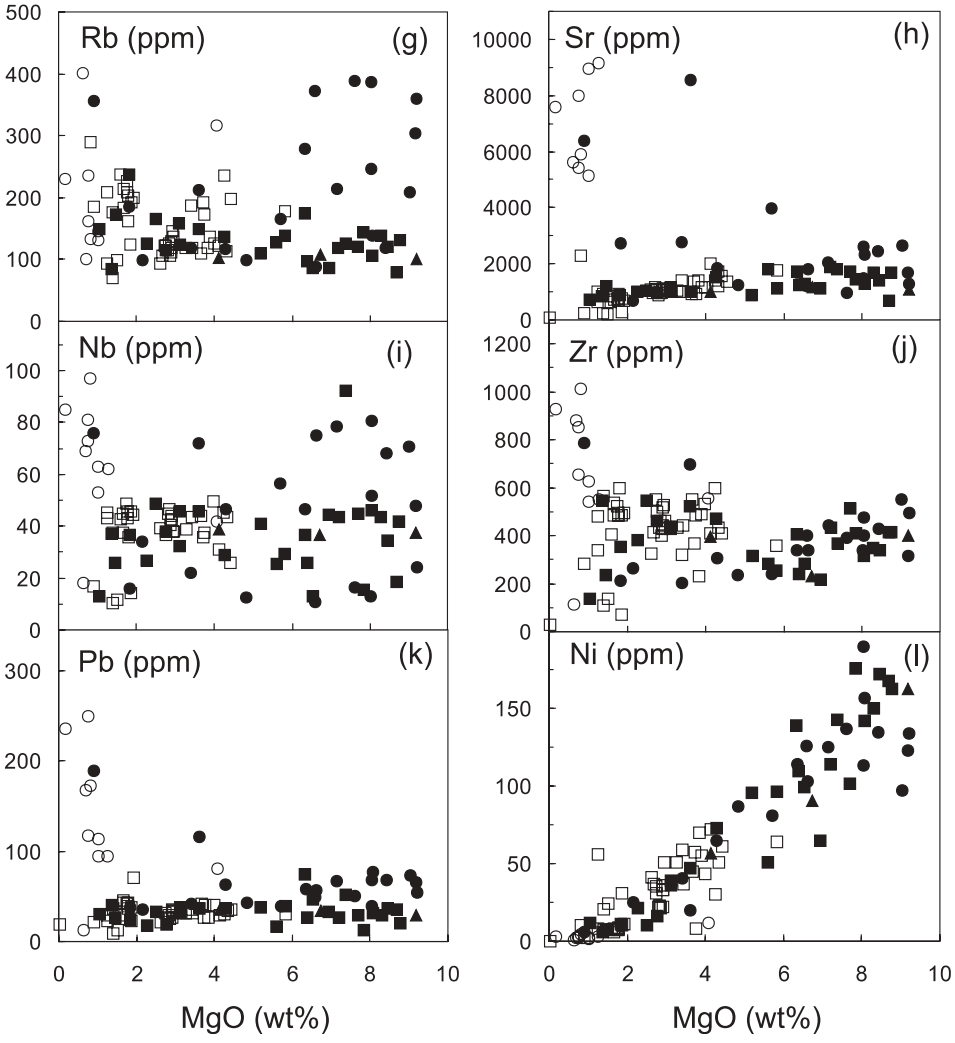

Fig. 4. Continued

Role of crustal contamination processes in the petrogenesis of the magmas

Combined assimilation and fractional crystallization

The broad negative correlation between $(^{87}Sr/^{86}Sr)_i$ and MgO (wt %) (Fig. 10) for the North Qiangtang and Songpan–Ganzi terranes suggests operation of combined processes of crustal assimilation and fractional crystallization (AFC) in the petrogenesis of the magmas. The range in $(^{87}Sr/^{86}Sr)_i$ for the primitive samples from the North Qiangtang terrane suggests that their mantle source was isotopically heterogeneous (Fig. 10a). In contrast, the primitive samples from the Songpan–Ganzi terrane are isotopically more homogeneous; however, the more evolved magmatic rocks appear to be extremely heterogeneous when data from the literature are included for comparison (Fig. 10b). In Fig. 11, we show the variation of $(^{87}Sr/^{86}Sr)_i$ vs Sr (ppm) for the magmatic rocks from the North Qiangtang and Songpan–Ganzi/North Kunlun terranes. The data define distinctly different arrays, suggesting that different crustal contamination (AFC) processes may have operated in the individual terranes.

Modelling energy-constrained assimilation and fractional crystallization

The energy-constrained assimilation and fractional crystallization (EC-AFC) model (Bohrson & Spera, 2001; Spera & Bohrson, 2001) provides a rigorous approach to the simulation of AFC processes. The rationale behind our EC-AFC model calculations is as follows. First, we select reasonable ranges of the initial parameters required in the EC-AFC model based on the isotopic and geochemical characteristics of the magmas in north Tibet (Tables 3 and 5, and Electronic Appendix), previous knowledge about upper mantle partial melting processes

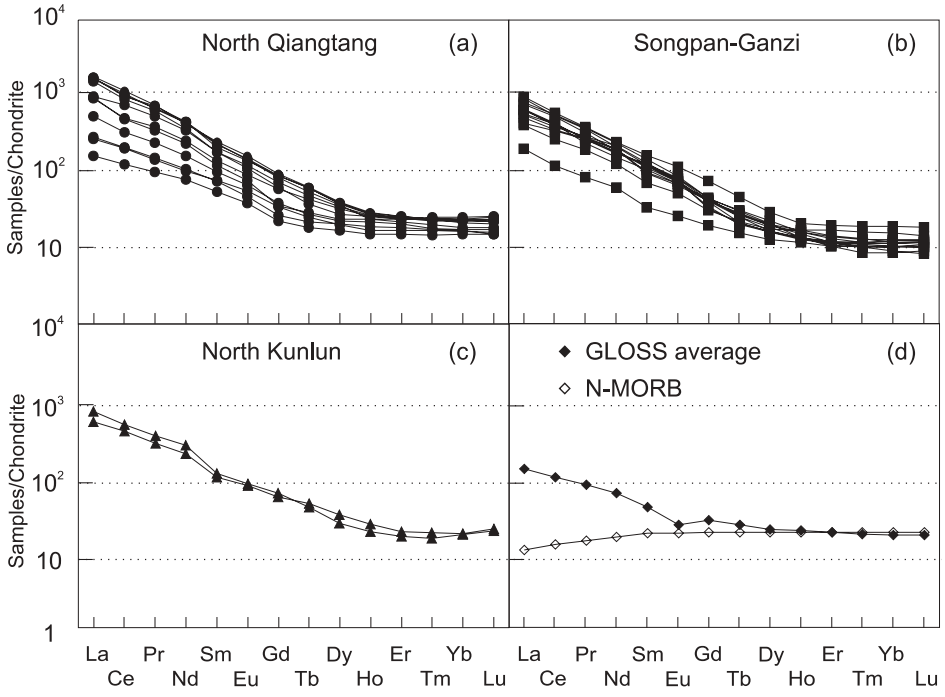

Fig. 5. Chondrite-normalized rare earth element diagrams; normalization factors are from Sun & McDonough (1989). To minimize the effect of magmatic differentiation and crustal contamination on the chondrite-normalized rare earth element patterns, only primitive samples with MgO >6 wt % are plotted. (a) The magmatic rocks in the North Qiangtang terrane; (b) the magmatic rocks in the Songpan–Ganzi terrane; (c) the magmatic rocks in the North Kunlun terrane; (d) GLOSS average (Plank & Langmuir, 1998) and N-MORB (Sun & McDonough, 1989). The symbols are as in Fig. 3a.

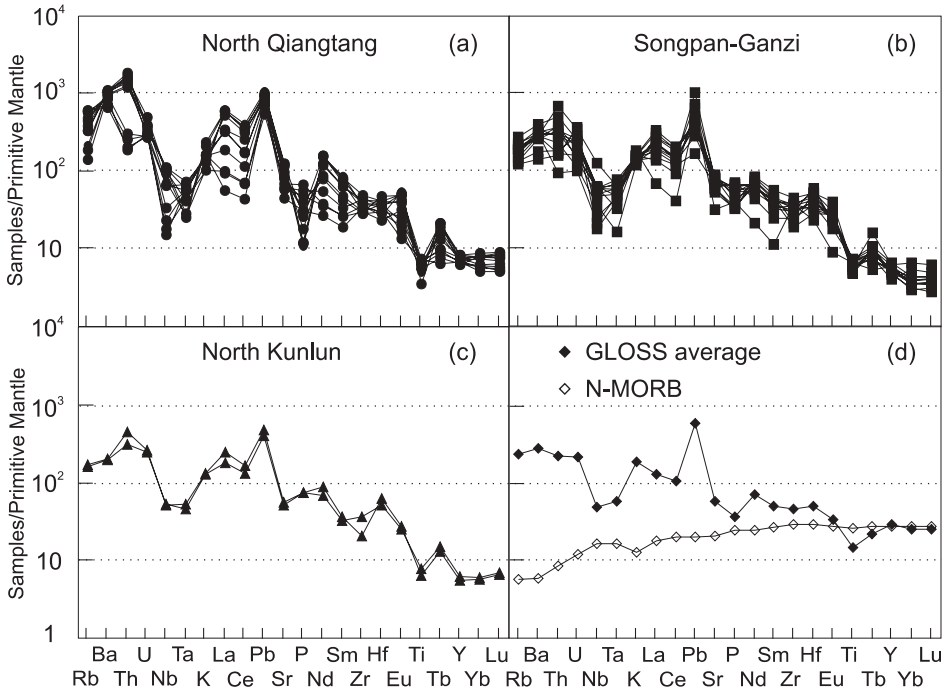

Fig. 6. Primitive mantle-normalized incompatible trace element diagrams; normalization factors are from Sun & McDonough (1989). To minimize the effect of magmatic differentiation and crustal contamination on the primitive mantle-normalized trace element patterns, only primitive samples with MgO >6 wt % are plotted. (a) The magmatic rocks in the North Qiangtang terrane; (b) the magmatic rocks in the Songpan–Ganzi terrane; (c) the magmatic rocks in the North Kunlun terrane; (d) GLOSS average (Plank & Langmuir, 1998) and N-MORB (Sun & McDonough, 1989). The symbols are as in Fig. 3a.

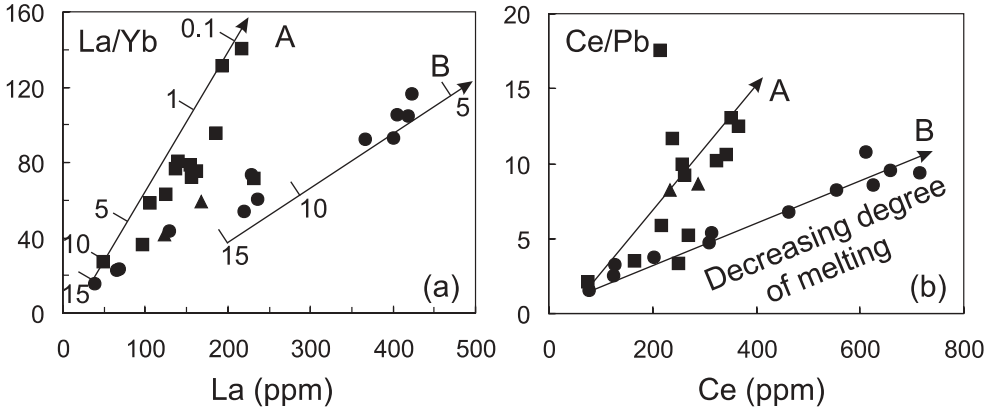

Fig. 7. (a) La/Yb vs La (ppm) diagram. (b) Ce/Pb vs Ce (ppm). To minimize the effect of magmatic differentiation and crustal contamination, only primitive samples with MgO >6 wt % are plotted. Arrowed lines A and B in (a) represent non-model batch melting trends for the Songpan–Ganzi and North Qiangtang terranes, respectively. Tick marks in (a) indicate the degree of partial melting in per cent. The detailed calculation procedures are explained in the footnote to Table 10. No Pb partition coefficient data for residual rutile and titanite in mantle source are available in the literature. Consequently, the trends labelled A and B in (b) are purely schematic. The symbols are as in Fig. 3a.

and the likely composition of the local crust. Then, using selected values of these initial parameters within their ranges, we perform iterative calculations using the EC-AFC calculation program (http://magma.geol.ucsb.edu), progressively changing the set of parameters within their ranges until we obtain the best fit to the Sr contents and Sr isotopic compositions of the northern Tibetan magmatic rocks (Fig. 11). The output from our EC-AFC simulations provides model curves to fit the correlation trends between $(^{87}Sr/^{86}Sr)_i$ and Sr (Fig. 11) and also optimized values of the parameters that form the basis of the EC-AFC model (Tables 7 and 8). These parameters provide important constraints on the characteristics of the primitive magmas, the nature of the crustal contaminant and the relative depth at which AFC processes operate in each of the terranes.

Ranges of the initial parameters of EC-AFC model

There are two types of initial parameters in the EC-AFC model: thermal and compositional parameters (Bohrson & Spera, 2001). Our approach to the selection of initial values of the thermal parameters is as follows. We selected the magma liquidus temperature to be within the range 900–1600°C, assuming that the primary/parental K-rich magmas were generated by partial melting of the upper mantle beneath north Tibet; we also assumed that the initial temperature of the magma at the site of crustal contamination is equal to the liquidus temperature. We adopted the approach of Bohrson & Spera (2001) and selected the assimilant liquidus temperature, solidus temperature and initial temperature in the ranges 500–1400°C, 300–1200°C and 100–1000°C, respectively. The equilibration temperature (T_{eq}) is the temperature at which the EC-AFC processes cease. This is constrained to lie between 1600°C and 300°C; following Bohrson & Spera (2001), this value must be between the magma liquidus temperature and the solidus temperature of the assimilant. Values for the isobaric specific heat of the magma, the isobaric specific heat of the assimilant, crystallization enthalpy and fusion enthalpy are taken from Bohrson & Spera (2001) and are assumed to be constant (Table 7).

The compositional parameters required for calculation of the EC-AFC model are based on the isotopic and chemical characteristics of the primitive magmas and likely crustal assimilants. We have modelled the relationship between $(^{87}Sr/^{86}Sr)_i$ and Sr concentrations for EC-AFC processes in northern Tibet and compared them with the model curves of Bohrson & Spera (2001). For the North Qiangtang terrane, we selected the initial Sr content of the magma to range between 1000 and 9000 ppm, extending significantly beyond the range of primitive compositions observed (Table 3 and Electronic Appendix), and Sr isotope ratios from 0·7070 to 0·7090 based on the $(^{87}Sr/^{86}Sr)_i$ ratios of the primitive magmas (Table 5). For the Songpan–Ganzi and North Kunlun terranes, we selected the initial Sr content of the magma to range from 500 to 2000 ppm, according to the data in Table 3 and the Electronic Appendix, and Sr isotope ratios from 0·7060 to 0·7090 based on the $(^{87}Sr/^{86}Sr)_i$ of the primitive magmas (Table 5). For the North Qiangtang, Songpan–Ganzi and North Kunlun terranes, we selected both the residue/melt bulk distribution coefficient for Sr in the partial melt of the assimilant (D_a) and the phenocryst/melt bulk distribution coefficient for Sr in the primitive magma (D_m) to range from 0 to 5·5 on the basis of previous studies of EC-AFC processes (Bohrson & Spera, 2001). Assimilant Sr contents and Sr isotope ratios in the three basement terranes are taken from Liu (1999), Pan (2000) and Deng *et al.* (2002) (Table 7).

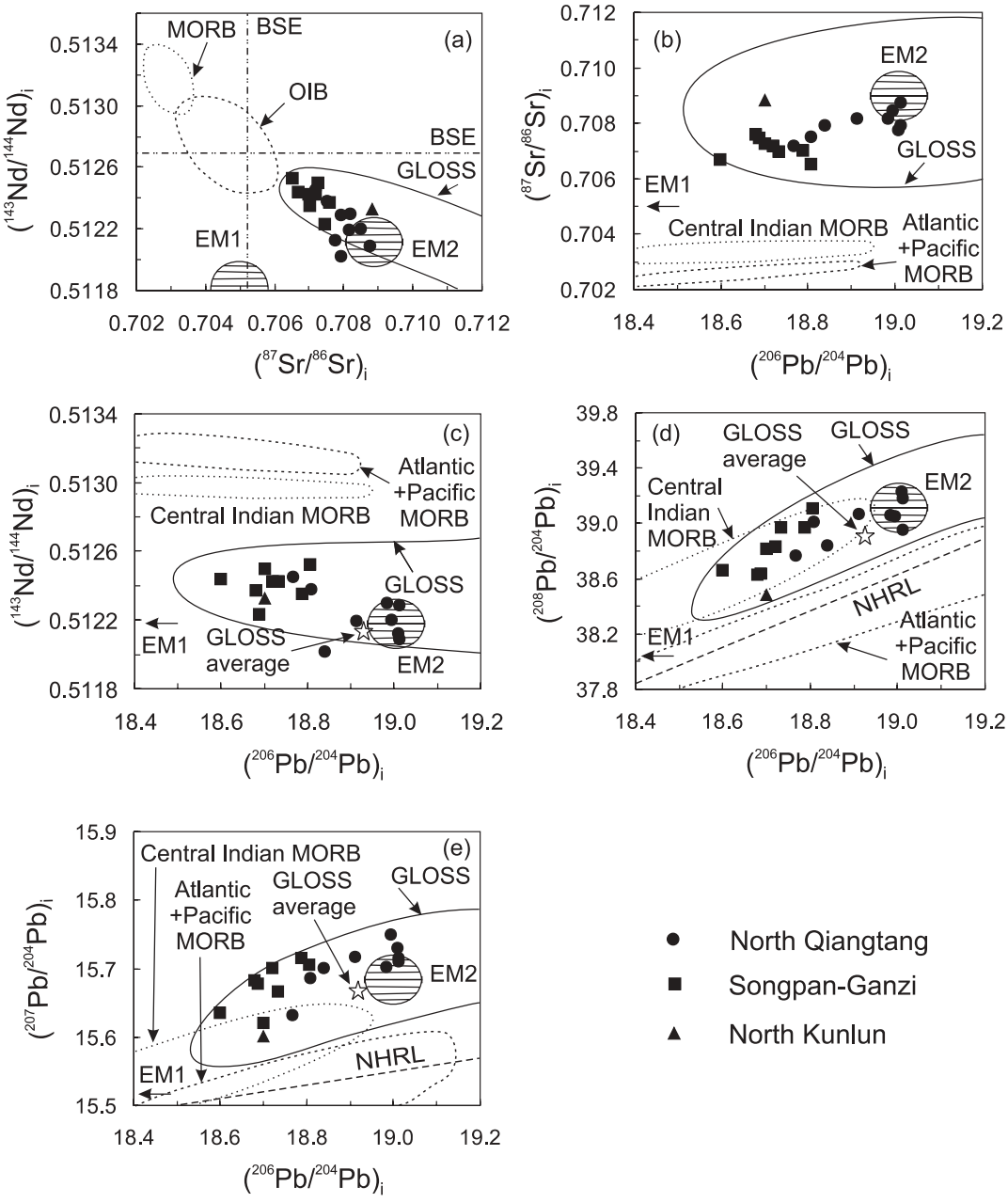

Fig. 8. (a) $(^{143}Nd/^{144}Nd)_i$ vs $(^{87}Sr/^{86}Sr)_i$. (b) $(^{87}Sr/^{86}Sr)_i$ vs $(^{206}Pb/^{204}Pb)_i$. (c) $(^{143}Nd/^{144}Nd)_i$ vs $(^{206}Pb/^{204}Pb)_i$. (d) $(^{208}Pb/^{204}Pb)_i$ vs $(^{206}Pb/^{204}Pb)_i$. (e) $(^{207}Pb/^{204}Pb)_i$ vs $(^{206}Pb/^{204}Pb)_i$. To minimize the effect of magmatic differentiation and crustal contamination, only primitive samples with MgO >6 wt % are plotted. No previously published data for primitive magmatic rocks with MgO >6 wt % are available. All data shown here are from this study. The symbols are as in Fig. 3a. Field for Central Indian MORB is from Mahoney *et al.* (1989) and Hofmann (1997). Field for Atlantic + Pacific MORB is from White *et al.* (1987) and Hofmann (1997). The continuous line outlines the field of Global Subducting Sediment (GLOSS; Plank & Langmuir, 1998). The open star shows the average composition of GLOSS (GLOSS average; Plank & Langmuir, 1998). The NHRL (Northern Hemisphere Reference Line; Hart, 1984), EM1 and EM2 (enriched mantle end-members; Zindler & Hart, 1986; Hofmann, 1997; Zou *et al.*, 2000), and MORB and OIB fields (Wilson, 1989; Hofmann, 1997) are shown for reference. BSE is Bulk Silicate Earth.

Calculated results of the above parameters in the EC-AFC model

Based on the above ranges and values of the initial parameters (Table 7), we performed iterative EC-AFC calculations by changing the initial parameters from minimum to maximum values within their respective ranges [for a detailed discussion of the EC-AFC model the reader is referred to Bohrson & Spera (2001) and Spera & Bohrson (2001)]. When the calculation results of the EC-AFC model provided the best fit to the actual

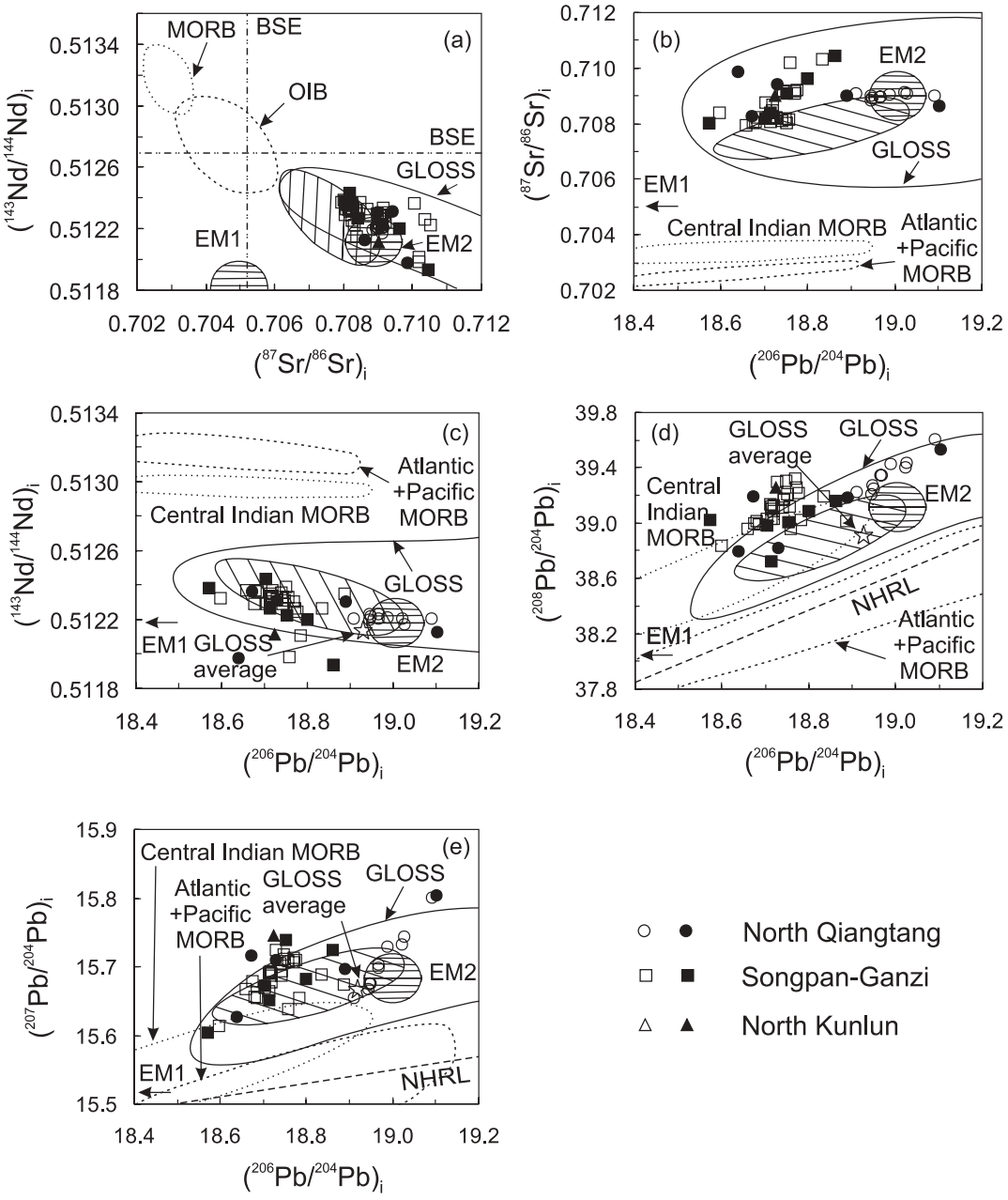

Fig. 9. (a) $(^{143}Nd/^{144}Nd)_i$ vs $(^{87}Sr/^{86}Sr)_i$. (b) $(^{87}Sr/^{86}Sr)_i$ vs $(^{206}Pb/^{204}Pb)_i$. (c) $(^{143}Nd/^{144}Nd)_i$ vs $(^{206}Pb/^{204}Pb)_i$. (d) $(^{208}Pb/^{204}Pb)_i$ vs $(^{206}Pb/^{204}Pb)_i$. (e) $(^{207}Pb/^{204}Pb)_i$ vs $(^{206}Pb/^{204}Pb)_i$. To show the effect of magmatic differentiation and crustal contamination on Sr–Nd–Pb isotope ratios, only relatively evolved samples with MgO <6 wt % are plotted. The diagonal shaded field is that of the primitive magmas with MgO >6 wt % defined in Fig. 8. Field for Central Indian MORB is from Mahoney *et al.* (1989) and Hofmann (1997). Field for Atlantic + Pacific MORB is from White *et al.* (1987) and Hofmann (1997). The continuous line outlines the field of GLOSS (Plank & Langmuir, 1998). The open star shows the average composition of GLOSS (GLOSS average; Plank & Langmuir, 1998). The NHRL (Northern Hemisphere Reference Line; Hart, 1984), EM1 and EM2 (enriched mantle end-members; Zindler & Hart, 1986; Hofmann, 1997; Zou *et al.*, 2000), and MORB and OIB fields (Wilson, 1989; Hofmann, 1997) are shown for reference. BSE is Bulk Silicate Earth. The symbols are as in Fig. 3a.

data trends (i.e. in Fig. 11 the model curves provided a good fit to the correlation of $^{87}Sr/^{86}Sr$ vs Sr for the individual terranes), we terminated the iteration and recorded the final values of the thermal and compositional parameters (Table 8).

For the North Qiangtang terrane, the best fit to the data shows that the assimilant liquidus temperature, solidus temperature and initial temperature are 1150°C, 900°C and 600°C, respectively. The magma liquidus temperature is 1300°C and the equilibration temperature

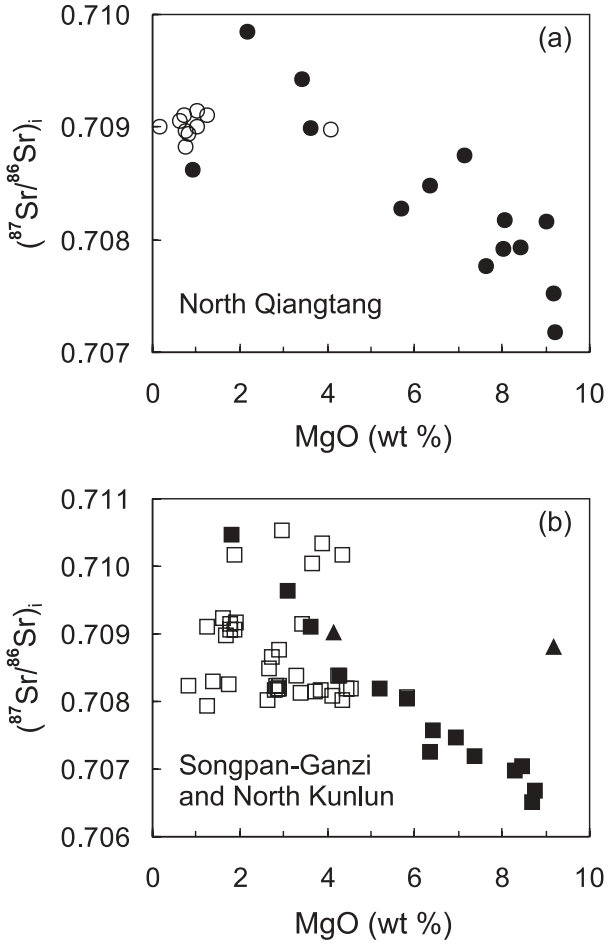

Fig. 10. Variation of $(^{87}Sr/^{86}Sr)_i$ vs MgO (wt %). The symbols are as in Fig. 3a. (a) Magmatic rocks in the North Qiangtang terrane. (b) Magmatic rocks in the Songpan–Ganzi and North Kunlun terranes.

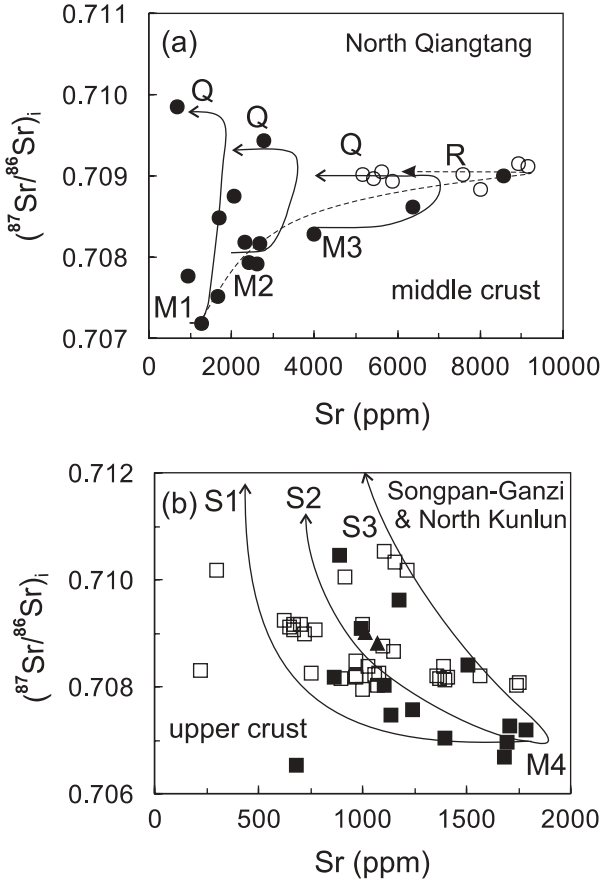

Fig. 11. $(^{87}Sr/^{86}Sr)_i$ vs Sr (ppm). (a) Magmatic rocks in the North Qiangtang terrane. The symbols are as in Fig. 3a. The curves labelled M1–Q, M2–Q and M3–Q are EC-AFC model curves for different compositions of the least differentiated basalts, as shown in Table 8. Arrows illustrate direction of falling T_m. The curve labelled R denotes the best-fit EC-AFC model curve for basalt M1, which has assimilated crustal rocks with Sr concentration of 6000 ppm and a $^{87}Sr/^{86}Sr$ ratio of 0·7094. (b) Magmatic rocks in the Songpan–Ganzi and North Kunlun terranes. The symbols are as in Fig. 3a. The curves with numbers S1, S2 and S3 represent EC-AFC model curves for assimilants with different compositions, as indicated in Table 7. Arrows illustrate the direction of falling T_m. M4 is the composition of the most primitive magma.

(T_{eq}) is 1100°C (Table 8). The majority of the data can be explained by an EC-AFC model in which three primitive magmas (M1–M3), with Sr contents of 1000 ppm, 2000 ppm and 4000 ppm, respectively, and corresponding initial Sr isotope ratios of 0·70720, 0·70805 and 0·70835, assimilate granulite-facies crust assimilant Q. This is consistent with the observation that the most primitive magmas in the North Qiangtang terrane (MgO >8 wt %) are isotopically heterogeneous (Fig. 10a). An important result of our iterative calculations is that the residue/melt bulk distribution coefficient for Sr for the partial melt of the assimilant is <1·0 (0·05), indicating that Sr is incompatible and the residue is feldspar-free. Likewise, the phenocryst/melt bulk distribution coefficients for Sr in the primitive magmas are significantly less than 1·0 (0·00001–0·06). This indicates that there are no fractionating phases in which Sr is compatible.

For the Songpan–Ganzi and North Kunlun terranes, the best fit EC-AFC results indicate that the assimilant liquidus temperature, solidus temperature and initial temperature are 1000°C, 800°C and 300°C, respectively. The magma liquidus temperature is 1280°C and the equilibration temperature (T_{eq}) is 980°C (Table 8). The calculations show that composition of the primitive magma is relatively homogeneous (Sr = 1800 ppm; $^{87}Sr/^{86}Sr$ = 0·7070), which is consistent with the observation from Fig. 10b. Conversely, the results of the iteration show that a range of crustal assimilants (S1–S3) are required, to fit the range of Sr isotopic compositions and Sr concentrations observed in the magmatic rocks. The calculated residue/melt bulk distribution coefficients for Sr for the partial melts of the assimilants are all

Table 7: Assumed parameters for the EC-AFC model calculations

Parameters	North Qiangtang		Songpan–Ganzi and North Kunlun	
Thermal parameters				
Isobaric specific heat of magma ($C_{p,m}$, J/kg per K)	1484		1484	
Isobaric specific heat of assimilant ($C_{p,a}$, J/kg per K)	1370		1370	
Crystallization enthalpy (Δh_{cry}, J/kg)	396000		396000	
Fusion enthalpy (Δh_{fus}, J/kg)	270000		270000	
Compositional parameters	Q	S1	S2	S3
Assimilant Sr content (C_a°, ppm)	200[1,2]	250[3]	250[2]	350[2]
Assimilant Sr isotope ratio (ε_a)	0·725[2,3]	0·720[3]	0·725[2]	0·730[2]

The thermal parameters are taken from Bohrson & Spera (2001). The compositional parameters of assimilants are taken from (1) Deng *et al.* (2002), (2) Pan (2000) and (3) Liu (1999). Q represents granulite as middle crustal assimilant in the North Qiangtang terrane. S1 (pelite), S2 (pelite) and S3 (calc-pelite) represent three different upper crustal assimilants with different compositions in the Songpan–Ganzi and North Kunlun terranes.

>1·0 (1·0–1·5), whereas the bulk distribution coefficients for Sr in the primitive magma are in the range 0·9–1·5 (Table 8). This requires the presence of feldspar in the residue and also indicates feldspar fractionation.

Interpretation of the parameters of the EC-AFC model

The best-fit calculation results of the EC-AFC model confirm that the correlated trends of $(^{87}Sr/^{86}Sr)_i$ vs Sr (ppm) for the K-rich magmas are caused by different processes in the North Qiangtang terrane (Fig. 11a) from those in the Songpan–Ganzi and North Kunlun terranes (Fig. 11b). Moreover, the calculated thermal and compositional parameters are also different between the two terranes (Table 8). This suggests differences in the depths of crustal contamination, the nature of the assimilant and the composition of the primitive magmas. In detail, the calculated assimilant liquidus temperature, solidus temperature and initial temperature in the North Qiangtang terrane during the EC-AFC process are higher compared with those in the Songpan–Ganzi and North Kunlun terranes (Table 8). This implies that the site at which EC-AFC processes occurred in the North Qiangtang terrane was deeper in the crust than in the Songpan–Ganzi and North Kunlun terranes. The inference that the residue of partial melting of the assimilant in the North Qiangtang terrane was feldspar-free may be interpreted to indicate a depth of assimilation beyond the field of feldspar stability. Conversely, the presence of feldspar in the residue of partial melting of the assimilant in the Songpan–Ganzi and North Kunlun terranes is consistent with a shallower depth of contamination in the crust. Moreover, the calculated results of the EC-AFC model show that the best-fit assimilant is a mafic granulite (Q) in the North Qiangtang terrane and a pelite (S1, S2) or calc-pelite (S3) in the Songpan–Ganzi and North Kunlun terranes.

Hacker *et al.* (2000) proposed that thermal gradient was 17°C/km in the Qiangtang terrane based on temperature estimates for crustal xenoliths entrained in 3 Ma shoshonitic rocks. According to this, the depth at which AFC processes occurred in the North Qiangtang terrane and Songpan–Ganzi and North Kunlun terranes was ~35 km and ~18 km, respectively, based on the calculation results for the assimilant initial temperature (Table 8). Owens & Zandt (1997) suggested that the crustal thickness of the North Qiangtang and Songpan–Ganzi terrane is 65 km and 55 km, respectively. This indicates that EC-AFC processes occurred in the middle crust (about 35 km) in the North Qiangtang terrane, but in the upper crust (about 18 km) in the Songpan–Ganzi and North Kunlun terranes, using the terms middle and upper crust to indicate relative depth.

Sr is compatible during the differentiation of the magmas in the Songpan–Ganzi and North Kunlun terranes (D_m = 0·9, 1·0, 1·5; Table 8), but is incompatible in those of the North Qiangtang terrane (D_m = 0·06, 0·006 and 0·00001; Table 8). This is consistent with the presence of plagioclase phenocrysts in most of the samples from the Songpan–Ganzi and North Kunlun terranes, and their absence in those from the North Qiangtang terrane (Table 2).

For the three basement terranes, it is not possible to fit the correlated trends of $(^{87}Sr/^{86}Sr)_i$ vs Sr (ppm) (Fig. 11) for the potassium-rich magmatic rocks with a single composition of assimilant and primitive magma. This suggests that the crustal assimilants and/or parent magmas are heterogeneous in terms of their trace element and Sr isotopic compositions in the three terranes. For the samples from the North Qiangtang terrane, our attempts to simulate EC-AFC processes using a parent magma with low Sr content (M1) required an unrealistically high concentration of Sr in the assimilant (~6000 ppm), and the $^{87}Sr/^{86}Sr$ ratios of the most evolved magmas simulated by the EC-AFC model were lower (~0·709; Fig. 11a) than those of the most extreme samples analysed (~0·710). Irrespective of changes in the initial parameters of the parent magma, the $^{87}Sr/^{86}Sr$ ratios of the more evolved magmas calculated by the EC-AFC model were always lower than ~0·710 and the model curve (dashed curve line labelled R in Fig. 11a) could not be forced to fit the trend of the analysed data. This requires that the least differentiated parent magmas were compositionally

Table 8: Best-fit calculation results of parameters of the EC-AFC model

Modelling processes	North Qiangtang			Songpan–Ganzi and North Kunlun		
	M1/Q	M2/Q	M3/Q	M4/S1	M4/S2	M4/S3
Thermal parameters						
Magma liquidus temperature ($T_{l,m}$,°C)		1300			1280	
Magma initial temperature ($T_m°$,°C)		1300			1280	
Assimilant liquidus temperature ($T_{l,a}$,°C)		1150			1000	
Assimilant initial temperature ($T_a°$,°C)		600			300	
Solidus temperature (T_s,°C)		900			800	
Equilibration temperature (T_{eq},°C)		1100			980	
Compositional parameters						
Magma initial Sr content ($C_m°$, ppm)	1000	2000	4000	1800	1800	1800
Magma Sr isotope ratio (ε_m)	0·70720	0·70805	0·70835	0·7070	0·7070	0·7070
Magma bulk distribution coefficient for Sr (D_m)	0·06	0·006	0·00001	1·5	1·0	0·9
Assimilant bulk distribution coefficient for Sr (D_a)	0·05	0·05	0·05	1·5	1·5	1·0

M1, M2, M3 and M4 are primitive magma compositions; Q, S1, S2 and S3 are assimilants.

heterogeneous in the North Qiangtang terrane. For the Songpan–Ganzi and North Kunlun terranes, simulation of EC-AFC processes using a single initial composition for the parent magma, combined with variable compositions for the assimilant (Table 7), could fit the correlated trends of $(^{87}Sr/^{86}Sr)_i$ vs Sr (ppm) in Fig. 11b, indicating that the assimilants were compositionally and isotopically heterogeneous.

Previous studies (Owens & Zandt, 1997; Unsworth *et al.*, 2004) have proposed that there is pervasive partial melting of the crust beneath the northern Tibetan Plateau based on the high Poisson's ratio of the crust of the North Qiangtang and Songpan–Ganzi terranes. Such pervasive partial melting zones are probably the sites at which EC-AFC processes have taken place. The average thickness of the crust is greater beneath the North Qiangtang terrane (65 km) than beneath the Songpan–Ganzi terrane (55 km) (Owens & Zandt, 1997). This is consistent with the results of our EC-AFC modelling, which indicate that crustal contamination of the rising magmas happened in the middle crust in the North Qiangtang terrane, but in the upper crust in the Songpan–Ganzi and North Kunlun terranes (Fig. 12). The migration with time from the middle crust to the upper crust is probably related to thermal maturation of the crust. The eruption of some primitive magmatic rocks indicates that not all the magmas were affected by EC-AFC processes (Fig. 12).

The evolved magmatic rocks in the three terranes (North Qiangtang, Songpan–Ganzi and North Kunlun) of north Tibet have broadly similar ranges of Sr–Nd–Pb isotope compositions (Fig. 9). However, the compositions of the most primitive magmas in the different terranes are variable based on their trace element and Sr–Nd–Pb isotope compositions. We consider that the convergence in the geochemical characteristics of the evolved magmas in north Tibet is caused by the operation of EC-AFC processes. Our model results indicate that the composition of the crustal assimilant and/or the primitive mantle-derived magmas was variable in the three terranes (Tables 7 and 8). For example, the primitive magmas in the North Qiangtang terrane have higher contents of LILE (Table 3 and Electronic Appendix), higher $(^{87}Sr/^{86}Sr)_i$ and $(^{206}Pb/^{204}Pb)_i$ ratios and lower $(^{143}Nd/^{144}Nd)_i$ ratios (Fig. 8) than those in the Songpan–Ganzi and North Kunlun terranes. The primitive magmas in the North Qiangtang terrane underwent contamination by middle crustal rock types (Fig. 11a), which have relatively low $^{206}Pb/^{204}Pb$ ratios and LILE contents (Table 7) compared with likely upper crustal contaminants (Liu, 1999; Pan, 2000; Deng *et al.*, 2002). The EC-AFC process decreased the $^{206}Pb/^{204}Pb$ ratios and LILE contents of the resultant evolved magmas compared with the primitive magmas in the North Qiangtang terrane. In contrast, the primitive magmatic rocks in the Songpan–Ganzi and North Kunlun terranes have lower LILE contents (Table 3 and Electronic Appendix), lower $(^{87}Sr/^{86}Sr)_i$ and $(^{206}Pb/^{204}Pb)_i$ ratios, and higher $(^{143}Nd/^{144}Nd)_i$ ratios than those in the North Qiangtang terrane (Fig. 8). The primitive magmas in the Songpan–Ganzi and North Kunlun terranes appear to

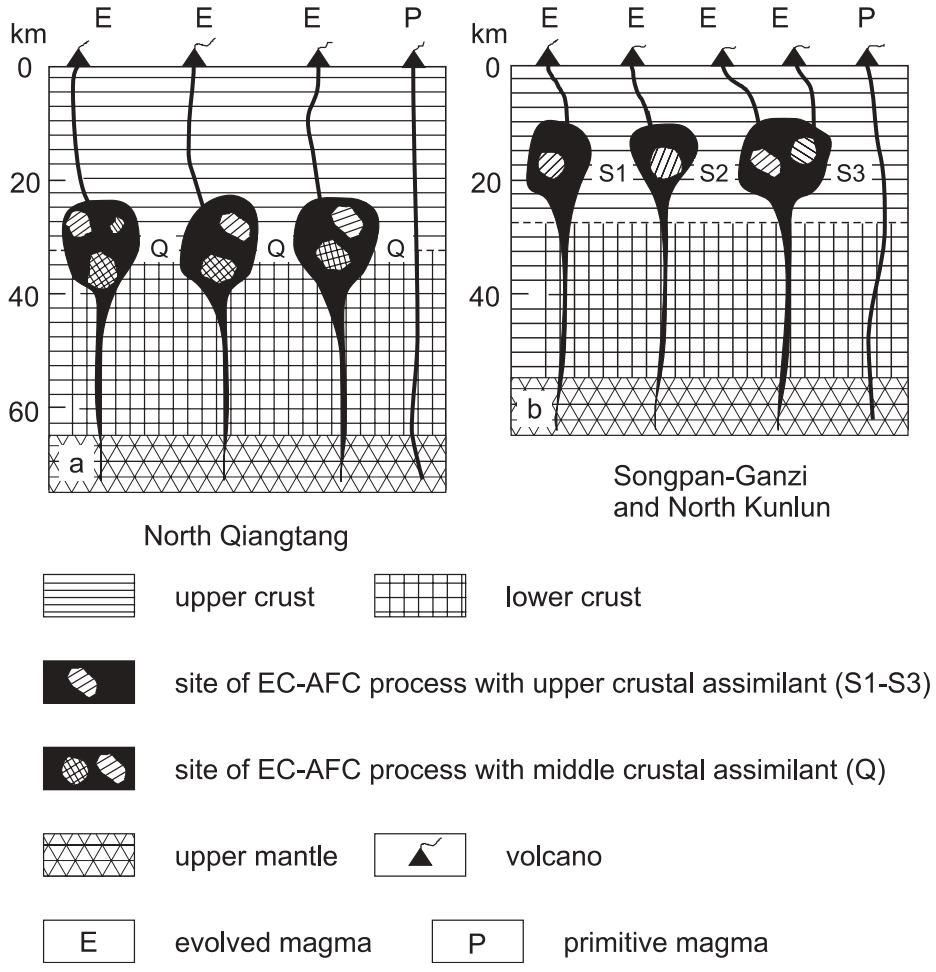

Fig. 12. Comparison of EC-AFC processes between the North Qiangtang terrane and the Songpan–Ganzi and North Kunlun terranes. (a) EC-AFC processes in the North Qiangtang terrane. (b) EC-AFC processes in the Songpan–Ganzi and North Kunlun terranes. The meaning of Q, S1, S2 and S3 is as in Fig. 11 and Table 7. Thickness of the crust is from Owens & Zandt (1997). The inference of magmatic underplating in north Tibet is based on available geophysical data (Owens & Zandt, 1997).

have undergone contamination by upper crustal rocks (Fig. 11b), which have relatively high $^{206}Pb/^{204}Pb$ ratios and LILE contents (Table 7) compared with the middle crustal rocks (Liu, 1999; Pan, 2000; Deng *et al.*, 2002). The EC-AFC process increased the $^{206}Pb/^{204}Pb$ and LILE contents in the resultant evolved magmas, compared with the primitive magmas, in the Songpan–Ganzi and North Kunlun terranes. Thus, the EC-AFC processes resulted in similar $^{206}Pb/^{204}Pb$ and LILE contents in the evolved magmas of the three terranes in north Tibet. The similarities in $^{87}Sr/^{86}Sr$ and $^{143}Nd/^{144}Nd$ ratios in the evolved magmas of the three terranes are because of the higher concentrations of Sr and Nd in the partial melts of the assimilants compared with those of the least differentiated basaltic magmas during EC-AFC processes. This leads to the $^{87}Sr/^{86}Sr$ and $^{143}Nd/^{144}Nd$ ratios of the resultant evolved magmas in the three terranes being close to those of the assimilants (e.g. increasing $^{87}Sr/^{86}Sr$). Similarities in the $^{87}Sr/^{86}Sr$ and $^{143}Nd/^{144}Nd$ ratios of the partial melts of the assimilants in the different terranes (Table 7) may result in convergence in the $^{87}Sr/^{86}Sr$ and $^{143}Nd/^{144}Nd$ ratios of the resultant evolved magmas in different basement terranes. Consequently, EC-AFC processes appear to have reduced the systematic differences in the trace element and isotope compositions of the evolved magmas, compared with those in the primitive magmas, between the North Qiangtang terrane and the Songpan–Ganzi and North Kunlun terranes.

The compositions of the evolved magmas in north Tibet have clearly undergone significant modification by crustal contamination during EC-AFC processes. The trace element and Sr–Nd–Pb isotope compositions of the evolved magmas are different from those of the primitive magmas. Only the primitive magmas can be used to investigate the characteristics of the mantle source

region and its evolution. Thus, conclusions about the nature of the mantle source reached by previous workers (e.g. Turner *et al.*, 1993, 1996*a*; Williams *et al.*, 2004), which were dominantly based on studies of the evolved magmas, need to be re-evaluated.

Nature of the mantle source region of the parental magmas

Enrichment of the mantle source

Oceanic basalts [i.e. ocean island basalts (OIB) and mid-ocean ridge basalts (MORB)] typically display positive Nb–Ta–Ti anomalies and negative Pb anomalies in primitive mantle-normalized trace element diagrams (e.g. Hofmann, 1986, 1988, 1997). In contrast, all of the primitive potassic and ultrapotassic magmatic rocks in north Tibet exhibit strongly negative Nb–Ta–Ti anomalies and positive Pb anomalies (Fig. 6), indicating that they were not derived from normal MORB- or OIB-source mantle. The significant difference between the primitive potassium-rich igneous rocks in north Tibet and MORB and OIB sources in the Sr–Nd isotope correlation diagram (Fig. 8a) supports this inference. Moreover, the average Ce/Pb ratios (7·64) of the primitive samples are considerably different from those of oceanic basalts (OIB and MORB) (~25; Hofmann, 1988, 1997), suggesting that they are not derived from normal asthenospheric mantle. The presence of residual phlogopite in the mantle source region of the northern Tibetan magmas could not cause the significant reduction in their Ce/Pb ratios relative to those of MORB and OIB because the partition coefficients for Ce and Pb in phlogopite are 0·0007 and 0·019 (Williams *et al.*, 2004), respectively, both of which are far less than unity. Consequently, residual phlogopite in the mantle source should increase the Ce/Pb ratio in the magmas rather than decrease it. In addition, there are differences in the average Ce/Pb ratios of the primitive magmas from each of the three terranes; these are 6·22, 8·83 and 8·43 in the North Qiangtang, Songpan–Ganzi and North Kunlun terranes, respectively, based on the data in Table 3 and the Electronic Appendix. The differences in the Ce/Pb ratios of the primitive magmas in the Songpan–Ganzi and North Kunlun terrane are relatively small. Nevertheless, it seems clear that the mantle source of the primitive magmas must differ in composition between the North Qiangtang terrane and the Songpan–Ganzi and North Kunlun terranes in terms of its trace element composition.

The significantly high abundances of incompatible trace elements (e.g. Rb, Ba, Th, U, Pb and Sr; Figs 4 and 6), and high light REE (LREE)/HREE (Fig. 7a), require enrichment of the mantle source region of the magmas before the onset of partial melting. The generation of such extreme trace element enrichment in the North Qiangtang parental magmas (e.g. Ba >6000 ppm; Fig. 4f and g) by partial melting of normal asthenospheric mantle (i.e. MORB-source mantle) would require vanishingly small degrees of partial melting. For example, if the concentration of Ba in the melt was 7627 ppm (e.g. sample G98-14; Table 3), the degree of partial melting would be ~0·0023%, assuming a bulk partition coefficient $D = 6 \times 10^{-5}$ (http://www.earthref.org/) and $C_0 = 0{\cdot}63$ ppm [normal MORB (N-MORB) mantle source; Sun & McDonough, 1989], based on a modal batch partial melting model (Wilson, 1989). The enrichment of the mantle source is also shown by increases in Th/U, U/Pb, and Rb/Sr and a decrease in Sm/Nd relative to depleted mantle values. Additionally, the high $^{87}Sr/^{86}Sr$ ratios and relatively low $^{143}Nd/^{144}Nd$ isotopic ratios (Table 5 and Fig. 8) of the primitive samples from north Tibet reflect a mantle source region with a time-integrated history of enrichment in Rb and LREE.

On the basis of the combined trace element and Sr–Nd–Pb isotope data, we conclude that the parental magmas of the potassic and ultrapotassic magmatic rocks in north Tibet were derived from an enriched mantle source rather than the normal asthenospheric (i.e. N-MORB-source) mantle.

Two end-member components of the mantle source

Experimental data (Brenan *et al.*, 1995; Keppler, 1996) and geochemical studies (Gill, 1981; Pearce, 1982; Pearce & Parkinson, 1993; Pearce & Peate, 1994; Hawkesworth *et al.*, 1993, 1997*a*; Turner, 2002; Turner *et al.*, 2003) indicate that island arc and active continental margin mafic magmas, petrogenetically related to subduction of oceanic lithosphere, are characterized by significant enrichment in LILE relative to HFSE, with strongly negative Nb–Ta–Ti anomalies and positive Pb anomalies in primitive mantle-normalized incompatible trace element diagrams. These characteristics are also shown by the primitive potassium-rich magmatic rocks from the northern part of the Tibetan Plateau (Fig. 6). Additionally, the Sr–Nd–Pb isotopic compositions of the primitive magmatic rocks in north Tibet plot within the range of isotopic compositions of Global Subducting Sediment (GLOSS; Plank & Langmuir, 1998) (Fig. 8), consistent with a subduction-related origin for the mantle source enrichment.

Previous geological studies have shown that the basement terranes (North Kunlun, South Kunlun, Songpan–Ganzi and North Qiangtang; Fig. 1) in north Tibet experienced multiple episodes of subduction of Proto- and Palaeo-Tethys oceanic lithosphere from Proterozoic to Middle–Late Triassic times, upon which were superimposed the effects of subduction of the back-arc basin lithosphere of the South Kunlun ocean and Jinsha ocean,

respectively (Pan *et al.*, 1998; Mattern & Schneider, 2000; Pan, 2000; Wang *et al.*, 2000; Xiao *et al.*, 2002). Migration of subduction-related melts and/or fluids would undoubtedly have contributed to the localized enrichment of the mantle lithosphere beneath north Tibet, generating low melting-point domains that would be easily melted during subsequent phases of lithospheric thinning and reheating, resulting in the generation of potassium-rich magmas with geochemical signatures similar to those of magmas derived from the mantle wedge above subduction zones.

Zhou & Murphy (2005) have provided evidence based on seismic tomography studies for wholesale underthrusting of Indian continental lithospheric mantle beneath the entire Tibetan Plateau and the presence of a thin asthenospheric mantle wedge above the subducted slab of Indian lithosphere. These data provide an alternative model for the petrogenesis of the most primitive magmas by partial melting of this asthenospheric wedge, which has been enriched by melts and/or fluids derived from Indian passive margin sediments subducted into the shallow mantle as a consequence of northward underthrusting of the Indian continental lithosphere. Partial melting of this enriched asthenospheric mantle wedge could produce magmas geochemically similar to subduction-related magmatic rocks. Logically, both the asthenospheric wedge and the base of the Asian continental lithosphere could be potential mantle sources for generation of the primitive magmas in north Tibet.

Previous studies have shown that supra-subduction zone enrichment of the mantle wedge can be broadly attributed to migration of: (1) aqueous fluids derived from dehydration of either altered oceanic crust (Tatsumi *et al.*, 1986; Hawkesworth *et al.*, 1993, 1997*a*; Turner *et al.*, 1996*b*, 1997; Turner, 2002) or subducted sediments (Ryan *et al.*, 1995; Class *et al.*, 2000; Elburg *et al.*, 2002); (2) partial or bulk melts of subducted sediments or even the subducted crust itself (Hawkesworth *et al.*, 1993, 1997*a*; Vroon *et al.*, 1993; Elliott *et al.*, 1997; Elburg *et al.*, 2002).

Important geochemical distinctions have been recognized between subduction-related magmatic rocks in which the magma sources are modified by a subduction-related aqueous fluid and those that are enriched by bulk subducted sediment or a partial or a bulk melt thereof (e.g. Hawkesworth *et al.*, 1997*a*, 1997*b*; Elburg *et al.*, 2002). The fluid, which carries very little REE and HFSE (e.g. Ce, Th, Nb, Zr and Ta), introduces significant amounts of LILE (e.g. Rb, Ba, Sr) and other fluid-mobile trace elements (e.g. U, Pb) into the mantle wedge. However, subducted sediment (or partial or bulk melt) is characterized by relatively high Th and LREE contents. Thus, those subduction-related magmatic rocks whose source was strongly metasomatized by a fluid component are likely to have higher U/Th (Hawkesworth *et al.*, 1997*a*), Ba/Th (Hawkesworth *et al.*, 1997*a*; Turner *et al.*, 1997) and Sr/Th (Hawkesworth *et al.*, 1997*a*) ratios than rocks whose source was enriched by bulk sediment or a partial or bulk melt of subducted sediment (Hawkesworth *et al.*, 1997*a*; Elburg *et al.*, 2002). In contrast, those subduction-related magmas with a strong imprint of a partial melt or bulk melt of subducted sediment or subducted sediment itself in their source region have higher Th/Ce (Hawkesworth *et al.*, 1997*a*, 1997*b*; Elburg *et al.*, 2002), $^{87}Sr/^{86}Sr$ and $^{206}Pb/^{204}Pb$ ratios (Hawkesworth *et al.*, 1997*b*; Turner *et al.*, 1997), higher Th contents, and lower $^{143}Nd/^{144}Nd$ ratios (Hawkesworth *et al.*, 1997*a*, 1997*b*) than those related to fluid metasomatism of their mantle source. Both fluid- and melt- (or subducted bulk sediment) induced metasomatism could account for the negative Nb–Ta–Ti anomalies of the north Tibet potassium-rich rocks (Fig. 6).

The combination of incompatible trace element and isotope ratios has been effectively used as a fingerprint in identifying the origin of metasomatic components in the source of subduction-related magmas (Hawkesworth *et al.*, 1997*a*, 1997*b*; Turner *et al.*, 1997). Previous studies have shown that fluids generated by dehydration of hydrothermally altered subducted oceanic crust have low $^{87}Sr/^{86}Sr$ ($\sim$0·7035), but high Ba/Th ($> \sim$170) ratios (Turner *et al.*, 1996*b*, 1997; Hawkesworth *et al.*, 1997*a*, 1997*b*; Elburg *et al.*, 2002; Guo *et al.*, 2005). The north Tibet primitive samples have higher $(^{87}Sr/^{86}Sr)_i$ ratios (>0·706) and lower Ba/Th ratios than fluids derived from altered subducted oceanic crust, and lower Ba/Th ratios than fluids derived from subducted sediments (Fig. 13). The $(^{87}Sr/^{86}Sr)_i$ ratios of the primitive magmas in north Tibet fall almost exclusively within the range of GLOSS (Plank & Langmuir, 1998; Fig. 13), which may suggest that their mantle source region was modified by mixing in bulk subducted sediment or metasomatized by a partial melt or a bulk melt of subducted sediment prior to the generation of the Cenozoic potassium-rich magmas.

It is thought unlikely that bulk subducted sediment can be added to the mantle source of subduction-related magmas (Hawkesworth *et al.*, 1997*a*; Turner *et al.*, 1997; Elburg *et al.*, 2002). The north Tibet primitive samples display a broad, linear, positive correlation between Th/Ce and Th/Sm (Fig. 14a), which could suggest simple two-component mixing. One end-member has a composition similar to Indian MORB-source mantle (Rehkämper & Hofmann, 1997) with low Th/Ce and Th/Sm. The average composition of GLOSS (Plank & Langmuir, 1998), however, lies within the linear trend; most samples plot beyond the range of Indian MORB-source mantle and the GLOSS average (Plank & Langmuir, 1998). This argues against average GLOSS as the second end-member for the two-component

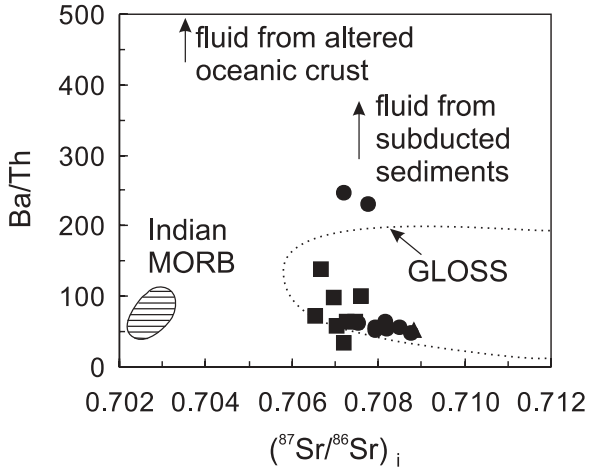

Fig. 13. Ba/Th vs $(^{87}Sr/^{86}Sr)_i$. To minimize the effect of magmatic differentiation and crustal contamination, only primitive samples with MgO >6 wt % are plotted. Overlapping of $(^{87}Sr/^{86}Sr)_i$ ratios between GLOSS (Plank & Langmuir,1998) and the potassium-rich magmatic rocks in north Tibet suggests the involvement of a subducted sediment-derived component in the generation of the magmas (see main text for further interpretation). The composition of the fluid derived from subducted altered oceanic crust is from Turner *et al.* (1997). Data for Indian MORB are taken from Rehkämper & Hofmann (1997). The symbols are as in Fig. 3a.

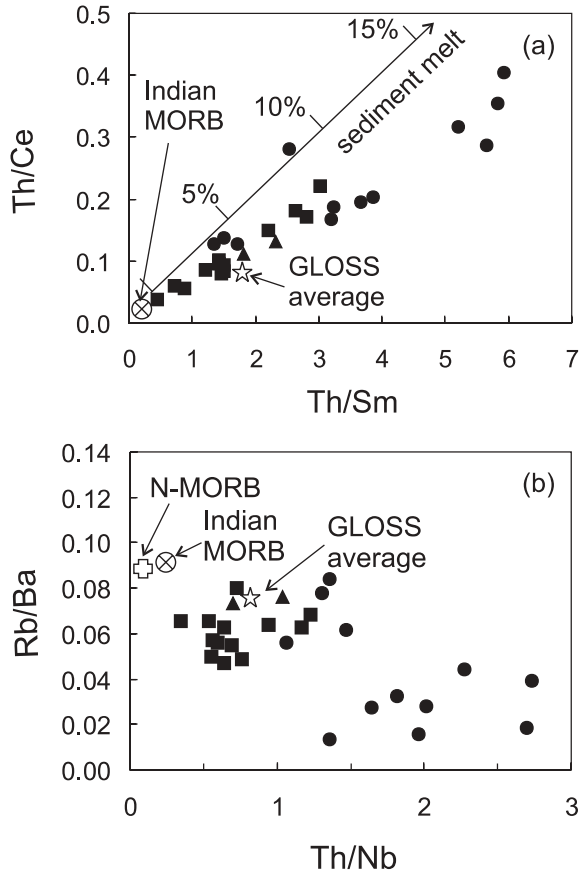

Fig. 14. (a) Th/Ce vs Th/Sm. (b) Rb/Ba vs Th/Nb. To minimize the effect of magmatic differentiation and crustal contamination, only primitive samples with MgO >6 wt % are plotted. The arrow labelled 'sediment melt' in (a) indicates a simple two-component mixing curve between a partial (4%) melt of the GLOSS average and Indian MORB-source mantle. The numbers in per cent shown on the tick marks of the curve in (a) denote the proportions of sediment melt in the primitive magmatic rocks. Data for Indian MORB and N-MORB are taken from Rehkämper & Hofmann (1997) and Sun & McDonough (1989), respectively. Data for GLOSS average are from Plank & Langmuir (1998). The symbols are as in Fig. 3a.

mixing. The sediment-derived end-member has to have much higher Th/Ce and Th/Sm ratios than the GLOSS average. Th/Ce and Th/Sm fractionation is likely during partial melting of subducted sediment, leading to higher Th/Ce and Th/Sm ratios in the partial melt than in the subducted bulk sediment (i.e. GLOSS) or a bulk melt of the subducted sediment. This indicates that the second end-member for the two-component mixing in Fig. 14a is probably a partial melt of subducted sediment. Simple two-component (i.e. partial melt of the sediment and Indian MORB-source mantle) mixing calculations support this inference; the model curve broadly approximates the analysed data trend (Fig. 14a). The departure of the model curve from the trend of the actual data may be interpreted as reflecting differences in the fractionation of Th/Ce and Th/Sm during partial melting of the subducted sediment. The model curve suggests that the degree of partial melting of average GLOSS is 4%, and that the proportion of the partial melt of average GLOSS in the primitive magmatic rocks of the North Qiangtang terrane (4–15%) is higher than that in the Songpan–Ganzi and North Kunlun terranes (<8%). The linear arrays in Sr–Nd–Pb isotope space defined by the primitive samples (Fig. 8a, d and e) also support such a two-component mixing model.

If a partial melt of subducted sediment was added to the mantle source, the Ba/Th ratios of the primitive magmas should be slightly higher than those of bulk subducted sediment (i.e. GLOSS), because of Ba/Th fractionation during partial melting of the sediment. However, it is possible that phlogopite in the mantle source region may have retained Ba to variable degrees, resulting in relatively low and variable Ba/Th ratios in the primitive magmas in north Tibet (Fig. 13).

The combined constraints of incompatible trace element and Sr–Nd–Pb isotope ratios show that the mantle source region of the primitive magmas in north Tibet resulted from metasomatism of Indian MORB-source mantle by a partial melt of subducted sediment.

Heterogeneity of the mantle source beneath the different terranes

The differences in the proportion of partial melt of subducted sediment (GLOSS) in the primitive magmas of the North Qiangtang terrane and the Songpan–Ganzi and

North Kunlun terranes (Fig. 14a), indicated by the two-component mixing model calculations, suggest regional compositional differences in the mantle source regions. Moreover, the primitive magmatic rocks from the North Qiangtang terrane have higher $(^{87}Sr/^{86}Sr)_i$ and $(^{206}Pb/^{204}Pb)_i$, and lower $(^{143}Nd/^{144}Nd)_i$ ratios compared with those from the Songpan–Ganzi and North Kunlun terranes (Fig. 8). This is consistent with an increased amount of subducted sediment-derived melt added to the mantle source beneath the North Qiangtang terrane relative to the North Kunlun and Songpan–Ganzi terranes.

The slopes of the positive correlations between La/Yb and La (Fig. 7a), and Ce/Pb and Ce (Fig. 7b) are markedly different in the primitive magmatic rocks from the North Qiangtang terrane compared with those from the Songpan–Ganzi and North Kunlun terranes. This indicates that the primitive magmas in the different terranes of north Tibet were derived by variable degrees of partial melting of different mantle sources. The results of non-modal batch melting modelling (Fig. 7a) indicate that the mantle source region of the primitive magmas beneath the North Qiangtang terranes contains ~5% sediment melt, whereas that beneath the Songpan–Ganzi terrane contains ~1% sediment melt; degrees of partial melting of the mantle source range from 0·1% to 15%. This supports the inference that the composition of the mantle source region beneath the North Qiangtang terrane was different from that beneath the North Kunlun and Songpan–Ganzi terranes.

Residual minerals in the mantle source region of the parental magmas

The positive correlations between La/Yb and La (Fig. 7a), and Ce/Pb and Ce (Fig. 7b) show that partial melting is the dominant control factor on the compositional variations of the most primitive potassium-rich magmatic rocks in the northern part of the Tibetan Plateau. The following residual minerals in the mantle source region might retain their compatible elements during partial melting.

Spinel

The relatively high middle REE (MREE) and HREE abundances (Table 3 and Electronic Appendix) of the primitive samples (e.g. Yb contents that are >10 times chondritic abundances; Fig. 5) preclude garnet as a residual mineral in the mantle source region. The relatively flat HREE distribution patterns in chondrite-normalized diagrams (Fig. 5a–c), showing that HREE fractionations are weak, also do not support the presence of garnet in the mantle source region. Instead, the patterns are consistent with the presence of spinel in the mantle source.

Phlogopite

It has been shown that fractionation of incompatible elements during partial melting will happen if mineral phases that retain them are residual in the source region at low degrees of melting (e.g. Wilson, 1989). Because the mantle source region of the primitive magmas in north Tibet is inferred to be a mixture of Indian MORB-source mantle and a partial melt of subducted sediment, the Rb/Ba ratios of the primitive magmas should lie between those of Indian MORB-source mantle and partial melts of subducted sediment, if no residual minerals retained Rb and Ba, because both Ba and Rb are strongly incompatible during mantle partial melting. However, most of the primitive samples studied here have lower Rb/Ba ratios than both Indian MORB-source mantle and the GLOSS average (Fig. 14b). This requires that a mineral phase has preferentially retained Rb relative to Ba, which, therefore, must have a higher partition coefficient for Rb than Ba. The depletion of Rb relative to Ba in the primitive mantle-normalized incompatible element patterns of the primitive magmatic rocks also supports this inference (Fig. 6). These characteristics are consistent with the presence of phlogopite, which has a higher partition coefficient for Rb than Ba, rather than amphibole, because amphibole has a higher partition coefficient for Ba than Rb (Green, 1994; Foley *et al.*, 1996).

No correlation exists between $(Rb/Ba)_{PM}$ and MgO (wt %) in the studied samples (not shown), suggesting that there is no fractionation of phlogopite during magmatic differentiation (PM in the subscript represents the primitive mantle-normalized value). There is, however, a strong negative correlation between $(Rb/Ba)_{PM}$ and La/Yb in the primitive magmatic rocks, which indicates a decrease in the extent to which Rb is retained by residual phlogopite in the mantle source region with increasing degrees of partial melting (Fig. 15a and b); that is, phlogopite preferentially enters the melt during partial melting. The primitive magmas in the Songpan–Ganzi terrane have very uniform K contents (Fig. 6b), indicating that concentrations of this element are strongly buffered by residual phlogopite in the mantle source. However, the primitive magmas in the North Qiangtang terrane have variable K contents (Fig. 6a). This suggests that K is not as strongly buffered by phlogopite in the mantle source as in the Songpan–Ganzi terrane, or that the mantle source is heterogeneous (Fig. 10a), or both.

Two Ti-bearing mineral phases

Th/Nb ratios in the primitive magmas of north Tibet should lie between the Indian MORB-source mantle end-member and that of a partial melt of subducted sediment, based on the inference that the mantle source region of the magmas was a mixture of Indian

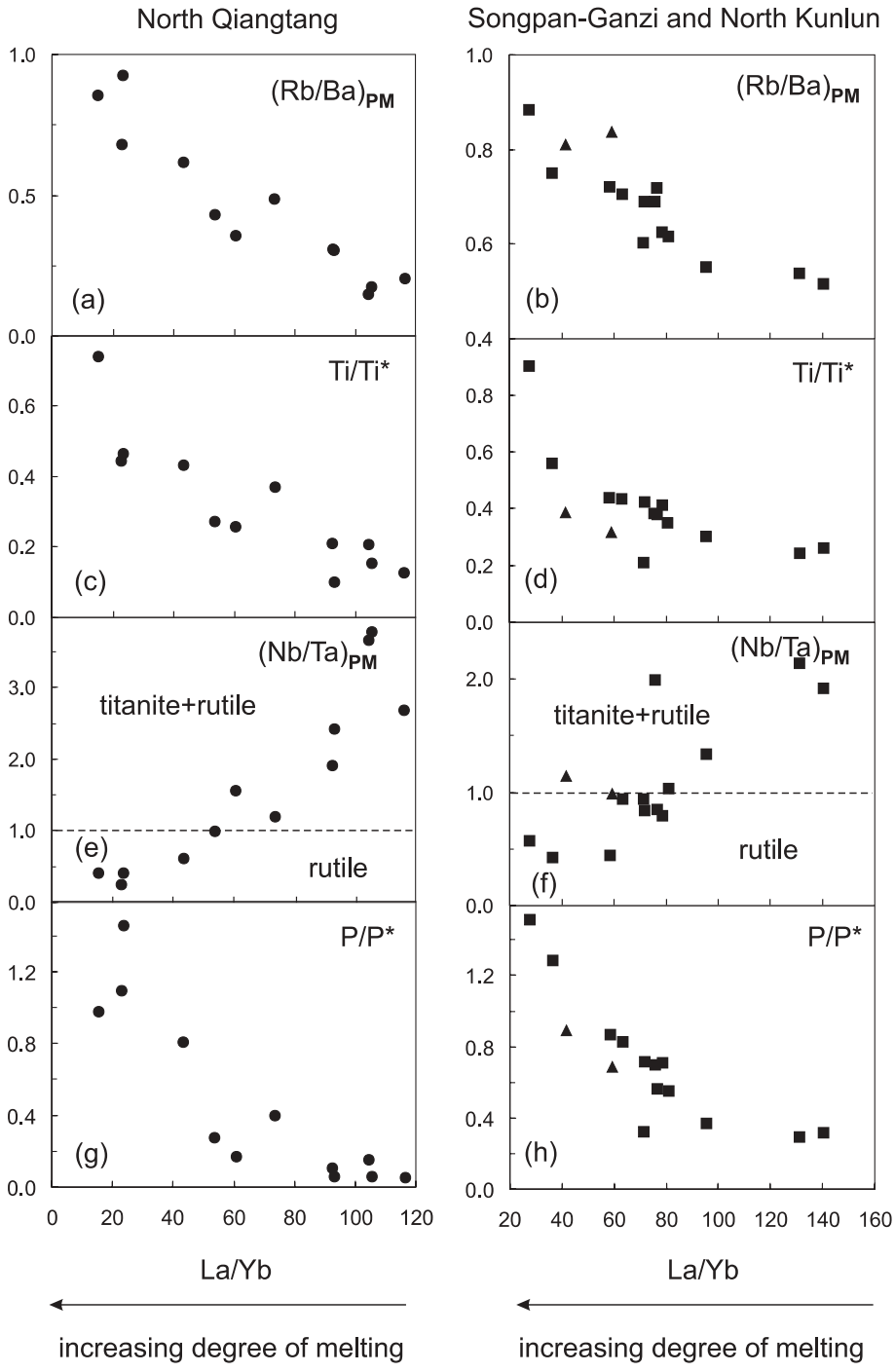

Fig. 15. (a, b) $(Rb/Ba)_{PM}$ vs La/Yb. (c, d) Ti/Ti* vs La/Yb. (e, f) $(Nb/Ta)_{PM}$ vs La/Yb. (g, h) P/P* vs La/Yb. In (a, c, e, g) the primitive magmatic rocks (MgO >6 wt %) in the North Qiangtang terrane are shown; in (b, d, f, h) the primitive magmatic rocks (MgO >6 wt %) in the Songpan–Ganzi and North Kunlun terranes are shown. The meaning of $(Rb/Ba)_{PM}$, Ti/Ti*, $(Nb/Ta)_{PM}$ and P/P* is described in the main text. Dashed lines in (e, f) indicate the primitive mantle normalized Nb/Ta ratio (i.e. 1·0). The symbols are as in Fig. 3a.

MORB-source mantle and a partial melt of subducted sediment (Fig. 14a), only if the primitive magmas inherit the Th/Nb of their mantle source. However, most of the primitive samples have higher Th/Nb ratios than both Indian MORB-source mantle and the GLOSS average (Plank & Langmuir, 1998; Fig. 14b). This indicates that the addition of subducted sediment melts to the mantle source cannot totally be responsible for the high Th/Nb

ratios; these are, instead, probably caused by residual Ti-bearing phases in the source region. These phases must have higher partition coefficients for Nb than Th, and preferentially retain Nb over Th. The positive correlation between Nb (ppm) and TiO_2 (wt %) in the primitive rocks (not shown), combined with strong negative anomalies in Nb, Ta and Ti in mantle-normalized trace element diagrams (Fig. 6), supports the presence of Ti-rich residual mineral phases in the mantle source region. In addition, the relatively flat correlation of TiO_2 vs MgO for the samples (Fig. 4e) also suggests that there might be residual Ti-bearing phases buffering the TiO_2 contents. No correlations exist between Ti/Ti*, Nb/Ta and MgO in the Tibetan magmatic rocks (not shown), indicating that there is no fractionation of Ti-bearing phases (Ti* is the expected concentration of Ti assuming no Ti anomaly in the mantle-normalized incompatible element diagram shown in Fig. 6). Based on the above, we conclude that the primitive mantle-normalized incompatible element patterns (Fig. 6) result from both additions of melt of subducted sediments to the mantle source, which produces enrichment in LILE (Fig. 14a), and the presence of Ti-rich residual mineral phases retaining HFSE, which causes depletions in these elements. Previous studies (e.g. Williams *et al.*, 2004) identified only one Ti-rich residual mineral phase (i.e. rutile). However, below we show that there were at least two residual Ti-rich mineral phases in the mantle source.

Both rutile and titanite have high partition coefficients for the HFSE Nb, Ta and Ti (Green, 1994; Foley *et al.*, 2000; Green *et al.*, 2000). These phases may retain the HFSE during progressive mantle partial melting, leading to strong depletion of these elements in the resultant magmas (Foley & Wheller, 1990; Sheppard & Taylor, 1992; Pearce & Parkinson; 1993; Pearce & Peate, 1994). Rutile has a higher partition coefficient for Nb (136) than Ta (16·6), whereas titanite has a higher partition coefficient for Ta (142) than Nb (4·6) (data from: http://www.earthref.org/). Some samples from north Tibet exhibit depletions in Nb that are stronger than those of Ta in the mantle-normalized trace element patterns (Fig. 6a and b); this suggests that rutile may be the dominant residual mineral phase in the mantle source. However, other samples show greater depletions of Ta than Nb (Fig. 6a and b), suggesting that titanite may be the dominant residual mineral phase in the mantle source. Other samples show broadly similar depletions of Ta and Nb (e.g. Fig. 6c), which might be well explained by approximately equal proportions of titanite and rutile in the mantle source region. This is further confirmed by the correlation between $(Nb/Ta)_{PM}$ and La/Yb (Fig. 15e and f), which shows a broadly decreasing trend in $(Nb/Ta)_{PM}$ ratios with decreasing La/Yb in the primitive magmas of the North Qiangtang and Songpan–Ganzi terranes. In detail, some of the primitive magmatic rocks have $(Nb/Ta)_{PM}$ ratios >1·0, suggesting that both titanite and rutile were present in the mantle source, and that titanite is more important than rutile in terms of retaining the HFSE; however, other primitive samples have $(Nb/Ta)_{PM}$ ratios <1·0, which suggests that in their petrogenesis titanite had progressively melted out and only rutile was residual in the mantle source, differentially retaining the HFSE because of differences in the partition coefficients for Nb and Ta in rutile and titanite. This suggests that the influence of residual rutile on the Nb and Ta contents of the primitive magmas becomes progressively stronger than that of titanite with increasing degree of partial melting. Thus, the negative correlation between $(Nb/Ta)_{PM}$ and La/Yb (Fig. 15e and f) suggests that the Ti-bearing residual mineral phases in the mantle source included both rutile and titanite, followed by rutile only with increasing degree of partial melting.

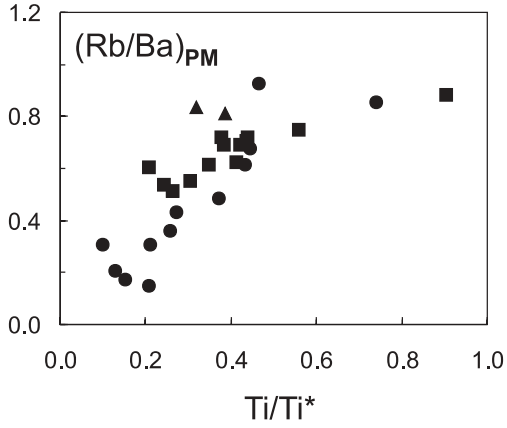

Fig. 16. $(Rb/Ba)_{PM}$ vs Ti/Ti*. To minimize the effect of magmatic differentiation and crustal contamination, only primitive samples with MgO >6 wt % are plotted. The meaning of $(Rb/Ba)_{PM}$ and Ti/Ti* is described in the main text. The symbols are as in Fig. 3a.

Ti/Ti* ratios show a progressive increase with increasing degree of partial melting (decreasing La/Yb) in the primitive magmas of the North Qiangtang and Songpan–Ganzi terranes (Fig. 15c and d). The broad positive correlation between $(Rb/Ba)_{PM}$ and Ti/Ti* (Fig. 16) suggests that residual phlogopite in the mantle source region may also influence the Ti budget in the primitive magmas.

Apatite

No correlation exists between P/P* (the meaning of P/P* is similar to that of Ti/Ti*) and indices of differentiation (e.g. MgO wt %), which would be present if apatite fractionation was important. Thus, we assume that apatite was not involved in fractional crystallization. The negative P anomalies in the mantle-normalized incompatible element diagrams (Fig. 6a and b) probably reflect the presence of residual apatite in the mantle source

region. The broad negative correlation between P/P* and La/Yb indicates increases in the P contents of the primitive magmas with increasing degree of partial melting of the mantle source (Fig. 15 g and h). This indicates that residual apatite in the mantle source region preferentially enters the melt during the partial melting process.

Trace element modelling

On the basis of the above discussion we propose that the dominant constraints on the composition of the primitive magmas in north Tibet are the degree of partial melting, the amount of subducted sediment melt added to the mantle source and the presence of residual phases in the source (e.g. phlogopite, rutile, titanite, apatite). Compared with subduction-derived fluids, partial melts of subducted sediments should have higher Th contents (Hawkesworth *et al.*, 1997*a*; Elburg *et al.*, 2002). To evaluate quantitatively the relative roles of the degree of partial melting and the amount of subduction-derived sediment melt induced metasomatism, and simultaneously to minimize the effects of fractional crystallization on the composition of the potassium-rich primitive magmas in north Tibet, we have selected the incompatible trace element ratios La/Yb and Th/Sm as simulated calculation parameters; these ratios may be considered indicative of the degree of partial melting and the amount of subducted sediment partial melt added, respectively. Both La/Yb and Th/Sm ratios are not significantly changed by small amounts of fractional crystallization of olivine and clinopyroxene, which are predicted by the major and trace element variations (Fig. 4a–d and l) and AFC modelling (Fig. 11). The model assumes that the primitive magmas in north Tibet were generated through two main processes: (1) enrichment of a depleted mantle source component with a partial melt of subducted sediment, followed by (2) partial melting of the resultant enriched mantle.

In developing an appropriate mantle melting model for the petrogenesis of the potassic and ultrapotassic magmas it is clear that we cannot assume modal melting because minor phases such as phlogopite, titanite, spinel, apatite and clinopyroxene preferentially enter the melt with respect to olivine, orthopyroxene and rutile during mantle partial melting process (Wilson, 1989; Guo *et al.*, 2005). Moreover, the distinctive and systematic trends in trace element abundances and their ratios (Figs 6 and 15) exhibited by the primitive magmas suggest that some minerals (e.g. phlogopite, apatite and titanite) may be preferentially consumed ahead of others (e.g. olivine, orthopyroxene and rutile) with increasing degree of partial melting of the mantle source region. Thus, the proportions of the different mineral phases in the mantle source region will vary during progressive partial melting. Because we do not have enough evidence to quantitatively determine whether there was a continuous change in the bulk composition of the system during the mantle partial melting process, we have not adapted a fractional melting model. Consequently, a non-modal batch melting model (Wilson, 1989) was used to simulate the mantle partial melting process and to constrain changes in melt composition as some phases become preferentially exhausted in the residue as the degree of the partial melting increases.

Although the composition of the mantle beneath the three basement terranes (i.e. the North Qiangtang, Songpan–Ganzi and North Kunlun terranes) in north Tibet, prior to modification by the subducted sediment melt, appears to have been close to that of Indian MORB-source mantle, based on the trace element and Sr–Nd–Pb isotope compositions of the most primitive magmas (Figs 8 and 14a), the concentrations of La (1·9–4·1 ppm), Th (0·079–0·205 ppm), Sm (2·0–3·5) and Yb (2·3–3·5 ppm) in Indian MORB are rather variable (Rehkämper & Hofmann, 1997). Therefore, in our modelling we have used normal MORB (i.e. N-MORB; Sun & McDonough, 1989) source mantle instead as the source material; this is assumed to have 0·1 times N-MORB (Sun & McDonough, 1989) concentrations of the relevant trace elements (i.e. Th 0·012 ppm, La 0·250 ppm, Sm 0·263 ppm and Yb 0·305 ppm) based on the assumption that MORB magmas are results of ~10% partial melting of their mantle source (Wilson, 1989).

Ratios of the incompatible trace elements (e.g. La/Yb, Th/Sm) in the primitive Tibetan magmas should not be significantly modified by partial melting processes, although these ratios in the partial melt of the subducted sediment may be slightly increased compared with the subducted bulk sediment because of the slightly different incompatibility between La and Yb, and Th and Sm. We have used the La/Yb and Th/Sm ratios of average GLOSS (Plank & Langmuir, 1998) to approximate those of a partial melt of the subducted sediment. The concentrations of the trace elements Th, La, Sm and Yb in the subducted sediment are 6·91 ppm, 28·8 ppm, 5·78 ppm and 2·76 ppm, respectively.

Johnson *et al.* (1990) systematically studied residual abyssal peridotites collected from the American–Antarctic and Southwest Indian Ridge and indicated modal proportions of clinopyroxene ranging from 2 to 12%. Because clinopyroxene is preferentially incorporated into the melt during mantle partial melting, compared with olivine and orthopyroxene, the initial proportion of clinopyroxene in MORB-source mantle should be higher than 12%. Johnson (1998) and Hellebrand *et al.* (2002) indicated that the spinel peridotite modes in MORB-source mantle are olivine (53%), orthopyroxene (27%), clinopyroxene (17%) and spinel (3%). Similarly, Bizimis *et al.* (2000) suggested the following modal mineralogy for MORB-source mantle: olivine

Table 9: Modal proportions of minerals in the mantle source region and their partition coefficients

Mineral	Modal (%)	Th	Sm	La	Yb
Apatite	0·5	17·1	14·6	3·7	8·1
Clinopyroxene	18	0·0127	0·312	0·031	0·265
Olivine	45	0·0000062	0·0013	0·0004	0·2685
Orthopyroxene	30	0·0000225	0·011	0·00045	0·097
Phlogopite	2	0·0145	0·0365	0·0322	0·0484
Rutile	0·5	0·54	—	0·0055	0·0093
Spinel	2	—	0·01	0·01	0·01
Titanite	2	17·1	204	—	104
D		0·43	4·21	0·03	2·32

D, bulk partition coefficient. —, no data are available. Data source: GERM (Geochemical Earth Reference Model) home page, http://www.earthref.org/.

(55%), orthopyroxene (25%), clinopyroxene (18%) and spinel (2%). Infiltration of a subducted sediment-derived, silica-rich partial melt into the mantle will clearly change the modal mineralogy, and would increase the content of orthopyroxene at the expense of olivine (Kelemen *et al.*, 1998). In addition, considering the formation of new mineral phases (e.g. phlogopite, titanite, rutile and apatite) as a result of metasomatism of the mantle beneath the three terranes in north Tibet, we have assumed that the resultant minerals and their modal proportions in the metasomatized mantle source region after introduction of the subduction-derived sediment partial melt are olivine (45%), orthopyroxene (30%), clinopyroxene (18%), spinel (2%), phlogopite (2%), titanite (2%), rutile (0·5%) and apatite (0·5%). The mineral–melt partition coefficients for Th, La, Sm and Yb in the mineral phases used in the model (Table 9) are based on those from the GERM (Geochemical Earth Reference Model) website (http://www.earthref.org/). Phlogopite phenocrysts are present in the K-rich magmatic rocks in north Tibet (Table 2), which suggests hydrous partial melting conditions. Following Bizimis *et al.* (2000), the melting mineral mode for the hydrous melting condition was considered to be: clinopyroxene (0·56), olivine (–0·10), orthopyroxene (0·52) and spinel (0·02). Because additional mineral phases (e.g. phlogopite, titanite, rutile and apatite) were formed during mantle metasomatism in north Tibet, and phlogopite, apatite, spinel, clinopyroxene and titanite are considered to be completely consumed into the melt before rutile, olivine and orthopyroxene based on the above interpretations (Figs 15 and 16), we, therefore, assumed the following mineral melting mode (i.e. the proportion of the mineral phases entering the melt): apatite (0·015), clinopyroxene (0·55), olivine (–0·10), orthopyroxene (0·40), phlogopite (0·062), rutile (0·003), spinel (0·02) and titanite (0·05).

On the basis of the above data, following the approach of Guo *et al.* (2005), we carried out non-modal batch melting model calculations. The results of the trace element modelling show that the degree of mantle partial melting required to fit the data ranges from <0·1% to ~15%, and that the proportion of subducted sediment-derived partial melt added to the mantle source ranges from 0% to around 10% for the primitive magmas (Table 10 and Fig. 17). Moreover, generation of the primitive magmas in the North Qiangtang terrane requires higher amounts (0·5–10%) of the sediment partial melt added to the mantle source compared with the Songpan–Ganzi and North Kunlun terranes (<2%). Thus, compared with the North Qiangtang terrane, both the Songpan–Ganzi and North Kunlun terranes appear to have experienced less supra-subduction zone metasomatism prior to the generation of the K-rich magmas. It should be noted that the actual proportions of subducted sediment-derived partial melt added would be slightly lower than the model results (Fig. 17) because the La/Yb and Th/Sm ratios are likely to be slightly higher in the subducted sediment-derived partial melt than in the bulk sediment.

The model results support the inferences made earlier based on the trace element (Figs 6 and 7) and Sr–Nd–Pb isotope data (Fig. 8), which confirm the heterogeneity in composition of the mantle source regions of the primitive potassium-rich magmatic rocks beneath the three terranes in north Tibet. It should be noted that the modelling results depend on the selection of a number of initial parameters, for example, the mantle source and subducted sediment melt compositions, and the partition coefficients and the proportions of residual mineral phases. However, sensitivity calculations indicate that the effect of variation in these parameters (e.g. composition of the mantle source and subducted sediment melt and the partition coefficients of the residual minerals for Th, La, Sm and Yb) on the final results of the modelling is not significant; this is 1–4% for Th/Sm and 3–7% for La/Yb ratios. The variation trends of La/Yb and Th/Sm ratios are similar even when the initial parameters are changed significantly (e.g. proportions of residual mineral phases). The subducted sediment melt has higher contents of K and Ba than N-MORB-source mantle (Fig. 6d). The average concentrations of K and Ba in the primitive magmatic rocks of the North Qiangtang terrane are higher than those in the Songpan–Ganzi and North Kunlun terranes (Table 3 and Electronic Appendix). This, combined with higher proportions of the sediment melt added to the mantle source beneath the North Qiangtang terrane than beneath the Songpan–Ganzi and North Kunlun terranes (Fig. 17), suggests that the subducted sediment melt is a good agent for producing K

Table 10: Results of the non-modal batch melting model

Proportion of sediment melt	0%		0·5%		1%		3%		5%		10%	
	Th/Sm	La/Yb	Th/Sm	La/Yb	Th/Sm	La/Yb	Th/Sm	La/Yb	Th/Sm	La/Yb	Th/Sm	La/Yb
Degree of melting												
0·1%	0·44	72·44	1·55	109·41	2·47	143·62	4·96	258·27	6·44	346·60	8·37	498·50
1%	0·44	54·01	1·53	81·57	2·43	107·07	4·88	192·56	6·32	258·42	8·22	371·67
5%	0·40	24·01	1·40	36·26	2·23	47·60	4·47	85·61	5·80	114·89	7·54	165·23
10%	0·35	13·02	1·24	19·67	1·97	25·82	3·95	46·43	5·12	62·30	6·66	89·61
15%	0·31	8·23	1·07	12·43	1·70	16·32	3·42	29·34	4·43	39·38	5·76	56·63

For non-modal batch partial melting, the equation $C_L/C_o = 1/(F + D - FP)$ (Wilson, 1989) was used. C_L is the concentration of a trace element in the melt. C_o is the content of a trace element in the metasomatized mantle source, which is modelled as a mixture of a depleted mantle component (m, similar to MORB-source) and subducted sediment-derived melt (s): $C_o = X_s C_s + (1 - X_s)C_m$, where X_s is the proportion of the subducted sediment-derived melt in the mantle source region, C_s is the concentration of a trace element in the subducted sediment-derived melt, C_m is the concentration of a trace element in the depleted mantle source region. D is the bulk distribution coefficient. $D = \Sigma X_i D_i$, where X_i is the weight fraction of phase i in the mineral assemblage and D_i is its crystal–liquid partition coefficient. $P = \Sigma P_i D_i$, where P_i is the proportion of phase i entering the melt. On the basis of the interpretation of the relative proportions of the mineral phases entering the melt during non-modal batch partial melting (see main text), we assumed $P = 0{\cdot}015D_{Apatite} + 0{\cdot}55D_{Clinopyroxene} - 0{\cdot}10D_{Olivine} + 0{\cdot}40D_{Orthopyroxene} + 0{\cdot}062D_{Phlogopite} + 0{\cdot}003D_{Rutile} + 0{\cdot}02D_{Spinel} + 0{\cdot}05D_{Titanite}$. F is the degree of partial melting.

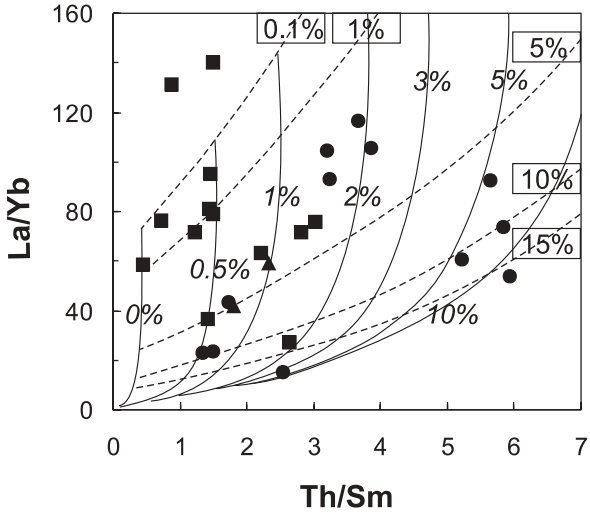

Fig. 17. Trace element modelling illustrating the variation of La/Yb vs Th/Sm in partial melts. The numbers (%) within open squares along the dashed lines represent the degree of mantle partial melting. The numbers (%) along the continuous lines (in italics) are the proportion of partial melt of subducted sediment in the mantle source region. To minimize the effect of magmatic differentiation and crustal contamination, only primitive samples with MgO >6 wt % are plotted. The symbols are as in Fig. 3a. We used a non-modal batch partial melting model and assumed depleted MORB-source mantle as the source material (see main text). The mineral phases and their modal abundances in the mantle source region after introducing the subducted sediment-derived melt are olivine (45%), orthopyroxene (30%), clinopyroxene (18%), spinel (2%), phlogopite (2%), titanite (2%), rutile (0·5%) and apatite (0·5%). Partition coefficients for La, Yb, Th and Sm in these mineral phases were taken from the GERM website (http://www.earthref.org/). (For further details see the main text.)

(and also Ba) metasomatism of the mantle source of the K-rich (and also Ba-rich) magmas in north Tibet.

Petrogenesis and geodynamic setting of the potassium-rich magmatism

As mentioned above, there are two relatively popular hypotheses for the petrogenesis of the post-collisional potassic and ultrapotassic magmas in north Tibet. The first involves southward intracontinental subduction of the Tarim and Qaidam terranes beneath the northern Tibetan Plateau (e.g. Pearce & Mei, 1988; Deng, 1989, 1991, 1998; Arnaud *et al.*, 1992; Tapponnier *et al.*, 2001; Ding *et al.*, 2003). However, the results of the trace element modelling suggest that increasing amounts of subducted sediment partial melt were added to the mantle beneath the northern Tibetan Plateau from north (North Kunlun and Songpan–Ganzi terranes) to south (North Qiangtang terrane). Moreover, there is a semi-continuous increase in age of the post-collisional K-rich magmatism from north to south in the northern part of the Tibetan Plateau (Fig. 2a). This is not easily explained by south-dipping intracontinental subduction of the Tarim and Qaidam terranes. In addition, recent deep seismic reflection profiling (Gao *et al.*, 2001; Xiao *et al.*, 2001) and petrological (e.g. Deng *et al.*, 2004) studies have shown the absence of south-dipping intracontinental subduction in north Tibet. The second hypothesis attributes the petrogenesis of the potassic and ultrapotassic magmatic rocks to convective removal of the lower part of previously thickened lithospheric mantle beneath

north Tibet (e.g. Turner *et al.*, 1993, 1996*a*; Williams *et al.*, 2004). However, this hypothesis is inconsistent with the following observations. (1) Recent studies show little or no sign of lithospheric removal or surface rebound in north Tibet since the Eocene, based on geological, geochronological and geophysical results (Tapponnier *et al.*, 2001). (2) Geophysical studies have indicated that the northern Tibetan upper mantle is characterized by inefficient regional S-wave (S_n) propagation (Ni & Barazangi, 1983; McNamara *et al.*, 1995) and low regional P-wave (P_n) velocity (McNamara *et al.*, 1995), broadly beneath the region of post-collisional potassic and ultrapotassic magmatism studied here (Fig. 1). This region of the mantle is considered to be hotter than that of the adjacent regions to a depth of 410 km (Owens & Zandt, 1997; Kosarev *et al.*, 1999; Xu *et al.*, 1999; Unsworth *et al.*, 2004); thus, it would also appear to be physically difficult to explain by delamination of cold lithosphere because the sinking of delaminated cold lithosphere would decrease the asthenospheric temperatures in this region by thermal conduction. (3) As metasomatism is likely to occur predominantly at deeper levels within the mantle lithosphere (Niu *et al.*, 2002), the remaining upper part of the lithosphere may be barren or less metasomatized. To partially melt such lithosphere is thermally difficult, but if it did happen, it would result in trace element and isotopically depleted magmas, rather than enriched potassic and ultrapotassic magmas. Thus, if the sub-continental lithospheric mantle were thickened, the post-collisional potassic and ultrapotassic magmas would have to be generated by partial melting of the lower part of the thickened lithosphere (because this is the zone of enrichment), rather than the upper part of the lithosphere. (4) Spatially, the trend of the potassic and ultrapotassic magmatic province in the different terranes of north Tibet is roughly parallel to the Himalayas (Fig. 1); this suggests that the generation of the potassic and ultrapotassic magmas is more likely to be related to northward subduction of the Indian continent, post-India–Asia collision, than to convective thinning of the lithospheric mantle (Tapponnier *et al.*, 2001). (5) The age of the post-collisional potassic and ultrapotassic magmatism in north Tibet ranges semi-continuously from 45 Ma to the present day (Fig. 2); this is unlikely to be explained by a petrogenetic model involving wholesale and sudden convective thinning of the lithospheric mantle (Yin & Harrison, 2000) on a time scale of about 5 Myr (Lenardic & Kaula, 1995), although some modifications of the convective thinning model have been proposed (e.g. Conrad & Molnar, 1999). Moreover, the decreasing trend in the age of the post-collisional potassium-rich magmatism in north Tibet from south to north (Fig. 2a) is also difficult to explain by convective thinning of the mantle lithosphere. (6) Geomorphological studies have shown that there is no evidence for sudden uplift, which is predicted by the model of convective thinning of the lithosphere (Meyer *et al.*, 1998). (7) Deng *et al.* (2004) proposed that the average lithospheric thickness beneath north Tibet has been ~150 km since initial collision of India and Asia at ~65–70 Ma. There is little evidence to support the substantial Tertiary thickening of the lithosphere (~250 km), proposed by Turner *et al.* (1996*a*), beneath north Tibet, which is required by models involving subsequent convective thinning of the mantle lithosphere. An earlier version of the second hypothesis, proposed by Turner *et al.* (1993), was based on limited geochemical data for the magmatic rocks in north Tibet, which suggested that the volcanism was younger than 13 Ma. However, the results of many new geochronological and geochemical studies of the magmatic rocks (summarized here), together with extension of the sampling area, require an alternative interpretation for the petrogenesis of the K-rich magmatism in north Tibet because the previous hypotheses can no longer explain all of the new data.

Studies of the shear-wave anisotropy of the mantle indicate that the direction of fast polarization is roughly east–west beneath Tibet (McNamara *et al.*, 1994, 1995; Hirn *et al.*, 1995; Guilbert *et al.*, 1996; Lave *et al.*, 1996; Sandvol *et al.*, 1997). Some studies have ascribed this shear-wave anisotropy to deformation of the lithospheric mantle (McNamara *et al.*, 1994; Silver, 1996), suggesting that this is a result of finite strain accumulated within the lithosphere over geological time (e.g. Davis *et al.*, 1997). The strong shear-wave anisotropy beneath the northern part of the Tibetan Plateau, including the North Qiangtang and Songpan–Ganzi terranes, suggests that the mantle lithosphere beneath these areas is highly strained (McNamara *et al.*, 1994). The sub-parallel relationship between the post-collisional potassic and ultrapotassic volcanic belts within the various terranes (Fig. 1) and the fabric indicated by the seismic anisotropy data may indicate a relationship between the deformation of the Tibetan lithospheric mantle and K-rich magma generation processes. In addition, Cenozoic tectonic movements in north Tibet are characterized by large-scale strike-slip faults (Tapponnier & Molnar, 1977), some of which are located within older tectonic suture zones [e.g. South Kunlun suture, Jinsha suture; for further discussion see Xu *et al.* (1999) and Yin & Harrison (2000)]. There are a number of pull-apart basins and push-up structures along these large strike–slip faults in north Tibet, which are associated with movements along the faults (Deng, 1998; Xu *et al.*, 1999; Yin & Harrison, 2000). Geophysical studies have shown that these strike-slip faults may penetrate the lithospheric mantle (e.g. Tapponnier *et al.*, 2001). Detailed field studies have indicated that most of the potassic and ultrapotassic magmatism in the northern part of the Tibetan Plateau is distributed along these huge fault systems, which are either transpressional or

strike-slip (e.g. Altyn-Tagh fault) in nature; some of the volcanic fields are located within pull-apart basins (e.g. the Ashikule volcanic field; Fig. 1) or at intersections between extensional or transtensional structures and compressional or strike-slip faults [QBGMR (Qinghai Bureau of Geology and Mineral Resources), 1991; Deng, 1998; Chi *et al.*, 1999; Lai & Liu, 2001]. This suggests that the lithospheric mantle exerts a strong control over post-collisional K-rich magma generation processes in the northern Tibetan Plateau.

Previous studies (e.g. Lai *et al.*, 1996; Owens & Zandt, 1997; Wu *et al.*, 2001; Luo *et al.*, 2003) have suggested that during the Cenozoic the sub-continental lithospheric mantle beneath north Tibet (i.e. the North Qiangtang and Songpan–Ganzi terranes) was relatively thin and weak compared with the lithosphere beneath the Indian continent to the south and that beneath the Tarim and Qaidam terranes to the north (Fig. 1). Moreover, geophysical studies indicate that the base of the lithosphere is between 90–120 km (An *et al.*, 1993) and 140–160 km (Zhu *et al.*, 2002) beneath north Tibet. Deng *et al.* (2004) proposed that the average lithosphere thickness beneath north Tibet and the terranes of Tarim and Qaidam (Fig. 1) has been ~150 km and ~200 km, respectively, since the initial collision of India and Asia in south Tibet at ~65–70 Ma, based on geophysical, petrological and tectonic studies. Zhou & Murphy (2005) pointed out that the Indian continental lithosphere is stronger and thicker (>200 km) relative to the Tibetan mantle lithosphere. Compared with the relatively thick, rigid and strong lithosphere beneath the stable Tarim and Qaidam terranes (or cratons) to the north and the Indian continental craton to the south, the sub-continental lithospheric mantle beneath north Tibet is relatively thin and weak. This probably results from earlier episodes of subduction-related magmatism and metasomatism, leading to easier deformation of the lithospheric mantle beneath north Tibet during continental collision and the northward underthrusting of the Indian continental lithosphere beneath the Tibetan Plateau lithosphere (Owens & Zandt, 1997; Kosarev *et al.*, 1999; Zhou & Murphy, 2005). The advancing, relatively thick, Indian continental lithosphere is considered to have pushed the asthenosphere beneath Tibet northwards until it was stopped by the thick Tarim and Qaidam continental lithosphere in the north of Tibet (Fig. 18). The relatively hot asthenosphere was squeezed up between the advancing Indian continental lithosphere front and the backstop of the older Asian continental lithosphere (Owens & Zandt, 1997; Kosarev *et al.*, 1999), causing localized partial melting. Such a model is supported by the low P-wave velocities in the upper mantle beneath the Tibetan Plateau (Xu *et al.*, 1999; Zhou & Murphy, 2005). The larger volumes (Table 1) and denser outcrops (Fig. 1) of the post-collisional K-rich magmatic rocks between 85°E to 93°E (longitude) in north Tibet compared with those in the western and eastern portions may be further explained by a steeper angle of underthrusting of the Indian continental lithosphere beneath central Tibet than beneath the west and east Tibetan Plateau; this has been verified by recent seismic tomography results (Zhou & Murphy, 2005). An asthenospheric mantle wedge appears to exist between the overlying northern Tibetan lithosphere and the underlying subducted Indian slab based on seismic tomography data (Zhou & Murphy, 2005). As discussed in previous sections, partial melts of subducted Indian passive margin sediments have probably metasomatized this asthenospheric wedge, forming the enriched mantle source region of the primitive magmas in north Tibet. The metasomatized asthenospheric wedge geochemically comprises two components: MORB-source mantle (normal asthenospheric mantle beneath north Tibet) and subducted sediment melt (partial melt of the subducted Indian passive margin sediments). In many respects, this may be indistinguishable from lithospheric mantle metasomatized during earlier episodes of subduction. Thus we cannot unequivocally distinguish between asthenospheric and lithospheric mantle contributions to the source of the primary magmas. Partial melts formed by upwelling of the metasomatized asthenospheric mantle would infiltrate enriched domains within the overlying Tibetan mantle lithosphere, inducing further partial melting. An alternative possibility is that the mantle source region was located at the boundary between the lithosphere and asthenosphere, including both enriched domains at the base of the lithosphere and the underlying metasomatized asthenospheric mantle. For the Qiangtang terrane, it is likely that there was a minimal contribution from the mantle lithosphere if the model of Kapp *et al.* (2003) for Late Triassic–Early Jurassic flat slab subduction is accepted.

Relatively low degrees of partial melting of highly enriched mantle sources (in both lithosphere and asthenosphere) resulted in potassic and ultrapotassic magmas that escaped to the surface along reactivated diffuse palaeo-plate boundaries (lithospheric shear zones) and/or strike-slip faults. This explains the generally small volume yet widespread distribution of the potassic and ultrapotassic magmatism in north Tibet (Fig. 1a and Table 1). Geophysical studies (Owens & Zandt, 1997; Chen & Ozalaybey, 1998; Kosarev *et al.*, 1999; Xu *et al.*, 1999; Yin & Harrison, 2000) indicate that the northern edge of the subducted Indian continental lithosphere beneath Tibet currently lies between the North Qiangtang and South Qiangtang terranes (at ~33°N), and that there is upwelling of hot metasomatized asthenosphere beneath the North Qiangtang terrane, Songpan–Ganzi terrane and the South Kunlun suture in the northern part of the Tibetan

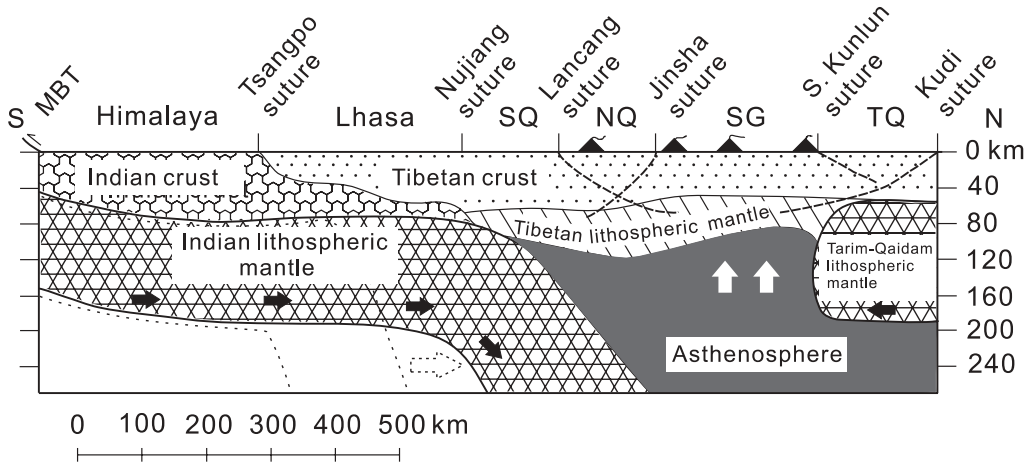

Fig. 18. Geodynamic model for the petrogenesis of the post-collisional potassic and ultrapotassic magmatism in the northern part of the Tibetan Plateau. The diagram shows a north–south cross-section. Dashed lines represent the Lancang, Jinsha, South Kunlun and Kudi sutures, matching the locations of previous subduction zones during the convergence of the Proto- and Palaeo-Tethyan oceans. Thick black arrows in the Indian and Tarim–Qaidam continental lithospheric mantle show the convergence direction between India and Asia. Upward white arrows in the asthenosphere indicate the upwelling of the asthenospheric mantle because of the northward underthrusting of the Indian continental lithospheric mantle. Dotted line with arrow shows the changing position of the underthrust Indian continental lithospheric mantle with time. This diagram is based on the studies by Owens & Zandt (1997), Kosarev *et al.* (1999), Xu *et al.* (1999), Zhao *et al.* (2003) and Zhou & Murphy (2005). MBT, Main Boundary thrust; N, north; NQ, North Qiangtang terrane; S, south; SG, Songpan–Ganzi terrane; SQ, South Qiangtang terrane; TQ, Tarim–Qaidam terranes. Filled triangles represent the locations of post-collisional potassium-rich magmatism in north Tibet.

Plateau (Figs 1 and 18). This has caused Pliocene–Quaternary magmatism in this area, including an active volcano at Ashikule (Fig. 1 and Table 1), located along the South Kunlun suture at the northern edge of the Tibetan Plateau. The zone of upwelling asthenosphere, inferred from seismic tomographic data, beneath north Tibet roughly overlaps with the distribution of the potassic and ultrapotassic magmatism in the northern part of the Tibetan Plateau (Fig. 1a; Wittlinger *et al.*, 1996; Owens & Zandt, 1997; Deng, 1998; Kosarev *et al.*, 1999; Xu *et al.*, 1999; Zhou & Murphy, 2005).

As discussed above, the sub-continental lithospheric mantle beneath the Qaidam and South Kunlun terranes probably also experienced metasomatism as a consequence of subduction of the Proto-Tethys and South Kunlun oceans; however, no outcrops of post-collisional potassium-rich magmatic rocks have been found in these terranes (Fig. 1a). The plausible reasons are that (1) the sub-continental lithospheric mantle beneath the Qaidam and South Kunlun terranes is rigid and relatively thick and/or (2) the upwelling of hot metasomatized asthenosphere has not yet spread northwards beneath them (Owens & Zandt, 1997; Kosarev *et al.*, 1999). However, the Pulu volcanic field, which is located in the North Kunlun terrane (Fig. 1a), is located on the intersection between the Altyn Tagh strike-slip fault, which is inferred to reach the base of the lithosphere (Tapponnier *et al.*, 2001), and a series of north–south-trending extensional faults (Deng, 1998). This may have induced a zone of decompression partial melting (Yin & Harrison, 2000). Thus, two factors are requisites for the generation of the post-collisional potassic and ultrapotassic magmatic rocks in north Tibet: one is the presence of thin and weak (i.e. easily deformed and disrupted) lithosphere that has previously been metasomatized and enriched, and another is the upwelling of hot metasomatized asthenosphere beneath the lithosphere.

Timing and mechanism of uplift of the northern Tibetan Plateau, constrained by the K-rich magmatism

Upwelling of the asthenosphere, resulting from the northward underthrusting of the Indian continental lithosphere, may have led to the uplift of the overlying lithospheric mantle beneath the northern Tibetan Plateau. This, in turn, resulted in uplift of north Tibet. The progressively northward underthrusting of the Indian continental lithosphere may have resulted in continuous upwelling of the asthenosphere beneath north Tibet since the initial collision of India and Asia in south Tibet at ~65–70 Ma. This in turn would lead to progressive uplift of the northern Tibetan Plateau since 65–70 Ma, generating the highest plateau in the world. As a consequence of upwelling of the asthenosphere, K-rich magmatism has formed with an approximately continuous age spectrum from ~45 Ma to the present day (Fig. 2).

Lithospheric convergence between India and Asia in Tibet since 65–70 Ma has resulted in underthrusting of the Indian continental lithosphere, pushing the asthenosphere beneath north Tibet progressively further northwards (Owens & Zandt, 1997); however, the Tarim and

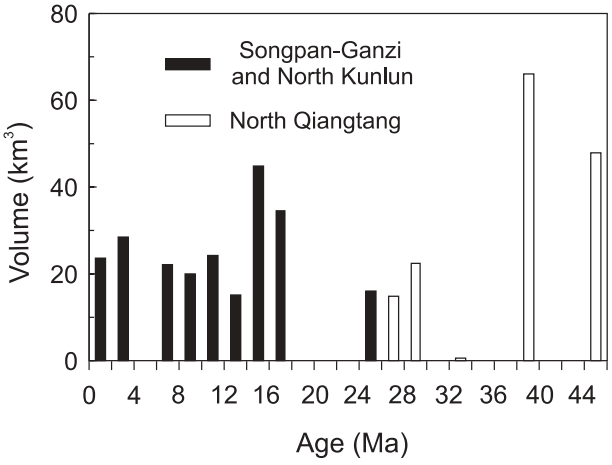

Fig. 19. Erupted volume (km^3) vs average age (Ma) of the volcanic fields in north Tibet. Data for the erupted volumes and the average ages of the volcanic fields are from Table 1.

Qaidam lithosphere has remained stable as there is no south-dipping intracontinental subduction in north Tibet. Consequently, uplift of the North Qiangtang terrane should have been earlier than that of the Songpan–Ganzi and Kunlun terranes. This inference may explain the progressive decrease in the age of the potassic and ultrapotassic magmatism in north Tibet from south to north (Fig. 2a) in terms of the northward migration of the region of partial melting of the enriched asthenospheric mantle. This suggests that both the post-collisional, K-rich magmatism and uplift of the northern Tibetan Plateau resulted from the upwelling of the asthenosphere. If this inference is correct, the age of the magmatism might indicate the timing of relatively rapid and large-scale uplift of the northern Tibetan Plateau.

Figure 19 indicates the volume of magmatism as a function of the age of the K-rich rocks in north Tibet. This shows that post-collisional magmatism occurred continuously between 45 Ma and the present day with peaks at 45–38 Ma, 30–24 Ma and 18 Ma–present. This may suggest that rapid uplift of the northern Tibetan Plateau occurs in similar pulses. Because the subcontinental lithospheric mantle beneath north Tibet is thinner and weaker compared with the lithospheric mantle beneath the Tarim and Qaidam terranes (or cratons) to the north and the Indian continental plate to the south, the uplift of the lithosphere beneath north Tibet, as a consequence of the upwelling of the asthenosphere, may have been earlier than indicated by the age of the K-rich magmatism, because a period of time would be required for partial melting of the enriched mantle source, AFC processes in the crust and upward migration of the magmas. This inference is consistent with our detailed field observations; some volcanic fields are located on the top of the high mountains at an average elevation of 5000 m above sea level (e.g. Ashikule), whereas other volcanic fields are located on erosion plains (e.g. Yulinshan and Bamaoqiongzong; Fig. 1a). Well-preserved outcrops in the volcanic fields indicate that volcanism must have occurred after the formation of the high mountains and the erosion plains; otherwise, the effusive volcanic rocks would have been removed by subsequent strong erosion and weathering.

CONCLUSIONS

On the basis of major and trace element and Sr–Nd–Pb isotope data, combined with previous geochronological and geophysical studies, we propose a petrogenetic model to explain the spatial and temporal variations in the distribution and geochemical characteristics of the post-collisional potassic and ultrapotassic magmatism in the northern part of the Tibetan Plateau. This model advocates an important role for enrichment of the asthenospheric mantle beneath the northern part of the plateau as a consequence of the underthrust Indian continental lithosphere. Locally, there may also be a contribution from lithospheric mantle enriched during earlier episodes of subduction of the Proto- and Palaeo-Tethys oceans. Partial melts derived from subducted sediments, including Indian passive margin sediments and Proto- and Palaeo-Tethyan continental margin sediments, were the main agents that caused the enrichment of the asthenospheric mantle source of the primitive northern Tibetan magmas. The mantle-normalized incompatible element patterns of the most primitive mafic magmas (MgO >6 wt %) in north Tibet are comparable with those of subduction-related magmatic rocks; these are attributed to a combination of addition of subducted sediment melts to the mantle source and the presence of two Ti-rich residual mineral phases. The amount of subducted sediment melt added to the mantle source region of the potassic and ultrapotassic magmas in the North Qiangtang terrane is higher than that in the source of the magmas in the Songpan–Ganzi and North Kunlun terranes, resulting in compositional differences between the primitive magmatic rocks in the North Qiangtang terrane and those in the Songpan–Ganzi and North Kunlun terranes. The subducted sediment melt is a good agent for producing K (and also Ba) metasomatism of the mantle source of the K-rich (and also Ba-rich) magmas in north Tibet. The composition of the mantle source prior to the introduction of the subducted sediment-derived melts appears to be similar in all three terranes, corresponding to that of Indian MORB-source mantle (i.e. asthenospheric mantle). The increasing input of partial melt of subducted sediment from north to south before the generation of the Tertiary–recent potassic and ultrapotassic magmas, together with the southward

increase in the age of the post-collisional potassic and ultrapotassic magmatic rocks, cannot be easily explained by south-dipping intracontinental subduction of the Tarim and Qaidam terranes. However, this is consistent with northward underthrusting of the Indian continental lithosphere. The evidence presented here does not support the hypothesis that the post-collisional K-rich magmas were generated by convective removal (delamination) of the lower part of a previously thickened lithospheric mantle root beneath north Tibet. Our preferred model involves the partial melting/upwelling of hot metasomatized asthenosphere beneath north Tibet as a result of the northward underthrusting of the Indian continental lithosphere and rapid convergence between the Indian and Asian lithosphere. The uplift of the northern Tibetan Plateau is also inferred to result from the upwelling of the asthenosphere and may be periodic at 45–38 Ma, 30–24 Ma and 18 Ma–present. AFC processes, operating in the middle crust in the North Qiangtang terrane and in the upper crust in the Songpan–Ganzi and North Kunlun terranes, can explain the range of evolved (MgO <6 wt %) magmas types, which have similar compositions in the three terranes of north Tibet.

ACKNOWLEDGEMENTS

We thank J. C. Lin, N. Sun and Q. Zhao for their friendship and guidance during the field work. Further logistic help was provided during the field campaigns by the Qinghai and Tibet Bureaus of Geology and Mineral Resources of China. This study was financially supported by a joint project (2003–2005) between the Royal Society of London and the National Natural Science Foundation of China (NSFC). Yaoling Niu is particularly acknowledged for his help in this study. This work was also supported by grants from the NSFC (40372045 and 40473023). Julian Pearce, Helen Williams and Wendy Bohrson are acknowledged for their constructive reviews of an earlier version of the manuscript. We also thank the editor, John Gamble, for his support.

SUPPLEMENTARY DATA

Supplementary data for this paper are available at *Journal of Petrology* online.

REFERENCES

An, C., Song, Z., Chen, G., Chen, L., Zhuang, Z., Fu, Z., Lü, Z. & Hu, J. (1993). 3-D shear wave velocity structure in northwestern China. *Acta Geophysica Sinica* **36**, 317–325 (in Chinese with English abstract).

Arnaud, N. O., Vidal, Ph., Tapponnier, P., Matte, Ph. & Deng, W. M. (1992). The high K_2O volcanism of northwestern Tibet: geochemistry and tectonic implications. *Earth and Planetary Science Letters* **111**, 351–367.

BGMRXAR (Bureau of Geology and Mineral Resources of Xizang Autonomous Region) (1993). *Regional Geology of Xizang (Tibet) Autonomous Region*. Beijing: Geological Publishing House, 707 pp. (in Chinese with English abstract).

Bizimis, M., Salters, V. J. M. & Bonatti, E. (2000). Trace and REE content of clinopyroxenes from supra-subduction zone peridotites: implications for melting and enrichment processes in island arcs. *Chemical Geology* **165**, 67–85.

Bohrson, W. A. & Spera, F. J. (2001). Energy-constrained open-system magmatic processes II: application of energy-constrained assimilation–fractional crystallization (EC-AFC) model to magmatic systems. *Journal of Petrology* **42**, 1019–1041.

Brenan, J. M., Shaw, H. F., Ryerson, F. J. & Phinney, D. L. (1995). Mineral–aqueous fluid partitioning of trace elements at 900°C and 2·0 GPa: constraints on the trace element chemistry of mantle and deep crustal fluids. *Geochimica et Cosmochimica Acta* **59**, 3331–3350.

Chen, W.-P. & Ozalaybey, S. (1998). Correlation between seismic anisotropy and Bouguer gravity anomalies in Tibet and its implications for lithospheric structures. *Geophysical Journal International* **135**, 93–101.

Chi, X., Li, C., Jin, W., Liu, S. & Yang, R. (1999). Spatial–temporal evolution of Cenozoic volcanism and uplifting in north Tibet. *Geological Review* **45**, 978–986 (in Chinese with English abstract).

Chung, S.-L., Lo, C.-H., Lee, T.-Y., Zhang, Y., Xie, Y., Li, X., Wang, K.-L. & Wang, P.-L. (1998). Diachronous uplift of the Tibetan plateau starting 40 Myr ago. *Nature* **394**, 769–773.

Class, C., Miller, D. M., Goldstein, S. L. & Langmuir, C. H. (2000). Distinguishing melt and fluid subduction components in Umnak volcanics: Aleutian arc. *Geochemistry, Geophysics, Geosystems* **1**, 1999GC000010.

Conrad, C. P. & Molnar, P. (1999). Convective instability of a boundary layer with temperature- and strain-rate-dependent viscosity in terms of 'available buoyancy'. *Geophysical Journal International* **139**, 51–68.

Coward, M. P., Kidd, W. S. F., Pan, Y., Shackleton, R. M. & Zhang, H. (1988). The structure of the 1985 Tibet geotraverse, Lhasa to Golmud. *Philosophical Transactions of the Royal Society of London, Series A* **327**, 307–336.

Davis, P., England, P. & Houseman, G. (1997). Comparison of shear wave splitting and finite strain from the India–Asia collision zone. *Journal of Geophysical Research* **102**,27511–27522.

Deng, J. F., Mo, X. X., Zhao, H. L., Wu, Z. X., Luo, Z. H. & Su, S. G. (2004). A new model for the dynamic evolution of Chinese lithosphere: 'continental roots–plume tectonics'. *Earth-Science Reviews* **65**, 223–275.

Deng, W. (1989). Cenozoic volcanic rocks in the northern Ngari district of the Tibet: a discussion on the intracontinental subduction. *Acta Petrologica Sinica* **3**, 1–11 (in Chinese with English abstract).

Deng, W. (1991). Geology, geochemistry and ages of the shoshonitic lavas in the central Kunlun orogenic belt. *Scientia Geologica Sinica* **3**, 201–213 (in Chinese with English abstract).

Deng, W. (1993). A study on trace element and Sr, Nd isotopic geochemistry of Cenozoic potassic volcanic rocks in north Tibet. *Acta Petrologica Sinica* **9**, 379–387 (in Chinese with English abstract).

Deng, W. (1998). *Cenozoic Intraplate Volcanic Rocks in the Northern Qinghai–Xizang (Tibetan) Plateau*. Beijing: Geological Publishing House, 180 pp. (in Chinese with English abstract).

Deng, W., Zheng, X. & Yukio, M. (1996). Petrological characteristics and ages of Cenozoic volcanic rocks in the Hoh Xil mountains, Qinghai province, China. *Acta Petrologica et Mineralogica* **15**, 289–298 (in Chinese with English abstract).

Deng, X., Ding, L., Liu, X., Yin, A., Kapp, P. A., Murphy, M. A. & Manning, C. E. (2002). Geochemical characteristics of the blueschists and its tectonic significance in the central Qiangtang area, Tibet. *Acta Petrologica Sinica* **18**, 517–525 (in Chinese with English abstract).

DePaolo, D. J. (1988). *Neodymium Isotope Geochemistry: an Introduction*. New York: Springer, 230 pp.

Desio, A. (1979). Geological evolution of the Karakorum. In: Farah, A. & DeJong, K. A. (eds) *Geodynamics of Pakistan Geology*. Islamabad: Geological Survey of Pakistan, 111–124.

Dewey, J. F., Shackleton, R. M., Chang, C. & Sun, Y. (1988). The tectonic evolution of the Tibetan plateau. *Philosophical Transactions of the Royal Society of London, Series A* **327**, 379–413.

Ding, L., Zhang, J., Zhou, Y., Deng, W., Xu, R. & Zhong, D. (1999). Tectonic implication on the lithosphere evolution of the Tibet plateau: petrology and geochemistry of sodic and ultrapotassic volcanism in northern Tibet. *Acta Petrologica Sinica* **15**, 408–421 (in Chinese with English abstract).

Ding, L., Kapp, P., Zhong, D. & Deng, W. (2003). Cenozoic volcanism in Tibet: evidence for a transition from oceanic to continental subduction. *Journal of Petrology* **44**, 1833–1865.

Elburg, M. A., Bergen, M. V., Hoogewerff, J., Foden, J., Vroon, P., Zulkarnain, I. & Nasution, A. (2002). Geochemical trends across an arc–continent collision zone: magma sources and slab–wedge transfer processes below the Pantar Strait volcanoes, Indonesia. *Geochimica et Cosmochimica Acta* **66**, 2771–2789.

Elliott, T., Planck, T., Zindler, A., White, W. & Bourdon, B. (1997). Element transport from slab to volcanic front at the Mariana arc. *Journal of Geophysical Research* **102**,14991–15019.

Fan, W. M., Guo, F., Wang, Y. J. & Ge, L. (2003). Late Mesozoic calc-alkaline volcanism of post-orogenic extension in the northern Da Hinggan Mountains, northeastern China. *Journal of Volcanology and Geothermal Research* **121**, 115–135.

Feng, Q., Ye, M. & Zhang, Z. (1997). Early Carboniferous radiolarians from western Yunnan. *Acta Micropalaeontologica Sinica* **14**, 79–92 (in Chinese with English abstract).

Foley, S. F. & Wheller, G. E. (1990). Parallels in the origin of the geochemical signatures of island arc volcanics and continental potassic igneous rocks: the role of residual titanates. *Chemical Geology* **85**, 1–18.

Foley, S. F., Venturelli, G., Green, D. H. & Toscani, L. (1987). The ultrapotassic rocks: characteristics, classification and constraints for petrogenetic models. *Earth-Science Reviews* **24**, 81–134.

Foley, S. F., Jackson, S. E., Fryer, B. J., Greenough, J. D. & Jenner, G. A. (1996). Trace element partition coefficients for clinopyroxene and phlogopite in an alkaline lamprophyre from Newfoundland by LAM-ICP-MS. *Geochimica et Cosmochimica Acta* **60**, 629–638.

Foley, S. F., Barth, M. G. & Jenner, G. A. (2000). Rutile/melt partition coefficients for trace elements and an assessment of the influence of rutile on the trace element characteristics of subduction zone magmas. *Geochimica et Cosmochimica Acta* **64**, 933–938.

Gao, R., Li, P., Li, Q., Guan, Y., Shi, D., Kong, X. & Liu, H. (2001). Deep process of the collision and deformation on the northern margin of the Tibetan Plateau: revelation from investigation of the deep seismic profiles. *Science in China (Series D)* **44**(supplement), 71–78 (in English).

Gao, S., Ling, W., Qiu, Y., Lian, Z., Hartmann, G. & Simon, K. (1999). Contrasting geochemical and Sm–Nd isotopic compositions of Archean metasediments from the Kongling high-grade terrain of the Yangtze craton: evidence for cratonic evolution and redistribution of REE during crustal anatexis. *Geochimica et Cosmochimica Acta* **63**, 2071–2088.

Gill, J. B. (1981). *Orogenic Andesites and Plate Tectonics*. Berlin: Springer, 390 pp.

Goldstein, S. L., O'Nions, R. K. & Hamilton, P. J. (1984). A Sm–Nd isotopic study of atmospheric dusts and particulates from major river systems. *Earth and Planetary Science Letters* **70**, 221–236.

Govindaraju, K. (1994). Compilation of working values and sample description for 383 geostandards. *Geostandards Newsletter* **18**(special issue), 1–15.

Green, T. H. (1994). Experimental studies of trace-element partitioning applicable to igneous petrogenesis—Sedona 16 years later. *Chemical Geology* **117**, 1–36.

Green, T. H., Blundy, J. D., Adam, J. & Yaxley, G. M. (2000). SIMS determination of trace element partition coefficients between garnet, clinopyroxene and hydrous basaltic liquids at 2–7·5 GPa and 1080–1200°C. *Lithos* **53**, 165–187.

Guilbert, J., Poupinet, G. & Jiang, M. (1996). A study of azimuthal P wave residuals and shear wave splitting across the Kunlun range (Northern Tibetan Plateau). *Physics of the Earth and Planetary Interiors* **95**, 167–174.

Guo, Z., Deng, J., Xu, Z., Mo, X. & Luo Z. (1998). Late Palaeozoic–Mesozoic intracontinental orogenic process and intermediate–acidic igneous rocks from the Eastern Kunlun mountains in north Tibet, northwestern China. *Geoscience* **12**, 344–352 (in Chinese with English abstract).

Guo, Z., Hertogen, J., Liu, J., Pasteels, P., Boven, A., Punzalan, L., He, H., Luo, X. & Zhang, W. (2005). Potassic magmatism in western Sichun and Yunnan provinces, SE Tibet, China: petrological and geochemical constraints on petrogenesis. *Journal of Petrology* **46**, 33–78.

Hacker, B. R., Gnos, E., Ratschbacher, L., Grove, M., McWilliams, M., Sobolev, S. V., Wan, J. & Wu, Z. (2000). Hot and dry deep crustal xenoliths from Tibet. *Science* **287**, 2463–2466.

Harris, N. B. W., Xu, R., Lewis, C. L. & Jin, C. (1988*a*). Plutonic rocks of the 1985 Tibet geotraverse, Lhasa to Golmud. *Philosophical Transactions of the Royal Society of London, Series A* **327**, 145–168.

Harris, N. B. W., Xu, R., Lewis, C. L., Hawkesworth, C. J. & Zhang, Y. (1988*b*). Isotope geochemistry of the 1985 Tibet geotraverse, Lhasa to Golmud. *Philosophical Transactions of the Royal Society of London, Series A* **327**, 263–285.

Hart, S. R. (1984). The DUPAL anomaly: a large-scale isotopic anomaly in the southern hemisphere. *Nature* **309**, 753–756.

Hawkesworth, C. J., Gallagher, K., Hergt, J. M. & McDermott, F. (1993). Mantle and slab contributions in arc magmas. *Annual Review of Earth and Planetary Sciences* **21**, 175–204.

Hawkesworth, C. J., Turner, S. P., McDermott, F., Peate, D. W. & van Calsteren, P. (1997*a*). U–Th isotopes in arc magmas: implications for element transfer from the subducted crust. *Science* **276**, 551–555.

Hawkesworth, C., Turner, S., Peate, D., McDermott, F. & van Calsteren, P. (1997*b*). Elemental U and Th variations in island arc rocks: implications for U-series isotopes. *Chemical Geology* **139**, 207–221.

Hellebrand, E., Snow, J. E., Hoppe, P. & Hofmann, A. W. (2002). Garnet-field melting and late-stage refertilization in 'residual' abyssal peridotites from the Central Indian Ridge. *Journal of Petrology* **43**, 2305–2338.

Hirn, A., Jiang, M., Sapin, M., Diaz, J., Nercessian, A., Lu, Q. T., Lepine, J. C., Shi, D. N., Sachpazi, M., Pandey, M. R., Ma, K. & Gallart, J. (1995). Seismic anisotropy as an indicator of mantle flow beneath the Himalayas and Tibet. *Nature* **375**, 571–574.

Hofmann, A. W. (1986). Nb in Hawaiian magmas: constraints on source composition and evolution. *Chemical Geology* **57**, 17–30.

Hofmann, A. W. (1988). Chemical differentiation of the Earth: the relationship between mantle, continental crust, and the oceanic crust. *Earth and Planetary Science Letters* **90**, 297–314.

Hofmann, A. W. (1997). Mantle geochemistry: the message from oceanic volcanism. *Nature* **385**, 219–229.

Hsü, K. J., Pan, G., Sengor, A. M. C., Briegel, U., Chen, H., Chen, C., Harris, N., Hsü, P., Li, J., Luo, J., Lee, T., Li, Z. X., Lu, C., Powell, C., Wang, Q. & Winterer, E. L. (1995). Tectonic evolution of the Tibetan plateau: a working hypothesis based on the archipelago model of orogenesis. *International Geology Review* **37**, 473–508.

Jacobsen, S. B. & Wasserburg, G. J. (1980). Sm–Nd isotopic evolution of chondrites. *Earth and Planetary Science Letters* **50**, 139–155.

Jiang, C. F., Wang, Z. Q. & Li, J. Y. (2000). *Opening and Closing Tectonics of Central Orogenic Belt in China*. Beijing: Geological Publishing House, pp. 1–153 (in Chinese with English abstract).

Jin, X. & Zhu, H. (2000). Determination of 43 trace elements in rock samples by double focusing high resolution inductively coupled plasma-mass spectrometry. *Chinese Journal of Analytical Chemistry* **28**, 563–567 (in Chinese with English abstract).

Jin, Y., McNutt, M. K. & Zhu, Y. S. (1996). Mapping the descent of Indian and Eurasian plates beneath the Tibetan Plateau from gravity anomalies. *Journal of Geophysical Research* **101**, 11275–11290.

Johnson, K. T. M. (1998). Experimental determination of partition coefficients for rare earth and high-field-strength elements between clinopyroxene, garnet, and basaltic melt at high pressures. *Contributions to Mineralogy and Petrology* **133**, 60–68.

Johnson, K. T. M., Dick, H. J. B. & Shimizu, N. (1990). Melting in the oceanic upper mantle: an ion microprobe study of diopsides in abyssal peridotites. *Journal of Geophysical Research* **95**, 2661–2678.

Kapp, P., Yin, A., Manning, C. E., Murphy, M., Harrison, T. M., Spurlin, M., Ding, L., Deng, X. & Wu, C. (2000). Blueschist-bearing metamorphic core complexes in the Qiangtang block reveal deep crustal structure of northern Tibet. *Geology* **28**, 19–22.

Kapp, P., Yin, A., Manning, C. E., Murphy, M., Harrison, T. M. & Ding, L. (2003). Tectonic evolution of the early Mesozoic blueschist-bearing Qiangtang metamorphic belt, central Tibet. *Tectonics* **22**(4), 1043, doi: 10.1029/2002TC001383.

Kelemen, P. B., Hart, S. R. & Bernstein, S. (1998). Silica enrichment in the continental upper mantle via melt/rock reaction. *Earth and Planetary Science Letters* **164**, 387–406.

Keppler, H. (1996). Constraints from partitioning experiments on the composition of subduction zone fluids. *Nature* **380**, 237–240.

Kosarev, G., Kind, R., Sobolev, S. V., Yuan, X., Hanka, W. & Oreshin, S. (1999). Seismic evidence for a detached Indian lithospheric mantle beneath Tibet. *Science* **283**, 1306–1309.

Lai, S. & Liu, C. (2001). Enriched upper mantle and eclogitic lower crust in north Qiangtang, Qinghai–Tibet plateau: petrological and geochemical evidences from the Cenozoic volcanic rocks. *Acta Petrologica Sinica* **17**, 459–468 (in Chinese with English abstract).

Lai, S., Deng, J. & Zhao, H. (1996). *Volcanism on the Northern Edge of the Tibetan Plateau and Tectonic Evolution*. Xi'an: Shanxi Scientific and Technology Press, pp. 1–135 (in Chinese with English abstract).

Lai, S., Liu, C. & Yi, H. (2003). Geochemistry and petrogenesis of Cenozoic andesite–dacite associations from the Hoh Xil region, Tibetan Plateau. *International Geology Review* **45**, 998–1019.

Lave, J., Avouac, J. P., Laccassin, R., Tapponnier, P. & Montagner, J. P. (1996). Seismic anisotropy beneath Tibet: evidence for eastward extrusion of the Tibetan lithosphere? *Earth and Planetary Science Letters* **140**, 83–96.

Le Bas, M. J., Le Maitre, R. W., Streckeisen, A. & Zanettin, B. (1986). A chemical classification of volcanic rocks based on the total alkali–silica diagram. *Journal of Petrology* **27**, 745–750.

Leeder, M. R., Smith, A. B. & Yin, J. (1988). Sedimentology and palaeoenvironmental evolution of the 1985 Tibet geotraverse, Lhasa to Golmud. *Philosophical Transactions of the Royal Society of London, Series A* **327**, 107–143.

Le Maitre, R. W., Bateman, P., Dudek, A., Keller, J., Lameyre, J., Le Bas, M. J., Sabine, P. A., Schmid, R., Sorensen, H., Streckeisen, A., Woolley, A. R. & Zanettin, B. (1989). *A Classification of Igneous Rocks and A Glossary of Terms*. Oxford: Blackwell Scientific.

Lenardic, A. & Kaula, W. M. (1995). More thoughts on convergent crustal plateau formation and mantle dynamics with regard to Tibet. *Journal of Geophysical Research* **100**, 15193–15203.

Li, C. (1987). The Longmucuo–Shuanghu–Langcangjiang suture and the north boundary of distribution of Permo-Carboniferous Gondwana facies in North Tibet, China. *Journal of Changchun College of Geology* **17**, 155–168 (in Chinese with English abstract).

Li, C., Fan, H. & Xu, F. (1989). Petrochemical characteristics of Cenozoic volcanic rocks in Qinghai–Xizang (Tibet) and its structural significance. *Geoscience* **3**, 58–69 (in Chinese with English abstract).

Li, C., Cheng, L., Hu, K., Yang, Z. & Hong, Y. (1995). *A Study on the Palaeo-Tethys Suture Zone of Longmu Co–Shuanghu, Tibet*. Beijing: Geological Publishing House, pp. 1–131 (in Chinese with English abstract).

Liu, C. & Xie, G. (1989). Geochemistry of trace element and Sr, Nd, Ce, O isotopes of Cenozoic volcanic rocks in Kangsulake, Yutian county, Xinjing, China. *Chinese Science Bulletin* **23**, 1803–1806 (in Chinese).

Liu, J. (1989). Comment on 'ages and distributions of the volcanic rocks in Pulu, Xinjing, China'. *Acta Petrologica Sinica* **2**, 95–97 (in Chinese with English abstract).

Liu, J. (1999). *Volcanoes in China*. Beijing: Science Press, 219 pp. (in Chinese).

Liu, J. & Maimaiti, Y. (1990). Distribution and K–Ar ages of Quaternary volcanoes in western Kunlun mountains. *Science in China (Series B)* **2**, 180–187 (in Chinese).

Lugmair, G. W. & Marti, K. (1978). Lunar initial $^{143}Nd/^{144}Nd$: differential evolution of the lunar crust and mantle. *Earth and Planetary Science Letters* **39**, 349–357.

Luo, Z., Zhang, W., Deng, J., Zheng, J. & Su, S. (2000). Characteristics and geological significances of the deep-seated xenoliths in Cenozoic basalts in Kangxiwa, western Kunlun mountains, Tibet, China. *Earth Science Frontiers* **7**, 295–298 (in Chinese with English abstract).

Luo, Z., Bai, Z., Zhao, Z., Zhan, H. & Li, L. (2003). Cenozoic magmatism in the south and north rims of Tarim basin: petrogenesis and tectonic implications. *Earth Science Frontiers* **10**, 179–189 (in Chinese with English abstract).

Mahoney, J. J., Natland, J. H., White, W. M., Poreda, R., Bloomer, S. H., Fisher, R. L. & Baxter, A. N. (1989). Isotopic and geochemical provinces of the western Indian Ocean spreading. *Journal of Geophysical Research* **94**, 4033–4052.

Matte, Ph., Tapponnier, P., Arnaud, N., Bourjot, L., Avouac, J. P., Vidal, Ph., Liu, Q., Pan, Y. & Wang, Y. (1996). Tectonics of Western Tibet, between the Tarim and the Indus. *Earth and Planetary Science Letters* **142**, 311–330.

Mattern, F. & Schneider, W. (2000). Suturing of the Proto- and Paleo-Tethys oceans in the western Kunlun (Xinjiang, China). *Journal of Asian Earth Sciences* **18**, 637–650.

McCulloch, M. T. & Black, L. P. (1984). Sm–Nd isotope systematics of Enderby Land granulites and evidence for the redistribution of Sm and Nd during metamorphism. *Earth and Planetary Science Letters* **71**, 46–58.

McNamara, D. E., Owens, T. J., Silver, P. G. & Wu, F. T. (1994). Shear wave anisotropy beneath the Tibetan plateau. *Journal of Geophysical Research* **99**, 13655–13665.

McNamara, D. E., Owens, T. J. & Walter, W. R. (1995). Observations of the regional phase propagation in the Tibetan plateau. *Journal of Geophysical Research* **100**, 22215–22229.

Meyer, B., Tapponnier, P., Bourjot, L., Metevier, F., Gaudemer, Y., Peltzer, G., Guo, S. & Chen, Z. (1998). Crustal thickening in Gansu–Qinghai, lithospheric mantle subduction, and oblique, strike-slip controlled growth of the Tibet plateau. *Geophysical Journal International* **135**, 1–47.

Mo, X., Lu, F. & Deng, J. (1991). Volcanism in Sanjiang Tethyan orogenic belt: new facts and concepts. *Journal of China University Geosciences* **2**, 58–74 (in Chinese with English abstract).

Mo, X., Lu, F., Cheng, S., Zhu, Q., Hou, Z., Yang, K., Deng, J., Liu, X. & He, C. (1993). *Sanjiang Tethyan Volcanism and Related Mineralization*. Beijing: Geological Publishing House, 267 pp. (in Chinese with English abstract).

Mo, X., Zhao, Z., Deng, J., Dong, G., Zhou, S., Guo, T., Zhang, S. & Wang, L. (2003). Response of volcanism to the India–Asia collision. *Earth Science Frontiers* **10**, 135–148 (in Chinese with English abstract).

Molnar, P., Burchfiel, B. C., Zhao, Z., Lian, K., Wang, S. & Huang, M. (1987). Geologic evolution of northern Tibet: results of an expedition to Ulugh Muztagh. *Science* **235**, 1684–1688.

Ni, J. & Barazangi, M. (1983). High-frequency seismic wave propagation beneath the Indian Shield, Himalayan Arc, Tibetan Plateau and surrounding regions; high uppermost mantle velocities and efficient Sn propagation beneath Tibet. *Geophysical Journal of the Royal Astronomical Society* **72**, 665–689.

Niu, Y., Regelous, M., Wendt, I. J., Batiza, R. & O'Hara, M. J. (2002). Geochemistry of near-EPR seamounts: implicance of source vs process and the origin of enriched mantle component. *Earth and Planetary Science Letters* **199**, 327–345.

Norin, E. (1946). Geological explorations in Western Tibet. In: *Reports from the Scientific Expedition to the Northwestern Provinces of China under the Leadership of Dr. Sven Hedin* **29** (III), *Geology 7*. Stockholm: Tryckeri Aktiebolaget.

Owens, T. J. & Zandt, G. (1997). Implications of crustal property variations for models of Tibetan plateau evolution. *Nature* **387**, 37–43.

Pan, Y. (1984). A discovery of ophiolitic assemblage in Tongtianhe, Qinghai province, China. *Seismological Geology* **2**, 44 (in Chinese with English abstract).

Pan, Y. (1996). *Geological Evolution of the Karakorum–Kunlun Mountains*. Beijing: Seismological Press, pp. 1–288 (in English).

Pan, Y. (2000). Tectonic evolution of the Karakorum–Kunlun mountains. In: Pan, Y. (ed.) *Geological Evolution of the Karakorum–Kunlun Mountains*. Beijing: Science Press, pp. 509–525 (in Chinese).

Pan, Y. & Bian, Q. (2000). Tectonic geology of the Karakorum–Kunlun mountains. In: Pan, Y. (ed.) *Geological Evolution of the Karakorum–Kunlun Mountains*. Beijing: Science Press, pp. 393–426 (in Chinese).

Pan, Y., Kong, X., Zhong, D., Wang, Q., Xiong, S., Ding, L. & Yan, Y. (1998). Lithospheric structure, evolution and dynamics of Qinghai–Xizang (Tibetan) plateau. In: Sun, H. & Zheng, D. (eds) *Formation, Evolution and Development of Qinghai–Xizang (Tibetan) Plateau*. Guangzou: Guangdong Scientific & Technological Press, pp. 3–71 (in Chinese with English abstract).

Pearce, J. A. (1982). Trace element characteristics of lavas from destructive plate boundaries. In: Thorpe, R. S. (ed.) *Andesites*. New York: John Wiley, pp. 525–548.

Pearce, J. A. & Mei, H. (1988). Volcanic rocks of the 1985 Tibet geotraverse: Lhasa to Golmud. *Philosophical Transactions of the Royal Society of London, Series A* **327**, 169–201.

Pearce, J. A. & Parkinson, I. J. (1993). Trace element models for mantle melting: application to volcanic arc petrogenesis. In: Prichard, H. M., Alabaster, T., Harris, N. B. W. & Neary,C. R. (eds) *Magmatic Processes and Plate Tectonics*. *Geological Society, London, Special Publications* **76**, 373–403.

Pearce, J. A. & Peate, D. W. (1994). Tectonic implications of the composition of volcanic arc magmas. *Annual Review of Earth and Planetary Sciences* **123**, 251–285.

Plank, T. & Langmuir, C. H. (1998). The chemical composition of subducting sediment and its consequences for the crust and mantle. *Chemical Geology* **145**, 325–394.

QBGMR (Qinghai Bureau of Geology and Mineral Resources) (1991). *Regional Geology of Qinghai Province*. Beijing: Geological Publishing House, pp. 1–662 (in Chinese with English abstract).

Rehkämper, M. & Hofmann, A. W. (1997). Recycled ocean crust and sediment in Indian Ocean MORB. *Earth and Planetary Science Letters* **147**, 93–106.

Rickwood, P. C. (1989). Boundary lines within petrologic diagrams which use oxides of major and minor elements. *Lithos* **22**, 247–263.

Ryan, J. G., Morris, J., Tera, F., Leeman, W. P. & Tsvetskov, A. (1995). Cross-arc geochemical variations in the Kurile arc as a function of slab depth. *Science* **270**, 625–627.

Sandvol, E., Ni, J., Kind, R. & Zhao, W. (1997). Seismic anisotropy beneath the southern Himalayas–Tibet collision zone. *Journal of Geophysical Research* **102**,17813–17823.

Sheppard, S. & Taylor, W. R. (1992). Barium- and LREE-rich, olivine–mica-lamprophyres with affinities to lamproites, Mt. Bundey, Northern Territory, Australia. *Lithos* **28**, 303–325.

Silver, P. J. (1996). Seismic anisotropy beneath the continents: probing the depths of geology. *Annual Review of Earth and Planetary Sciences* **24**, 385–432.

Sobel, E. & Arnaud, N. (1999). A possible middle Palaeozoic suture in the Altyn Tagh, NW China. *Tectonics* **18**, 64–74.

Spera, F. J. & Bohrson, W. A. (2001). Energy-constrained open-system magmatic processes I: general model and energy-constrained assimilation and fractional crystallization (EC-AFC) formulation. *Journal of Petrology* **42**, 999–1018.

Steiger, R. H. & Jager, E. (1977). Subcommission on geochronology: convention of the use of decay constants in geo- and cosmochronology. *Earth and Planetary Science Letters* **36**, 359–362.

Sun, S.-S. & McDonough, W. F. (1989). Chemical and isotopic systematics of ocean basalts: implications for mantle composition and processes. In: Saunders, A. D. & Norry, M. J. (eds) *Magmatism in the Ocean Basins*. *Geological Society, London, Special Publications*, **42**, 313–345.

Sun, Y. (1992). Geological characteristics of the Miocene volcanic belts in the northern margin of the Hoh Xil mountains. *Qinghai Geology* **2**, 40–47 (in Chinese with English abstract).

Tahirkheli, R. A. K. (1982). Geology of Himalaya, Karakorum and Hindukush in Pakistan. *Geological Bulletin of University of Pesh* (Special Issue) **15**, 504–519.

Tan, F., Pan, G. & Xu, Q. (2000). The uplift of Qinghai–Xizang (Tibetan) plateau and geochemical characteristics of Cenozoic volcanic rocks in the center of the Qiangtang terrane, Tibet. *Acta Petrologica et Mineralogica* **19**, 121–130 (in Chinese with English abstract).

Tapponnier, P. & Molnar, P. (1977). Active faulting and Cenozoic tectonics of China. *Journal of Geophysical Research* **82**, 2905–2930.

Tapponnier, P., Xu, Z., Roger, F., Meyer, B., Arnaud, N., Wittlinger, G. & Yang, J. (2001). Oblique stepwise rise and growth of the Tibet plateau. *Science* **294**, 1671–1677.

Tatsumi, Y., Hamilton, D. L. & Nesbitt, R. W. (1986). Chemical characteristics of fluid phase released from a subducted lithosphere and origin of arc magmas: evidence from high-pressure experiments

and natural rocks. *Journal of Volcanology and Geothermal Research* **29**,293–309.

Turner, S. P. (2002). On the time-scales of magmatism at island-arc volcanoes. *Philosophical Transactions of the Royal Society, Series A* **360**, 2853–2871.

Turner, S., Hawkesworth, C., Liu, J., Rogers, N., Kelley, S. & van Calsteren, P. (1993). Timing of Tibetan uplift constrained by analysis of volcanic rocks. *Nature* **364**, 50–54.

Turner, S., Arnaud, N., Liu, J., Rogers, N., Hawkesworth, C., Harris, N., Kelley, S., van Calsteren, P. & Deng, W. (1996*a*). Post-collision, shoshonitic volcanism on the Tibetan Plateau: implications for convective thinning of the lithosphere and the source of ocean island basalts. *Journal of Petrology* **37**, 45–71.

Turner, S., Hawkesworth, C., van Calsteren, P., Heath, E., Macdonald, R. & Black, S. (1996*b*). U-series isotopes and destructive plate margin magma genesis in the Lesser Antilles. *Earth and Planetary Science Letters* **142**, 191–207.

Turner, S., Hawkesworth, C., Rogers, N., Bartlett, J., Worthington, T., Hergt, J., Pearce, J. & Smith, I. (1997). ^{238}U–^{230}Th disequilibrium, magma petrogenesis, and flux rates beneath the depleted Tonga–Kermadec island arc. *Geochimica et Cosmochimica Acta* **61**, 4855–4884.

Turner, S., Bourdon, B. & Gill, J. (2003). Insight into magma genesis at convergent margins from U-series isotopes. In: Bourdon, B., Henderson, G. M., Lundstrom, C. C. & Turner, S. P. (eds) *Uranium-Series Geochemistry. Reviews in Mineralogy and Geochemistry, Mineralogical Society of America* **52**, 255–310.

Unsworth, M., Wei, W., Jones, A. G., Li, S., Bedrosian, P., Booker, J., Jin, S., Deng, M. & Tan, H. (2004). Crustal and upper mantle structure of northern Tibet imaged with magnetotelluric data. *Journal of Geophysical Research* **109**, B02403, doi: 10.1029/2002JB002305.

Vroon, P. Z., Van Bergen, M. J., White, W. M. & Varekamp, J. C. (1993). Sr–Nd–Pb isotope systematics of the Banda Arc, Indonesia: combined subduction and assimilation of continental material. *Journal of Geophysical Research* **98**, 22349–22366.

Wang, Q., McDermott, F., Xu, J., Bellon, H. & Zhu, Y. (2005). Cenozoic K-rich adakitic volcanic rocks in the Hohxil area, northern Tibet: lower-crustal melting in an intracontinental setting. *Geology* **33**, 465–468.

Wang, X. F., Metcalfe, I., Jian, P., He, L. Q. & Wang, C. S. (2000). The Jinshajiang–Ailaoshan Suture Zone, China: tectono-stratigraphy, age and evolution. *Journal of Asian Earth Sciences* **18**, 675–690.

White, W. M., Hofmann, A. W. & Puchelt, H. (1987). Isotope geochemistry of Pacific mid-ocean ridge basalt. *Journal of Geophysical Research* **92**, 4881–4893.

Willet, S. D. & Beaumont, C. (1994). Subduction of Asian lithospheric mantle beneath Tibet inferred from models of continental collision. *Nature* **369**, 642–645.

Williams, H. M., Turner, S. P., Pearce, J. A., Kelley, S. P. & Harris, N. B. W. (2004). Nature of the source regions for post-collisional, potassic magmatism in southern and northern Tibet from geochemical variations and inverse trace element modeling. *Journal of Petrology* **45**, 555–607.

Wilson, M. (1989). *Igneous Petrogenesis: a Global Tectonic Approach*. London: Unwin Hyman, 466 pp.

Wittlinger, G., Masson, F., Poupinet, G., Tapponnier, P., Jiang, M., Herquel, G., Guilbert, J., Achauer, U., Xue, G. & Shi, D. (1996). Seismic tomography of northern Tibet and Kunlun: evidence for crustal blocks and mantle velocity contrasts. *Earth and Planetary Science Letters* **139**, 263–279.

Wu, C., Yang, J., Li, H., Shi, R. & Meng, F. (2001). Pyroxene xenolith in the Cenozoic volcanic rocks of north Tibet. *Acta Geoscientia Sinica* **22**, 61–66 (in Chinese with English abstract).

Wu, G., Xiao, X. & Li, T. (1989). A study on the geological traverse from Yadong to Golmud in the Tibetan plateau. *Bulletin of Geology* **63**, 285–296 (in Chinese with English abstract).

Wu, H. (1993). Discovery of Early Carboniferous deep-sea sediments from Jinsha Belt, NW Yunnan. *Scientia Geologica Sinica* **28**, 395–397 (in English).

XBGMR (Xinjiang Bureau of Geology and Mineral Resources) (1993). *Regional Geology of Xinjiang Province*. Beijing: Geological Publishing House, pp. 1–401 (in Chinese with English abstract).

Xiao, W., Windley, B., Hao, J. & Li, J. (2002). Arc-ophiolite obduction in the Western Kunlun Range (China): implications for the Palaeozoic evolution of central Asia. *Journal of the Geological Society, London* **159**, 517–528.

Xiao, X., Liu, X., Gao, R., Houn, K. & Luo, Z. (2001). Collision tectonics between the Tarim block (basin) and the northwestern Tibetan Plateau: new observation from a multidisciplinary geoscientific investigation in the western Kunlun mountains. *Acta Geologica Sinica* **75**, 126–132 (in English).

Xu, R. & Pan, Y. (1993). Timing of the orogenic process of the north tectonic belt in west Kunlun mountains. In: *Lithospheric Tectonic Evolution Research (1)*. Beijing: Seismological Press, pp. 121–127 (in English).

Xu, R., Zhang, Y., Xie, Y., Vidal, Ph., Arnaud, N., Zhang, Q. & Zhao, D. (2000). Isotopic geochemical characteristics of igneous rocks in the Karakorum–Kunlun mountains. In: Pan, Y. (ed.) *Geological Evolution of the Karakorum–Kunlun Mountains*. Beijing: Science Press, pp. 324–392 (in Chinese).

Xu, Z., Jiang, M., Yang, J., Zhao, G., Cui, J., Li, H., Lu, Q. & Xue, G. (1999). Mantle diapir and inward intracontinental subduction: a discussion on the mechanism of uplift of the Qinghai–Tibet plateau. In: Macfarlane, A., Sorkhabi, R. B. & Quade, J. (eds) *Himalaya and Tibet: Mountain Roots to Mountain Tops. Geological Society of America, Special Papers* **328**, 19–31.

Yang, J., Robinson, P. T., Jiang, C. & Xu, Z. (1996). Ophiolites of the Kunlun Mountains, China and their tectonic implications. *Tectonophysics* **258**, 215–231.

Yang, K. H. (1998). A plate reconstruction of the eastern Tethyan orogen in southwestern China. In: Flower, M. F. J., Chung, S.-L., Lo, C.-H. & Lee, T.-Y. (eds) *Mantle Dynamics and Plate Interactions in East Asia. American Geophysical Union, Geodynamics Series* **27**, 269–287.

YBGMR (Yunnan Bureau of Geology and Mineral Resources) (1990). *Regional Geology of Yunnan Province*. Beijing: Geological Publishing House, 728 pp. (in Chinese with English abstract).

Yin, A. & Harrison, T. M. (2000). Geologic evolution of the Himalayan–Tibetan orogen. *Annual Review of Earth and Planetary Sciences* **28**, 211–280.

Yin, A. & Nie, S. (1996). A Phanerozoic palinspastic reconstruction of China and its neighboring region. In: Yin, A. & Harrison, T. M. (eds) *The Tectonics of Asia*. New York: Cambridge University Press, pp. 442–485.

Zhang, H. F., Sun, M., Zhou, X. H., Fan, W. M., Zhai, M. G. & Yin, J. F. (2002). Mesozoic lithosphere destruction beneath the North China Craton: evidence from major-, trace- element and Sr–Nd–Pb isotope studies of Fangcheng basalts. *Contributions to Mineralogy and Petrology* **144**, 241–253.

Zhang, Y. & Zheng, J. (1994). *Geological Outline of the Hoh Xil Mountains and Neighboring Areas in Qinghai Province, China*. Beijing: Seismological Press, pp. 1–177 (in Chinese with English abstract).

Zhang, Y., Xie, Y., Xu, R., Vidal, Ph. & Arnaud, N. (2000). Geochemistry of granitoid rocks in the Karakorum–Kunlun mountains. In: Pan, Y. (ed.) *Geological Evolution of the Karakorum–Kunlun Mountains*. Beijing: Science Press, pp. 209–258 (in Chinese).

Zhao, Z., Li, Y., Yie, H. & Zhang, Y. (2001). *Tectonic Characteristics and Basin Evolution of the Tibetan Plateau*. Beijing: Science Press, 439 pp. (in Chinese with English abstract).

Zhao, Z., Mo, X., Luo, Z., Zhou, S., Dong, G., Wang, L. & Zhang, F. (2003). Subduction of India beneath Tibet: magmatism evidence. *Earth Science Frontiers* **10**, 149–157 (in Chinese with English abstract).

Zhou, H.-W. & Murphy, M. A. (2005). Tomographic evidence for wholesale underthrusting of India beneath the entire Tibetan plateau. *Journal of Asian Earth Sciences* **25**, 445–457.

Zhou, X., Cao, Y. & Zhu, M. (1989). *An Explanation to the Plate Tectonic Map of Tibet*. Beijing: Geological Publishing House, pp. 1–39 (in Chinese).

Zhu, J., Cao, J., Cai, X., Yan, Z. & Cao, X. (2002). High resolution surface wave tomography in East Asia and West Pacific marginal seas. *Chinese Journal of Geophysics* **45**, 646–664 (in Chinese with English abstract).

Zinder, A. & Hart, S. R. (1986). Chemical geodynamics. *Annual Review of Earth and Planetary Sciences* **14**, 493–571.

Zou, H. B., Zindler, A., Xu, X. S. & Qi, Q. (2000). Major, trace element, and Nd, Sr and Pb isotope studies of Cenozoic basalts in SE China: mantle sources, regional variations and tectonic significance. *Chemical Geology* **171**, 33–47.